Molecular Recognition in Host-Guest
Ionophore-Siderophore Assemblies

by

Esther Marie Tristani

Department of Chemistry
Duke University

Date:_______________________
Approved:

____
Alvin L. Crumbliss, Supervisor

____
Richard A. Palmer

____
Michael C. Fitzgerald

____
George R. Dubay

Dissertation submitted in partial fulfillment of
the requirements for the degree of Doctor
of Philosophy in the Department of
Chemistry in the Graduate School
of Duke University

2010

ABSTRACT

Molecular Recognition in Host-Guest Ionophore-Siderophore Assemblies

by

Esther Marie Tristani

Department of Chemistry
Duke University

Date:_______________________
Approved:

____
Alvin L. Crumbliss, Supervisor

____
Richard A. Palmer

____
Michael C. Fitzgerald

____
George R. Dubay

An abstract of a dissertation submitted in partial
fulfillment of the requirements for the degree
of Doctor of Philosophy in the Department of
Chemistry in the Graduate School
of Duke University

2010

Abstract

This work examines the characterization of supramolecular assemblies and, more specifically, host-guest complexes involved in molecular recognition events. The supramolecular assemblies studied take root from metal ion delivery in biological uptake pathways, specifically the delivery of iron to microbial cells. These assemblies are studied in an effort to further understand the nature of molecular recognition events, specifically the nature and strength of interactions between a host and a guest, and possible applications of these systems.

The development of a mass spectral method by which to characterize supramolecular assemblies involving the cation binding hosts 18-crown-6, benzo-18-crown-6, dicyclohexano-18-crown-6, and dibenzo-18-crown-6 macrocycles, and the linear ionophore lasalocid with cationic guests, including substituted protonated amines and the iron siderophore ferrioxamine B is presented. Methodology was developed using ESI-MS to successfully quantitate host-guest interactions in binary and complex mixtures. Binding constants were obtained in the range of log $K_a = 3 - 5$ and correspond to similar systems previously studied in the literature. The studies presented here further our understanding of the molecular recognition events that must occur between a siderophore and a receptor and provide an improved method by which to measure the strength of their interaction.

The effects of redox hosts on host-guest complex formation with ferrioxamine B and the characterization of the host-guest complexes formed and the strength of the interactions between them were studied using cyclic voltammetry, ESI-MS, FAB-MS and ITC. A shift in redox potential towards more positive values is observed upon addition of a cationic siderophore guest to a solution of a redox-active *para*-Wurster's aza crown or mono-substituted Wurster's aza crown macrocycle. Mass spectral evidence indicates the formation of a host-guest complex between the cationic siderophore and the redox host. A redox switch mechanism is proposed, whereby the redox state of the host influences the binding affinity between the host and guest and, consequently, host-guest complex formation. These systems offer a unique means by which to modulate the uptake or release of ionic guests from a cavity by using externally controlled methods and can be applied to selective metal ion compartmentalization.

Finally, the application of supramolecular assemblies as a tool in the field of drug delivery is presented. The covalent attachment of an antimalarial drug, artemisinin, by our collaborators to a siderophore produced by *M. Tuberculosis*, mycobactin, facilitates the subsequent delivery of the drug into the microbial cell by taking advantage of the natural biological iron uptake pathway. Here, the molecular recognition event and supramolecular assembly of interest is that occurring between the siderophore-drug assembly and the microbial receptor. Characterization of the siderophore-drug assembly using cyclic voltammetry shows that there is an interaction between the Fe-mycobactin and artemisinin when these are covalently attached in the form of a conjugate. Increased current output is observed due to an intramolecular electron transfer between the two components. Based on these in vitro data, we propose a redox mechanism by which the drug-siderophore conjugate exhibits a therapeutic effect in vivo.

To my mother and sister,

My colleagues and closest friends,

And to the newest members of my family,

Whose unfailing love and support have gotten me here.

Contents

List of Tables

List of Figures

List of Abbreviations

H_4DFB^+ - Desferrioxamine B
$FeHDFB^+$ - Ferrioxamine B
18C6 - 18-Crown-6
B18C6 - Benzo-18-Crown-6
DC18C6 - Dicyclohexano-18-Crown-6
DB18C6 - Dibenzo-18-Crown-6
ESI-MS - Electrospray Ionization Mass Spectrometry
FeDFE - Ferrioxamine E
NH_4^+ - ammonium ion
K^+ - potassium ion
$CH_3NH_3^+$ - methylamine ion
$CH_3(CH_2)_4NH_3^+$ - pentylamine ion
MeOH – methanol
KCl – potassium chloride
HCl – hydrochloric acid
MeCN – acetonitrile
$CHCl_3$ – chloroform
FAB-MS – Fast Atom Bombardment Mass Spectrometry
ITC – isothermal calorimetry
3-NBA – 3-nitrobenzyl alcohol
EDTA – ethylene diamine tetraacetic acid
Ca^{2+} - calcium (II) ion

TB – tuberculosis

Multidrug resistant – MDR

Extensively drug resistant - XDR

1. Introduction

1.1 Chemistry and Molecular Recognition

Supramolecular chemistry has been defined as the chemistry of molecular assemblies and of the intermolecular bond [1]. Although general, this definition encompasses specific characteristics, functions and properties such as recognition, catalysis, and transport. Supramolecular chemistry is also concerned with the degree of order of complexes, the interactions between multiple subunits, and intermolecular interactions.

Although it is a more recent field of study, the origins of supramolecular chemistry date back to the 19th century. Key developments such as (1) the introduction of "coordination chemistry" by Alfred Werner in 1893 [2], (2) the formulation of the lock and key concept by Emil Fischer in 1894 [3,4], and (3) the discovery of cyclodextrins as the first "host" molecule by Villiers and Hebd in 1891 [5,6] helped lay the foundation for the field of supramolecular chemistry [1,7]. More recently, the work of Jean-Marie Lehn on the synthesis of the first cryptands (1969) and his formal introduction of the term "supramolecular chemistry" shaped the field of supramolecular chemistry into what it is today [1,7]. These visionaries went on to receive the Nobel Prize in 1902 (Fischer), 1913 (Werner), and 1987 (Lehn) for their contributions.

Central to the study of supramolecular assemblies is the concept of molecular recognition. The essential aspect of molecular recognition is the specific nature of the interaction between two or more molecular units and, more importantly, the strength of that interaction [8]. These two units can be defined as a host and a guest, as in many cases they fit together upon assembly. The specific interactions of a host and a guest to form a supramolecular assembly involve noncovalent bonding and, more commonly, ion-dipole interactions and hydrogen bonding [1,7,8].

These types of interactions are essential in ion recognition in biological and chemical pathways. In pathways such as cellular uptake, molecular recognition leads to selectivity and reactivity in the specific uptake of ions into the cell. We are specifically interested in studying host-guest assemblies involving cation-binding hosts and cationic protonated amine guests, including a siderophore (iron chelator) guest, from a biological perspective. We are further interested in characterizing the nature and strength of interactions using a series of analytical techniques. These will be further discussed in the following sections.

1.1.1 Application to drug delivery

The concepts of supramolecular assemblies and molecular recognition can be used advantageously in the field of medicine to find new and improved methods for drug delivery. Supramolecular assemblies are being investigated in treating infections, since cellular uptake pathways can be harnessed to deliver drugs to which microbial cells would normally develop resistance [9]. Bacterial iron chelators, known as siderophores, can be used as a means of drug delivery by coupling to a known bacterial inhibitor, such as an antibiotic. Molecular recognition is a key aspect of this Trojan Horse approach, as it allows the antibiotic specific entry into the microbial cell without the complications of other drug delivery methods.

1.2 *Siderophores*

1.2.1 Biological Iron

Iron is an essential nutrient in virtually all living systems. As the fourth most abundant element and the second most abundant metal on the Earth's crust, iron is readily available [10]. However, its bioavailability is limited due to its tendency to form insoluble iron hydroxides at biological pH, Figure 1.1. Specifically, the solubility of aqueous ferric iron, $Fe(H_2O)_6^{3+}$, at physiological pH is $[Fe_{aq}^{3+}] = 10^{-18}$ M, which is 10 orders of magnitude lower than that needed to sustain essential metabolic processes [10]. The solubility of the total free ferric iron, which includes various aquo-hydroxy species, is 10^{-10} M, which is still too low to sustain these processes, Figure 1.1.

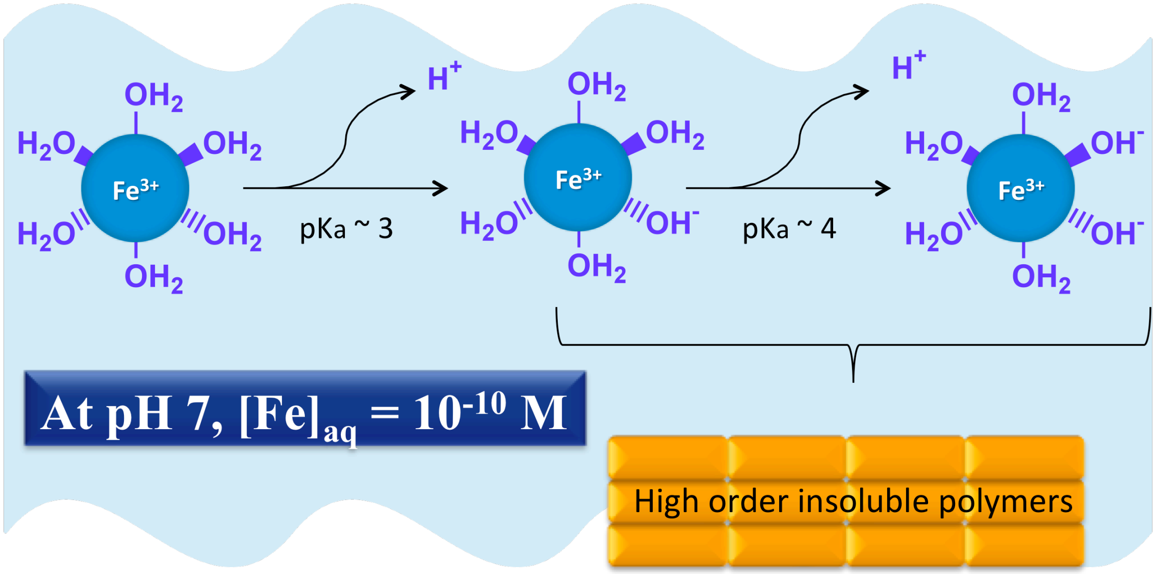

Figure 1.1 Schematic representation of the proton dissociation steps that lead to the formation of mono-, di- and tri-hydroxide species. These species can then polymerize to form higher order insoluble polymers, ultimately resulting in the formation of an insoluble gelatinous hydrous oxide.

A further complication lies in the fact that, in certain coordination environments and at certain redox potentials, iron has the ability to catalyze the generation of free radicals and reactive oxygen species through Fenton chemistry and the Haber Weiss-cycle, Figure 1.2 [11]. In this cycle, superoxide anion reduces ferric to ferrous ion. Ferrous ion then promotes the fission of the O-O bond in peroxide to generate a hydroxyl anion and a hydroxyl radical [11]. Hydroxyl radicals are extremely reactive and will abstract a hydrogen atom from virtually any type of biological molecule to form water and an organic radical, ultimately leading to oxidative damage in lipid membranes, DNA, or other biomolecules [12].

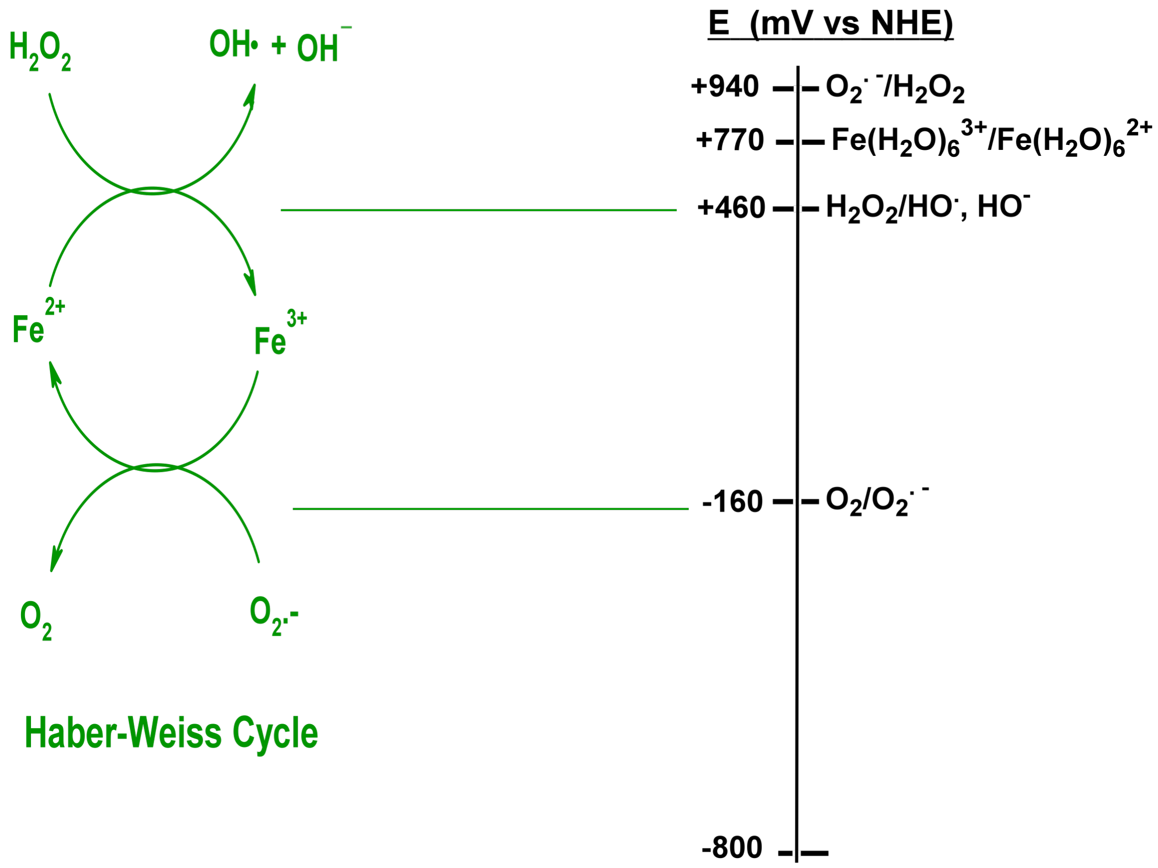

Figure 1.2 Schematic representation of Fenton chemistry and the Haber-Weiss cycle, wherein iron has the ability to catalyze the production of toxic reactive oxygen species.

Thus, although iron is a necessary nutrient, too much iron can be toxic. A strict regulation of iron in necessary in biological systems to sustain life due to the delicate balance between toxic overload and iron deficiency.

1.2.2 Siderophore-Mediated Microbial Iron Acquisition

Organisms have had to develop mechanisms for both solubilizing iron and controlling its redox potential in order to avoid production of reactive oxygen species which lead to oxidative stress. Protection is achieved in some cases through coordination with small molecules via mechanisms such as siderophore-mediated iron acquisition, wherein a siderophore (an iron chelator) is synthesized by cells to acquire iron [13]. This small molecule specifically sequesters iron, and the iron complex is transported to the cell surface. The ferri-siderophore is recognized by a receptor at the cell membrane and either (i) iron is released at the cell surface, or (ii) the ferri-siderophore complex passes through the membrane and iron is released once inside, Figure 1.3 [13-15].

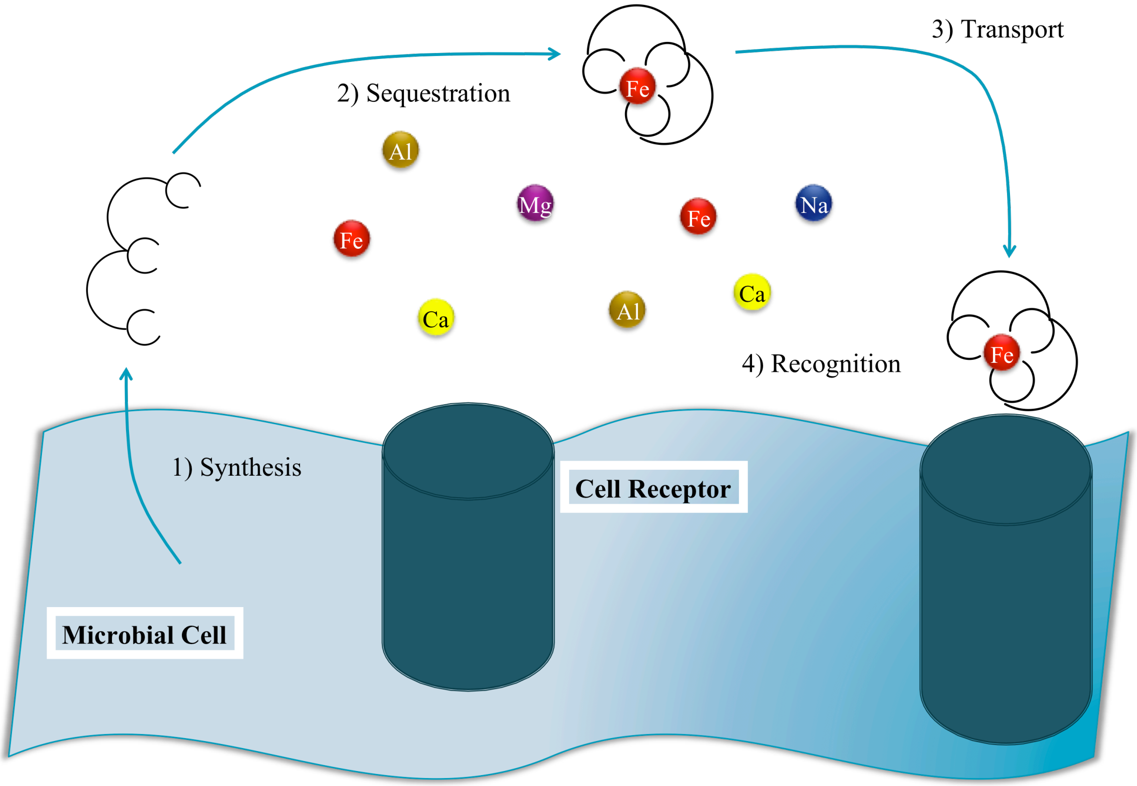

Figure 1.3 Siderophore-mediated microbial iron acquisition. A siderophore is produced by the microbial cell and sent out into the environment to specifically sequester iron. Once iron is bound, the iron-siderophore complex is transported back to the cell, where it is recognized by a cell receptor. Iron is either released from the siderophore at the cell surface, or the entire complex is transported inside the microbial cell and iron is released once inside the cell.

Molecular recognition is a vital part of iron transport across a biological membrane [15]. Without the recognition step between the siderophore and the cell receptor, the microbial cell would not acquire iron by this mechanism. Supramolecular assemblies such as host-guest complexes are studied as model systems for molecular recognition, as will be discussed in subsequent sections [16].

1.2.3 Siderophore Structures

Naturally occurring siderophores can be classified by a number of different criteria, including the organism they are produced by (bacteria, fungi, or plants), if they are peptidic or non-peptidic, and if they are cyclic or open chain structures [17]. Most often they are classified by the chemical nature of their electron pair donating groups. In this respect, we can classify siderophores into three main classes based on their principle iron-binding functional groups. These are catecholates, hydroxamates, and carboxylates, Figure 1.4. Each of these functional groups consists of a bidentate chelator group that binds iron through two hard oxygen donor atoms, making it highly specific for Fe(III). The stability of these complexes arises from both electrostatic interactions between the positively charged Fe(III) and the negative charge or dipole of the oxygen atom, and a covalent interaction in the form of a coordinate covalent bond. In addition, upon chelating Fe(III), these complexes form a five-membered chelate ring, which results in added stability, Figure 1.4 [13,18,19].

Catecholate siderophores contain ortho-dihydroxyphenyl groups and most use 2,3-dihydroxybenzoic acid as a basic unit [14]. Three catecholate groups are required for ferric iron binding in an octahedral fashion. Enterobactin, isolated from *Salmonella typhimurium*, is a prime example of a catecholate siderophore (Figure 1.5). It is the cyclic triester of N-2,3-dihydrobenzoyl-L-serine, and has been extensively studied due to its very high complexation constant with Fe(III) (on the order of 10^{52} M^{-1}) [14].

Carboxylate groups are found in many siderophores, in many cases in combination with other binding groups. When catecholate and hydroxamate siderophores are not present, iron coordinates solely to the oxygen donor atoms of a carboxylate. Rhizoferrin, isolated from *Rhizobium meliloti DM4*, was the first of this class to be discovered (Figure 1.5) [14].

Hydroxamate siderophores contain one to three hydroxylated amide bonds. The hydroxamate group can be deprotonated and serves as a bidentate ligand for ferric iron. The amine residue of the hydroxylated amine bond can be part of an amino acid, as is the case in desferrichrome, or of a diamine, as is the case in desferrioxamine B (Figure 1.5) [14]. Ferrioxamine B will be discussed further in the subsequent section. The siderophores produced by mycobactins, specifically mycobactin produced by *Mycobacterium Tuberculosis*, also contain these residues. These are also of interest to this dissertation and will be discussed in Chapter 4.

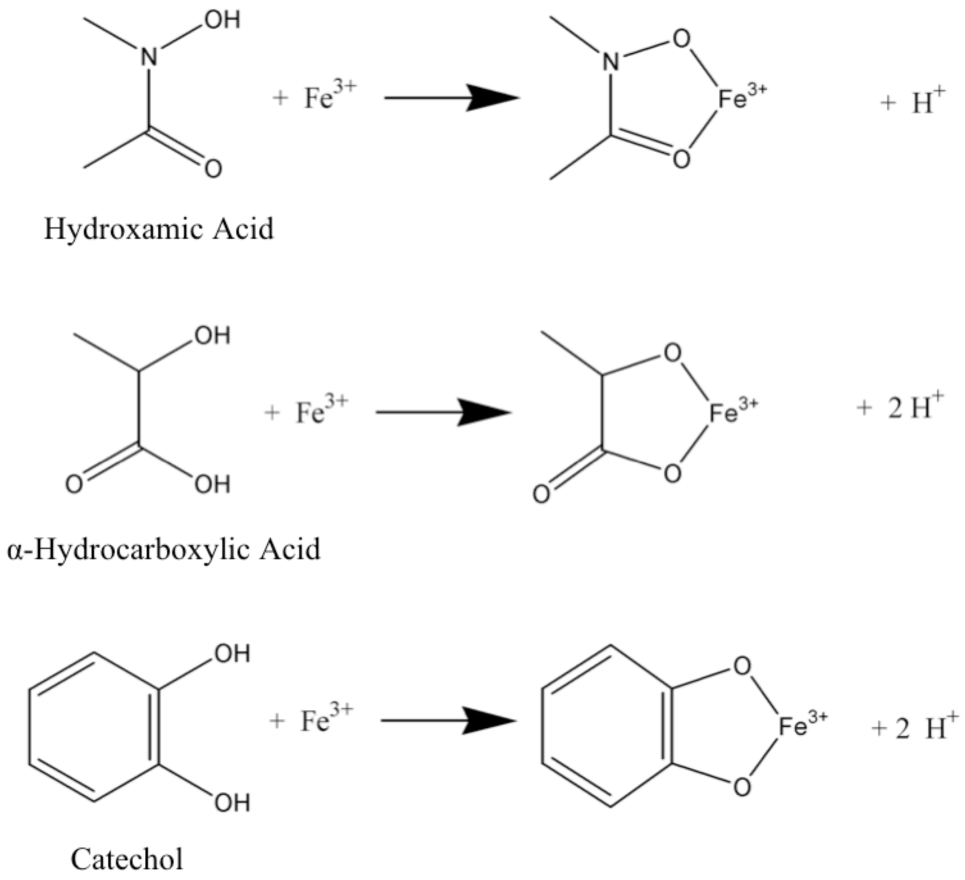

Figure 1.4 Principle iron-binding functional groups found in naturally occurring siderophores.

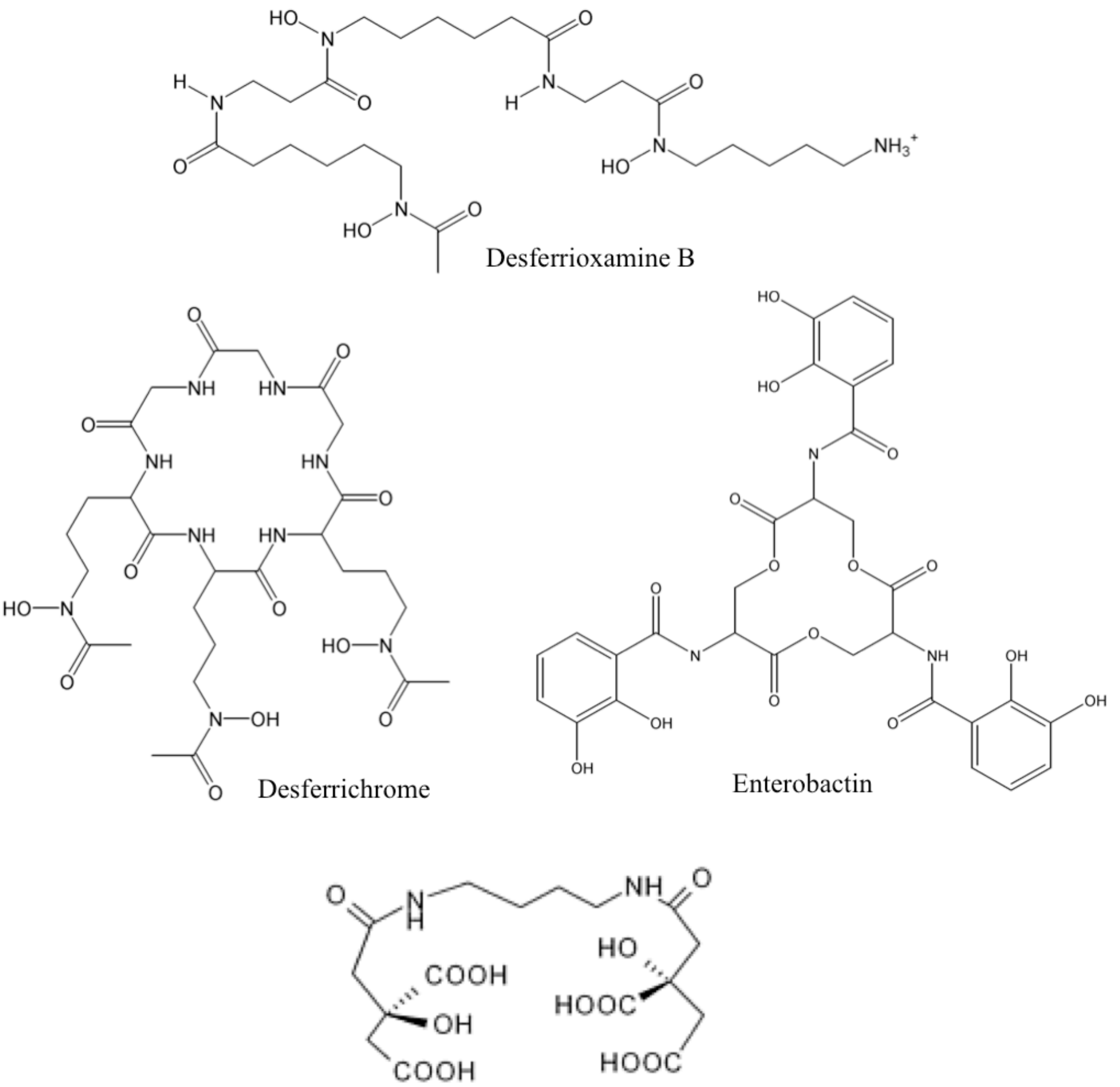

Desferrioxamine B

Desferrichrome

Enterobactin

Rhizoferrin

Figure 1.5 Structures of hydroxamate (desferrioxamine B, desferrichrome), catecholate (enterobactin), and carboxylate (rhizoferrin) siderophores of interest.

1.2.3.1 Desferrioxamine B, H_4DFB^+

Desferrioxamine B, Figure 1.5, is a natural linear trihydroxamic acid iron chelator produced by *Steptomyces pilosus* [20]. It forms a highly stable complex upon binding Fe(III) (on the order of 10^{30} M^{-1}) [21]. Currently on the market as Desferal®, it is a drug of choice for iron overload therapy [22]. Ferrioxamine B, $FeHDFB^+$ (the iron-bound form of the siderophore) has been well characterized in the literature [23-38]. One of the most important aspects of $FeHDFB^+$, and the reason why we study it, is its pendant pentylamine side chain, which is protonated at physiological pH ($pK_a = 10.8$) [39]. This side arm can serve as a recognition site and thus lies at the heart of our molecular recognition studies, as will be discussed in detail in Chapters 2 and 3.

1.3 Ionophores

Ionophores are a class of molecules that recognize and specifically bind certain ions, in most cases cations. This recognition may take place through non-covalent interactions, including hydrogen bonding, van der Waals forces, and ion-dipole interactions [1]. Generally, ionophores are lipid soluble molecules, meant to permeate biological or artificial lipid membranes to transport specific ions. These molecules vary in size and either contain a cavity in which the ion may fit, or may wrap around an ion. Here we focus on crown ethers, substituted crown ethers, and polyether carboxylic acids, as well as cavities with redox moieties, or aza-crowns, Figure 1.6. These will be discussed in detail in Chapters 2 and 3.

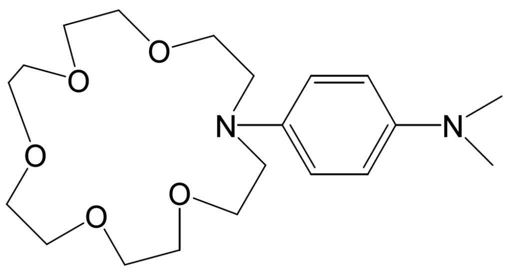

Aza-Crown Ether

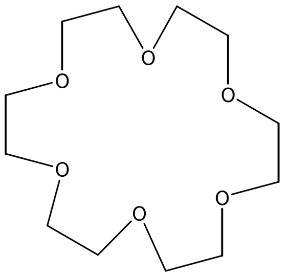

18-Crown-6 (18C6)

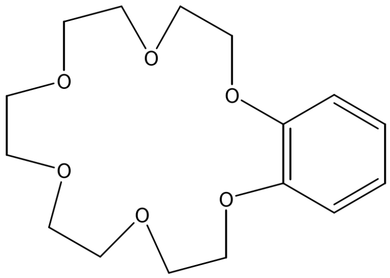

Benzo-18-Crown-6 (B18C6)

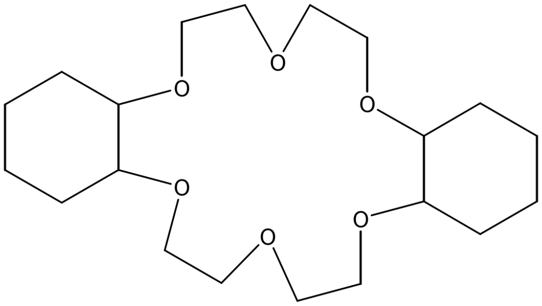

Dicyclohexano-18-Crown-6 (DC18C6)

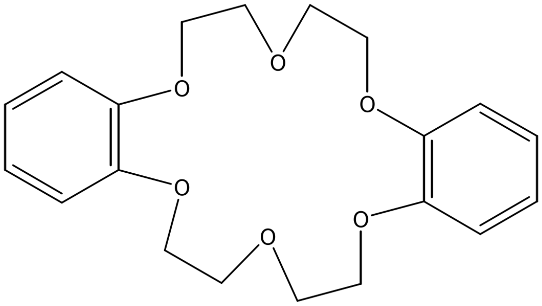

Dibenzo-18-Crown-6 (DB18C6)

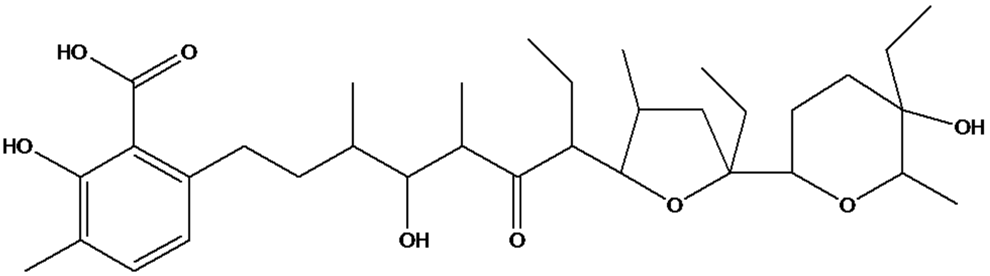

Lasalocid A

Figure 1.6 Structures of aza-crown, 18-crown-6 and substituted 18-crown-6 ethers and lasalocid A, a polyether carboxylic acid.

Our interest in these cavitands stems from their ability to recognize cationic species such as Group I ions, and compounds containing protonated amine moieties, such as the siderophore $FeHDFB^+$. Crown ethers, substituted crown ethers, and polyether carboxylic acids are able to recognize the protonated amine side chain of some siderophores, including $FeHDFB^+$, and have been used as models for membrane bound receptors [1,40-43]. Recognition of the siderophore by the ionophores listed above results in the formation of a host-guest complex, and more specifically, a supramolecular assembly.

1.4 Host-Guest Complexes

Host-guest chemistry is defined simply as a molecule (a "host") binding another molecule (a "guest") to produce a host-guest complex [1]. Most commonly, the host is a larger molecule such as an enzyme or cyclic compound containing a sizeable cavity. This molecular entity must contain convergent binding sites such as Lewis donor atoms, or hydrogen bond donors [1]. The crown ethers and similar ionophores described above fulfill these requirements and can be considered prototypical hosts. The guest molecule may be a simple cation or anion, or a more complex molecule such as a hormone. The entity must contain divergent binding sites, such as spherical Lewis acid metal cations, or hydrogen bond acceptors [1]. $FeHDFB^+$ is discussed here as the prototypical siderophore guest.

Multiple binding sites between the host and the guest are they key to highly structured complexes. The host-guest complexes studied here achieve this binding mainly through hydrogen bonding.

1.4.1 The Hydrogen Bond

Hydrogen bonding is an essential part of host-guest complex formation. These bonds are defined as dipole-dipole interactions in which a hydrogen atom attached to an electronegative atom (or electron withdrawing group) is attracted to a neighboring dipole on an adjacent molecule or functional group [1,7]. Hydrogen bonds exist in a range of lengths, strengths, and geometries. Their strengths vary from very weak (1-2 kJ/mol) to very strong (>100 kJ/mol), with an average strength of 40 kJ/mol [1,44]. For the purposes of this work, we are interested in hydrogen bonding between protonated amines, such as the protonated pendant amine of $FeHDFB^+$, and donor atoms in crown-type cavities, mostly oxygens. The strength for these interactions is on the order of 60 kJ/mol [1,36].

1.4.2 First and Second Coordination Shells

The concepts of first and second coordination shells are important to the study of host-guest chemistry. These concepts are best explained by looking at a model host-guest complex, that between $FeHDFB^+$ and 18C6, Figure 1.7.

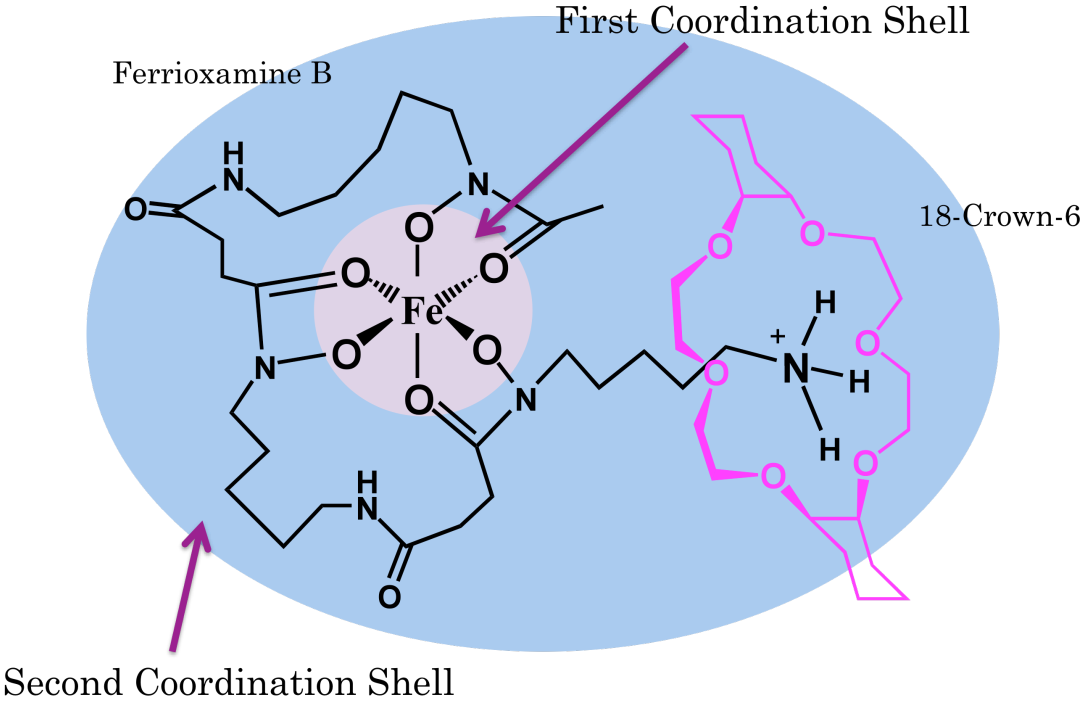

Figure 1.7 Host-guest complex formation between FeHDFB$^+$ and DC18C6 illustrating the concepts of first and second coordination shells. Based on the crystal structure obtained in reference [28].

The first coordination shell refers to the immediate environment surrounding the metal ion, mainly the atoms that are coordinate-covalently bound to the metal. In the above example, the first coordination shell is comprised of the metal and the oxygen donor atoms that are bound to it in FeHDFB$^+$. The second coordination shell refers to the environment beyond the metal bound atoms, where host-guest interactions can take place. In the example above, the second coordination shell encompasses the remainder of FeHDFB$^+$, specifically, the backbone and protonated pendant amine side chain. It is at this level that an interaction with 18C6 occurs.

First coordination shell interactions are typically very strong (on the order of 10^{30} M^{-1} in the case of the assembly in Fig 1.7), whereas second coordination shell interactions tend to be much weaker (on the order of 10^4 M^{-1} in the case of the assembly in Fig 1.7), as expected for non-covalent interactions [31]. We can look at first coordination shell interactions in $FeHDFB^+$ in terms of host-guest chemistry, where the siderophore is the host and the metal is the guest, Figure 1.7. Second coordination shell interactions can also be discussed further in the context of host-guest chemistry. As shown in Figure 1.7, 18C6 binds to the protonated pendant amine located on the side-chain of $FeHDFB^+$. This constitutes a host-guest complex, or using the terminology discussed previously, an ionophore-siderophore complex. In broader terms, these two molecules have formed a supramolecular assembly.

1.5 Statement of Research Objectives

The focus of this work is the characterization of supramolecular assemblies involved in a molecular recognition event. In some cases, these supramolecular assemblies can be classified as host-guest systems, where one component is the guest, and the other the host. In other cases, the supramolecular assembly itself serves as the guest in a biological uptake scheme where a membrane receptor serves as the host. The supramolecular assemblies studied are biologically relevant in all cases, and take root from metal ion delivery in biological uptake pathways, specifically the delivery of iron to microbial cells.

Chapter 2 focuses on the development of a mass spectral method by which to characterize supramolecular assemblies involving cation binding hosts, specifically crown ethers, substituted crown ethers, and a polyether carboxylic acid, with cationic guests, including substituted protonated amines and the iron siderophore $FeHDFB^+$. Our interest in these host-guest systems stems from an interest in iron biochemistry and in the molecular recognition events that must occur between a siderophore and a receptor in order for iron transport to take place. Our interest in the experimental approach taken led us to develop methodology to quantitate host-guest interactions in binary and complex mixtures.

In Chapter 3, we explore the effects of redox hosts on host-guest complex formation with $FeHDFB^+$ and characterize the host-guest complexes formed and the strength of the interactions between them. Specifically, we propose a redox switch mechanism, where the redox state of the host influences the binding affinity between the host and guest. The systems studied offer a unique means by which to modulate the uptake or release of ionic guests from a cavity by using externally controlled methods and can be applied to selective metal ion compartmentalization.

While Chapters 2 and 3 address the host-guest view of supramolecular assemblies, in contrast, Chapter 4 discusses the use of supramolecular assemblies as a delivery tool. Specifically, we look at the covalent attachment of a drug to a siderophore and its subsequent delivery into the microbial cell by taking advantage of the natural biological iron uptake pathway. Here, the molecular recognition event of interest is that occurring between the siderophore-drug assembly and the microbial receptor. We characterize the siderophore-drug assembly and suggest a mechanism by which the assembly takes effect.

Finally, the Appendix highlights an independent interest in pedagogy. The manuscript presented there, entitled **General Chemistry and the NO_2 / N_2O_4 System: It's Not as Simple as It Appears (and That Can Make It an Enrichment Teaching Tool)**, discusses a juxtaposition of the rules of chemistry as presented in general chemistry textbooks and the alterations that sometimes must be made to these rules in the presence of experimental data.

2. Characterization of second coordination shell ionophore-siderophore host-guest assemblies and binding selectivities in binary and complex mixtures by Electrospray Ionization Mass Spectrometry (ESI-MS)[1]

2.1 Background and Significance

Molecular recognition plays an important role in biological and chemical processes, in many cases in the form of host–guest complex assemblies. As such, there has been a growing interest in analytical techniques that can aid in the characterization of host–guest complexes, and the determination of association constants and binding selectivities. Association constants have been traditionally measured by NMR titrimetry, potentiometry, extraction, and UV–Visible spectrophotometry [45-55]. These techniques suffer from large sample consumption, lack of applicability in certain solvents, and relatively long analysis time. Recently, electrospray ionization mass spectrometry (ESI-MS) has been successfully used to measure the association constants of various complexes formed in solution upon their transfer to the gas phase [56-62]. This technique requires little sample, is applicable in a wide range of solvents, provides rapid data analysis, and as such has become a promising technique for the analysis of association constants and selectivities for intramolecular interactions. Although a wide range of host– guest complexes has been examined by ESI-MS, including small organic host–guest complexes and large biological assemblies [63-65], the systems most studied by ESI-MS center around the determination of binding selectivities of simple and modified crown ethers with alkali metal ions [66-69].

---

1 This chapter is an expansion of the material published in Tristani, E. M.; Dubay, G. R.; Crumbliss, A. L. **Characterization of second coordination shell ionophore-siderophore host-guest assemblies and binding selectivities in binary and complex mixtures by electrospray ionization mass spectrometry**. J. Incl. Phen. Macro. (2009), 64(1-2), 57-65.

The Crumbliss group has previously extensively studied the second-sphere host–guest complexation of the siderophore FeHDFB$^+$ (Figure 2.1) with a series of crown ethers as a model relevant to molecular recognition associated with microbial iron transport [23-26,32,34,35].

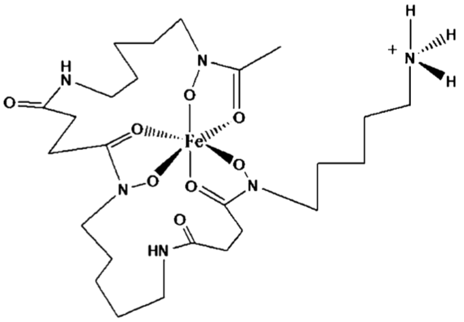

Figure 2.1 Structure of Ferrioxamine B, FeHDFB$^+$

From crystallographic studies, we have determined that FeHDFB$^+$ has the ability to form a series of host–guest complexes with macrocycles through hydrogen bonding of its protonated pendant amine tail to ether oxygen atoms present in the macrocycle ionophore (Figure 2.2) [28].

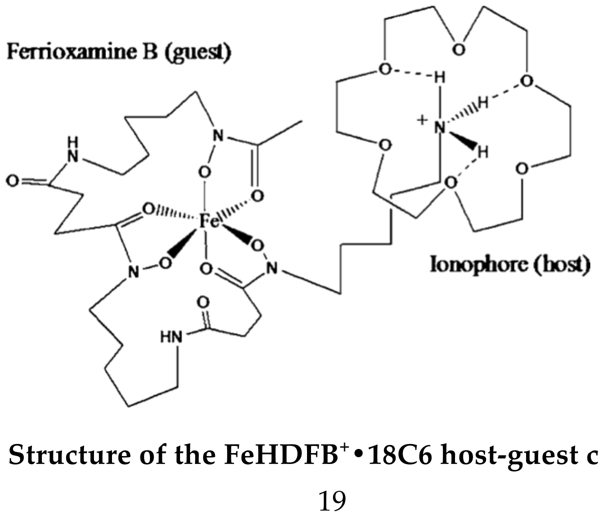

Figure 2.2 Structure of the FeHDFB$^+$•18C6 host-guest complex

Previous investigators from the Crumbliss group have obtained association constants for these complexes through liquid–liquid extraction and microcalorimetry studies [23-27,32,34,36]. However, as previously discussed, the extraction technique is both time-consuming and requires a large amount of sample to be utilized.

2.2 *Statement of Objectives*

To our knowledge, the use of ESI-MS for the determination of association constants and selectivities involving iron-loaded siderophore complex interactions with host molecules has not been pursued. This is the objective of our study. This chapter focuses on the development and discussion of a method in which ESI-MS has been used to determine association constants and binding selectivities for host–guest systems of binary and complex mixtures, including a metal complex guest. Our study involves the complexation of ammonium, protonated methylamine and pentylamine, and H_4DFB^+ with 18C6, B18C6, DC18C6, and DB18C6 host macrocycles, and the linear ionophore host lasalocid. The complexation of a metal complex guest, i.e. $FeHDFB^+$, with these macrocycles and the linear ionophore host was also studied.

2.3 *Experimental*

2.3.1 Materials

All referenced crown ethers, 18C6, B18C6, DB18C6, DC18C6 (Figure 2.3) were purchased from Acros Organics and used without further purification.

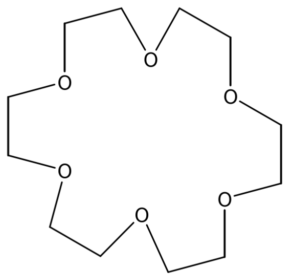

18-Crown-6 (18C6)

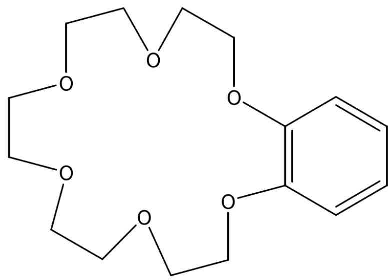

Benzo-18-Crown-6 (B18C6)

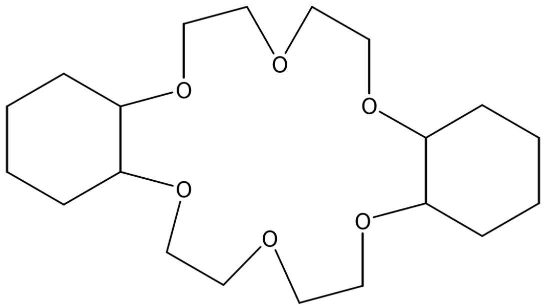

Dicyclohexano-18-Crown-6 (DC18C6)

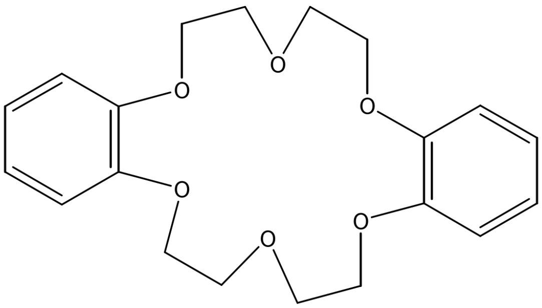

Dibenzo-18-Crown-6 (DB18C6)

Figure 2.3 Structures of the crown ethers used in this study: 18-Crown-6 (18C6), Benzo-18-Crown-6 (B18C6), Dicyclohexano-18-Crown-6 (DC18C6), and Dibenzo-18-Crown-6 (DB18C6).

Protonated methylamine and pentylamine were also purchased from Acros Organics and used without further purification. Anhydrous MeOH and tetra-n-butyl ammonium acetate were purchased from Alfa Aesar. Potassium chloride and ammonium chloride were purchased from Fisher Scientific. Ferrioxamine E, FeDFE, was purchased from Fluka, and H_4DFB^+ was obtained from Sigma Aldrich. $FeHDFB^+$ was prepared as previously described [30], using MeOH as the solvent. Lasalocid A was purchased from Sigma Aldrich. Stock solutions for all other reagents were prepared in MeOH, with the exception of that of KCl, which was prepared in 0.1 M aqueous HCl.

2.3.2 Methods

2.3.2.1 Sample Preparation

For systems of binary mixtures, a representative preparation is as follows: a series of samples was prepared containing an excess of guest (1 mM), and increasing concentrations of host (as low as 6 μM, and as high as 400 μM) in MeOH. For systems of complex mixtures, a similar series of samples was prepared, in addition to a competition sample, containing an excess of guest (1 mM), and two hosts (each at 50 μM) in MeOH. All samples contained tetra-n-butyl ammonium acetate (242 m/z) or FeDFE (658 m/z) as an internal calibration standard (13 μM, 0.1 or 1 mM). Each individual sample was filtered before analysis using PTFE membrane syringe filters with a 0.45 μm pore size, and 13 mm diameter. The experimental process is illustrated in Figure 2.4 for a binary host-guest complex system.

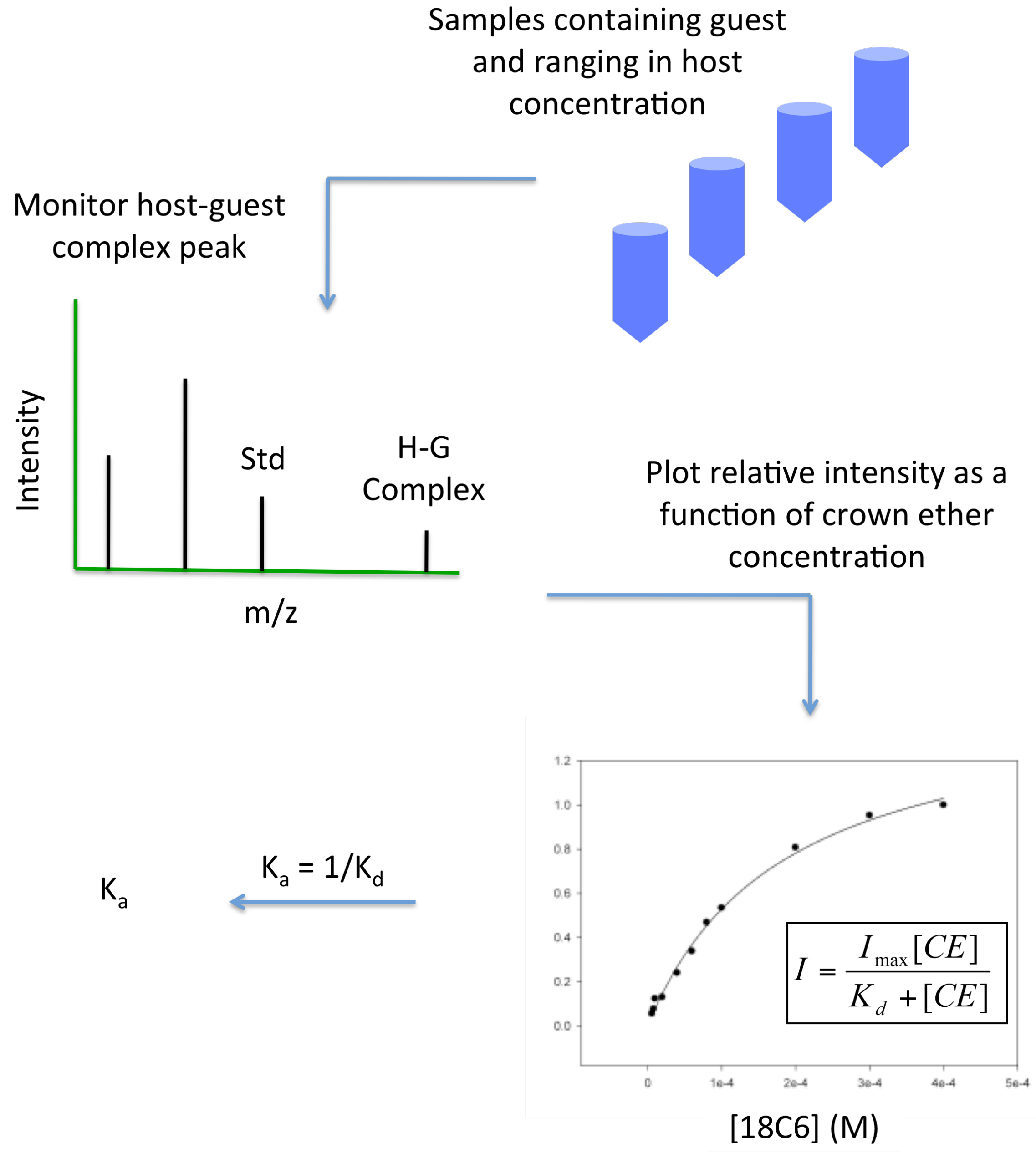

Figure 2.4 Illustration of the experimental process for a binary host-guest complex system involving 18C6 as the host.

2.3.2.2 ESI-MS

All mass spectrometry experiments were performed using an Agilent 1100 SL LC/MSD-Trap instrument in positive ion mode at a flow rate of 60 μL/min, a nebulizer pressure of 15 or 20 psi, a dry gas flow rate of 6 or 7 L/min, and an ionization chamber temperature of 50 °C, 125 °C, or 300 °C, depending on the host-guest system of interest. In addition to the conditions mentioned above, several different nebulizer pressures, dry gas flow rate, and ionization chamber temperature conditions were investigated in order to maximize the output intensity of the host-guest complex. A series of combinations of the nebulization pressure and dry gas flow rate were tested, ranging from a nebulizer pressure of 15 psi to 22 psi, and a dry gas flow rate of 5 L/min to 10 L/min. Two settings were found to work best; i.e. 20 psi, 7 L/min for host-guest systems of lower molecular weight cations, and 15 psi, 6 L/min for systems involving apo- or ferri-siderophores. Lower ionization chamber temperatures were found to favor the formation of host-guest complexes with a higher mass to charge ratio, whereas higher temperatures worked well for systems involving smaller cations as guests. All system lines were purged with MeOH before injection to eliminate any residual aqueous solvent present in the system. Samples were directly injected through the inlet, or directly injected through the LC auto-sampler. Note that no separation was performed, since no LC column was in place. In the case of the latter method, a restrictor was used to provide sufficient back-pressure to the instrument. Relative intensities of the host-guest complexes were obtained by accounting for the intensity of the standard in each mixture; that is, the intensities of host-guest complex peaks were divided by the intensity of a standard present at a constant concentration in all experiments. This was done in order to correct for the different ionization efficiencies of the individual compounds involved in the formation of the host-guest complex. Tetra-n-butyl ammonium acetate (242 m/z) was used as the standard for the system of binary mixtures involving crown ether hosts and potassium, ammonium, protonated alkyl amine, and H_4DFB^+ guests. In some cases, a significant amount of variability in the intensity of the standard was observed, even at constant concentration. As a consequence, tetra-n-butyl ammonium acetate was replaced by FeDFE (658 m/z), which was then used as the standard for binary mixtures involving crown ethers or lasalocid with H_4DFB^+ and $FeHDFB^+$, as well as complex mixtures involving crown ethers and $FeHDFB^+$. FeDFE is a highly stable tris-hydroxamate siderophore complex similar to $FeHDFB^+$, but with a cyclic structure shown below and no opportunity for host-guest complex formation.

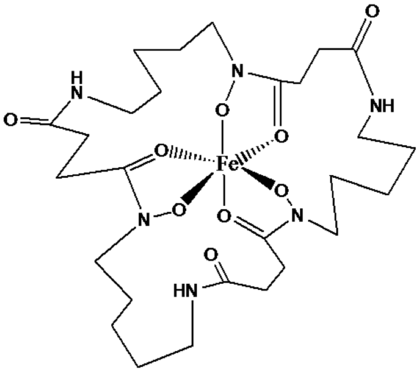

Figure 2.5 Structure of Ferrioxamine E, FeDFE

Tetra-n-butyl ammonium acetate and FeDFE were chosen as standards as they had no interaction with the host-guest complexes or crown ethers being studied, had high ionization efficiency, and a constant ESI response throughout the experiments.

All samples were prepared and run in 100% MeOH. The most abundant isotopic mass corresponding to the host-guest complex was identified by the expected m/z and the expected isotope distribution. For samples containing $FeHDFB^+$ as the guest, the isotopic distribution of the host-guest complex peak, arising from Fe and C isotopes, was used as further evidence of the presence of Fe in the complex. A spectrum simulation program from Scientific Instrument Services, Inc. was used to verify the isotopic distribution obtained experimentally. This isotope distribution calculator and mass spec plotter can be found at http://www.sisweb.com.

2.3.2.2.1 *Method Validation*

In order to determine the accuracy and precision of our experimental method, the association constants of several cation-crown ether host-guest complexes, whose association constants were previously reported in the literature using different experimental methods, were compared with association constants derived using our method. The equilibrium reaction under investigation is shown below,

$$H + G \overset{K_a}{\rightleftharpoons} H{\bullet}G \tag{2.1}$$

where H refers to the host component, i.e. the crown ether, G refers to the guest component, in this case the cation, H•G refers to the host•guest assembly, and K_a, the equilibrium constant for the association of the host-guest complex. A series of samples was analyzed at a constant K^+ concentration, and varying 18C6, B18C6, and DC18C6 concentrations, respectively, in MeOH. ESI-MS spectra for the crown ether•K^+ host-guest complexes are shown in Figure 2.6. As can be observed, the host-guest complex peaks are considerably more intense than the host peaks, indicating that the majority of the host is complexed.

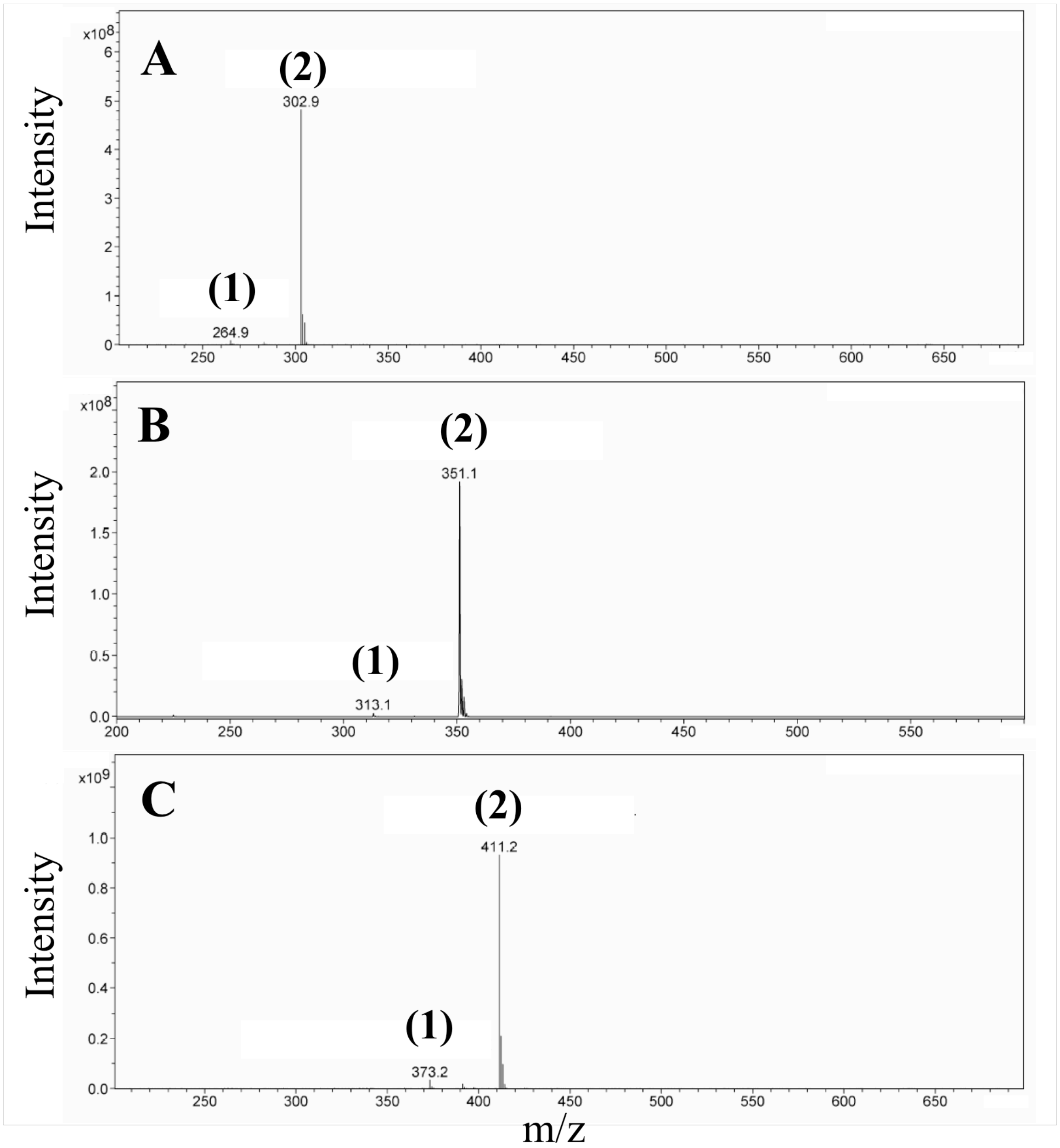

Figure 2.6 ESI mass spectrum of crown ether•K$^+$ host-guest systems. A. 18C6•K$^+$ host-guest system: (1) [18C6 + H]$^+$, (2) [18C6 + K]$^+$. B. B18C6•K$^+$ host-guest system: (1) [B18C6 + H]$^+$, (2) [B18C6 + K]$^+$. C. DC18C6•K$^+$ host-guest system: (1) [DC18C6 + H]$^+$, (2) [DC18C6 + K]$^+$. Conditions: [Crown Ether] = 0.15 mM, [KCl] = 10 mM, [tetra-n-methyl ammonium acetate] = 13 μM, in MeOH, T = 200 °C, Nebulizer = 20 psi, Dry Gas = 7 L/min. Note: The intensity of the standard is too low to be observed at this intensity scale. It was obtained through a table of intensities generated by the software.

Each of these samples contained tetra-n-butyl ammonium acetate or FeDFE as a relative intensity reference. These relative host-guest complex intensities were then plotted as a function of host concentration. The data were fit to a nonlinear regression for single-site saturation ligand binding (Equation 2.2), using SigmaPlot 9.0 software,

$$I = \frac{I_{\max}[\text{host}]}{{}^{1}\!/\!_{K_a} + [\text{host}]} \tag{2.2}$$

where I is the intensity of the host-guest complex relative to the standard, I_{max} is its maximum intensity, [host] is the molar free concentration of the crown ether host, and $1/K_a$ is the reciprocal of the equilibrium constant for the association of the host-guest complex, as shown in Equation 2.1 (Figure 2.7). This was the best model for the data, as no other model with different stoichiometries fit the data as well.

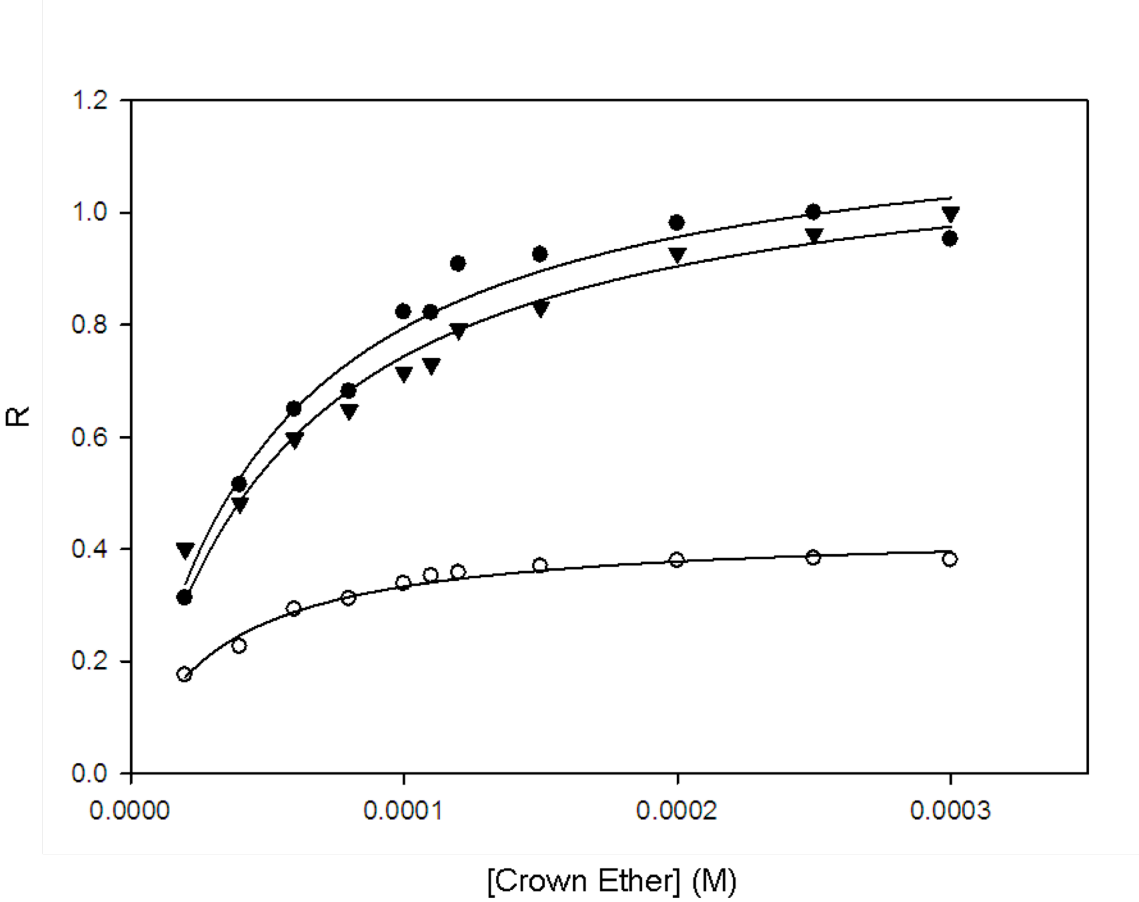

Figure 2.7 Plot of the ESI mass spectrum peak intensity ratio (R) between host-K^+ complex and standard peaks as a function of crown ether concentration. The solid line represents a non-linear least squares fit of Equation 2.2 to the data points. Each data point represents one experimental trial. (●) 18C6•K^+ complex, (▼) DC18C6•K^+ complex, (○) B18C6•K^+ complex. Conditions: [Crown Ether] = 20 μM – 300 μM, [KCl] = 10 mM, [tetra-n-butyl ammonium acetate] = 13 μM, in MeOH, T = 200 °C, Nebulizer = 20 psi, Dry Gas = 7 L/min.

Association constants (K_a) were obtained for systems involving K^+ with 18C6, B18C6, and DC18C6. These are generally in agreement with the values available in the literature in MeOH (Table 2.1). The only literature value available for comparison obtained by ESI-MS is that for K^+ and 18C6 obtained in a different solvent (MeCN). Our data yield a lower K_a values in MeOH, as expected for a hydrogen-bonding solvent, which would compete with the guest for the ether oxygen atoms of the host.

All of the results presented in Table 2.1 were analyzed in this way using Equations 2.1 and 2.2. Other stoichiometries do not fit the data obtained.

2.4 Results and Discussion

2.4.1 Determination of Host-Guest Complex Association Constants in Systems of Binary Mixtures

2.4.1.1 Protonated Amine Guests

As a prelude to our study of the second coordination shell complexation of $FeHDFB^+$ we investigated protonated amine guest/crown ether host assemblies involving NH_4^+, $CH_3NH_3^+$, and $CH_3(CH_2)_4NH_3^+$. A representative ESI-MS spectrum for the $18C6{\bullet}NH_4^+$ system is shown in Figure 2.8A, where the intense peak at 282 m/z corresponds to the host-guest complex. Additional data showing complexation of B18C6 and DC18C6 with NH_4^+ are shown in Figure 2.9. Our K_a value for $18C6{\bullet}NH_4^+$ (Figure 2.8A) is in reasonable agreement with the reported value obtained by conductivity measurements in MeOH (Table 2.1). Data are reported for this system in other non hydrogen-bonding solvents where the K_a is higher than in MeOH [49-51]. This reflects the hydrogen-bonding competition between the guest and solvent for the ether oxygen atoms.

Table 2.1 Formation constants (K_a) for binary host–guest mixtures in methanol solvent

Guest[a]	Host[b]	Log K_a[c]	Lit. values
K^+	18C6	4.29 ± 0.06	4.34[d], 4.8[e]
K^+	B18C6	4.51 ± 0.04	5.05[f]
K^+	DC18C6	4.26 ± 0.06	5.63[g]
NH_4^+	18C6	3.70 ± 0.06	4.10[h]
NH_4^+	B18C6	4.00 ± 0.06	
$CH_3NH_3^+$	18C6	4.49 ± 0.03	4.25[i]
$CH_3NH_3^+$	B18C6	4.50 ± 0.03	
$CH_3(CH_2)_4NH_3^+$	18C6	5.21 ± 0.03	
$CH_3(CH_2)_4NH_3^+$	B18C6	4.00 ± 0.04	
$CH_3(CH_2)_4NH_3^+$	DC18C6	4.40 ± 0.05	
H_4DFB^+	18C6	4.07 ± 0.05	
H_4DFB^+	B18C6	3.69 ± 0.06	
H_4DFB^+	DB18C6	4.03 ± 0.13	
H_4DFB^+	DC18C6	4.27 ± 0.05	
H_4DFB^+	Lasalocid	4.13 ± 0.09	
$FeHDFB^+$	18C6	3.70 ± 0.07	
$FeHDFB^+$	B18C6	3.40 ± 0.24	
$FeHDFB^+$	DB18C6	4.00 ± 0.13	
$FeHDFB^+$	DC18C6	4.03 ± 0.07	
$FeHDFB^+$	Lasalocid	4.53 ± 0.07	

[a] H_4DFB^+ refers to desferrioxamine B; $FeHDFB^+$ refers to ferrioxamine B

[b] 18C6, B18C6, DC18C6, and DB18C6 are 18-crown-6, benzo-18- crown-6, dicyclohexano-18-crown-6, and dibenzo-18-crown-6, respectively

[c] Host–guest association constants obtained in MeOH in this work. Error values were obtained from the non-linear least squares fit of Equation 2.2 to the data using SigmaPlot software and reflect fitting errors of the average of three measurements. Individual determinations from separate isotherms are within 5% of the average of the three runs reported.

[d] Obtained by conductivity in MeOH [51]

[e] Obtained by ESI-MS in MeCN [68]

[f] Obtained by ion-selective electrode measurements in MeOH [49,51]

[g] Obtained by calorimetry in MeOH [51]

[h] Obtained by conductivity in MeOH [51]

[i] Obtained by calorimetry in MeOH [49]

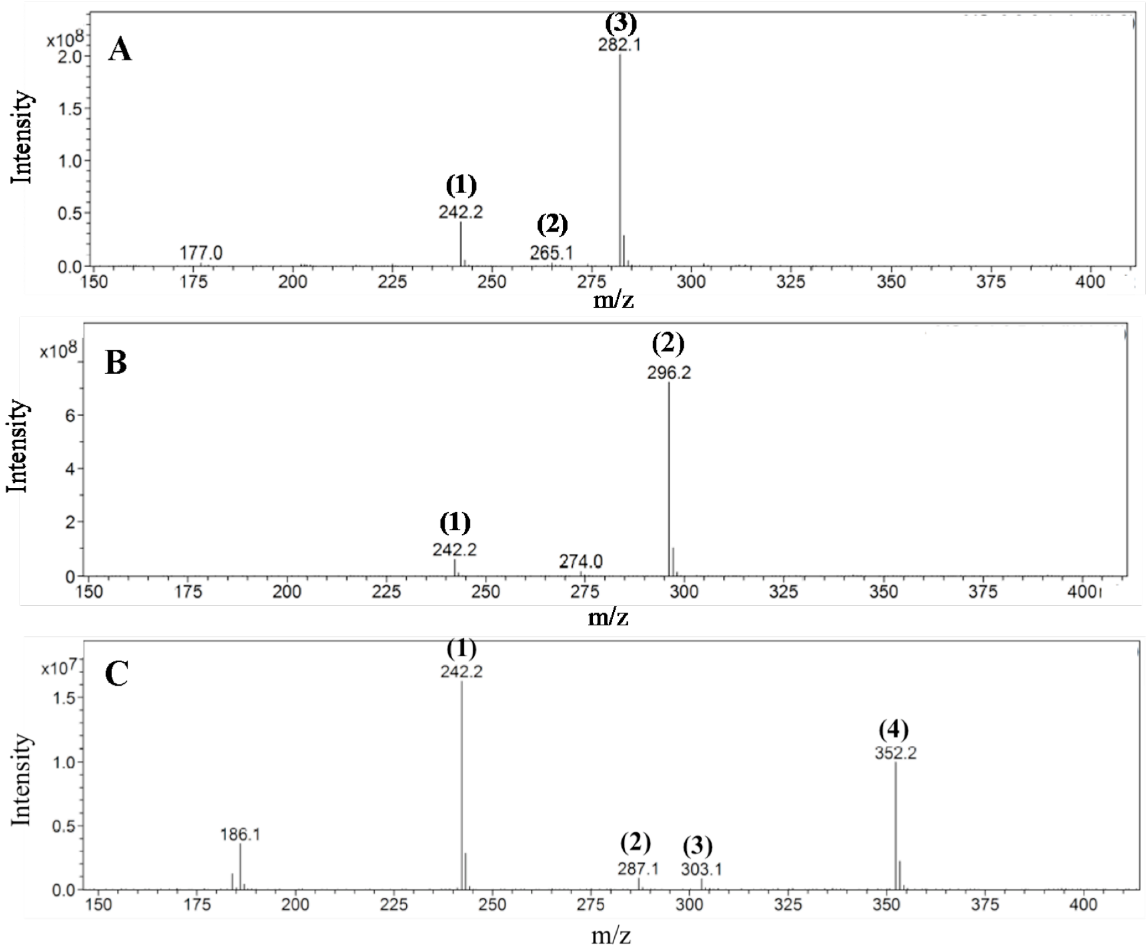

Figure 2.8 ESI mass spectrum of crown ether• protonated amine host-guest systems. A. 18C6•NH_4^+ host-guest system: (1) [Tetra-n-butyl ammonium acetate]$^+$, (2) [18C6 + H]$^+$, (3) [18C6 + NH_4]$^+$. B. 18C6•$CH_3NH_3^+$ host-guest system: (1) [Tetra-n-butyl ammonium acetate + H]$^+$, (2) [18C6 + CH_3NH_3]$^+$. C. 18C6•$CH_3(CH_2)_4NH_3^+$ host-guest system: (1) [Tetra-n-methyl ammonium acetate + H]$^+$, (2) [18C6 + Na]$^+$, (3) [18C6 + K]$^+$, (4) [18C6 + $CH_3(CH_2)_4NH_3$]$^+$. Conditions: [Crown Ether] = 0.15 mM, [amine] = 10 mM, [tetra-n-butyl ammonium acetate] = 1 mM (for C) or 13 μM (for A and B), in MeOH, T = 200 °C, Nebulizer = 20 psi, Dry Gas = 7 L/min.

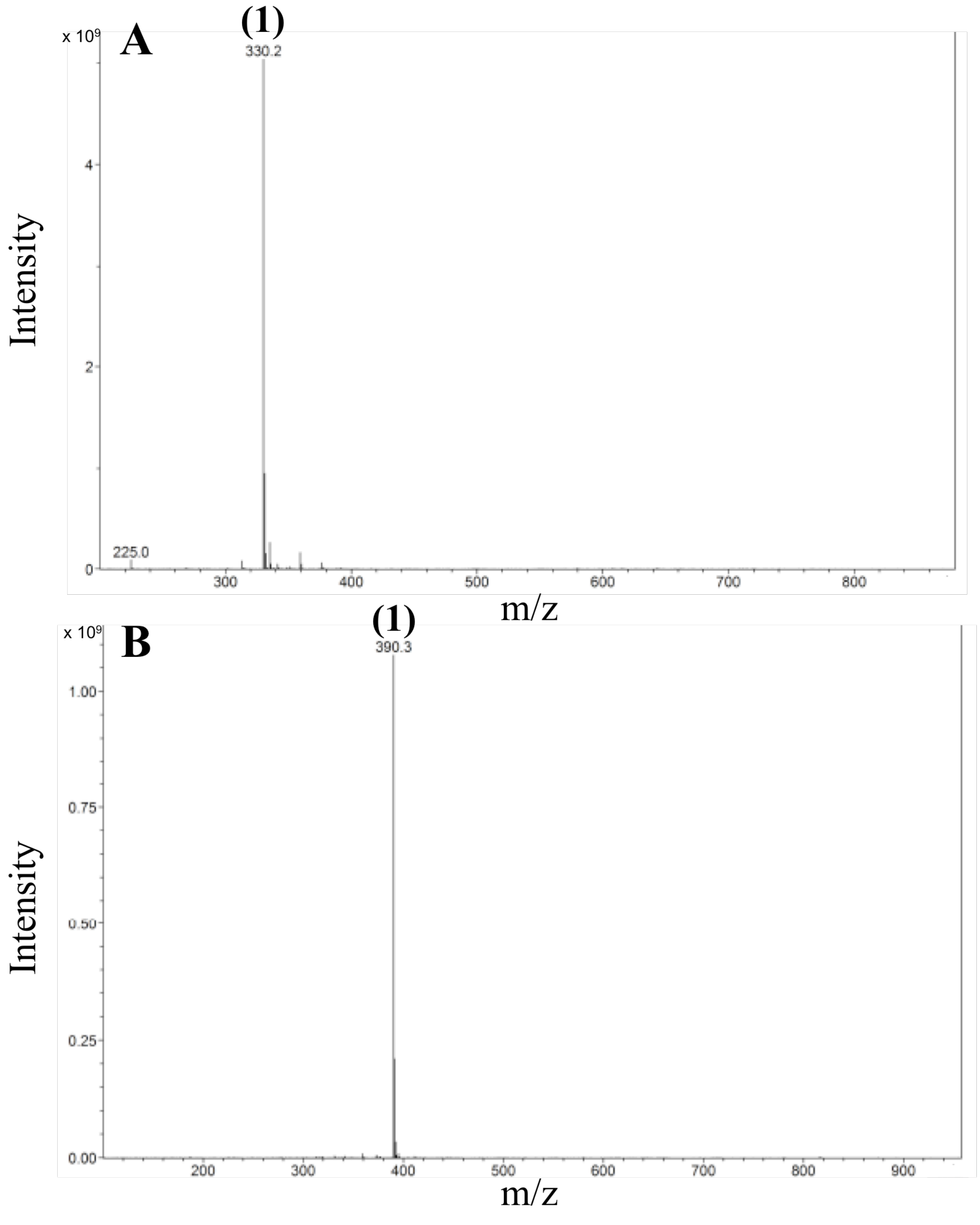

Figure 2.9 ESI mass spectrum of crown ether•ammonium host-guest systems. A. B18C6•NH_4^+ host-guest system: (1) [B18C6 + NH_4]$^+$. B. DC18C6•NH_4^+ host-guest system: (1) [DC18C6 + NH_4]$^+$. Conditions: [Crown Ether] = 0.15 mM, [ammonium] = 10 mM, [tetra-n-methyl ammonium acetate] = 13 μM in MeOH, T = 200 °C, Nebulizer = 20 psi, Dry Gas = 7 L/min. Note: The intensity of the standard is too low to be observed at this intensity scale. It was obtained through a table of intensities generated by the software.

Protonated alkyl amine guests were investigated in MeOH with 18C6, B18C6, and DC18C6 hosts. Representative spectra for protonated methylamine and pentylamine guests are shown in Figure 2.8 (B and C) with intense signals at 296 and 352 m/z corresponding to the $18C6{\bullet}CH_3NH_3^+$, and $18C6{\bullet}CH_3(CH_2)_4NH_3$+ host-guest complexes, respectively. Additional data for protonated methylamine and pentylamine guests with B18C6 and DC18C6 are shown in Figures 2.10 and 2.11. Fits of Equation 2.2 to the data are shown in Figure 2.12 and the derived K_a values are listed in Table 2.1. We find reasonable agreement between K_a values for $18C6{\bullet}CH_3NH_3^+$ in MeOH obtained here by ESI-MS and elsewhere[49] by calorimetry (Table 2.1).

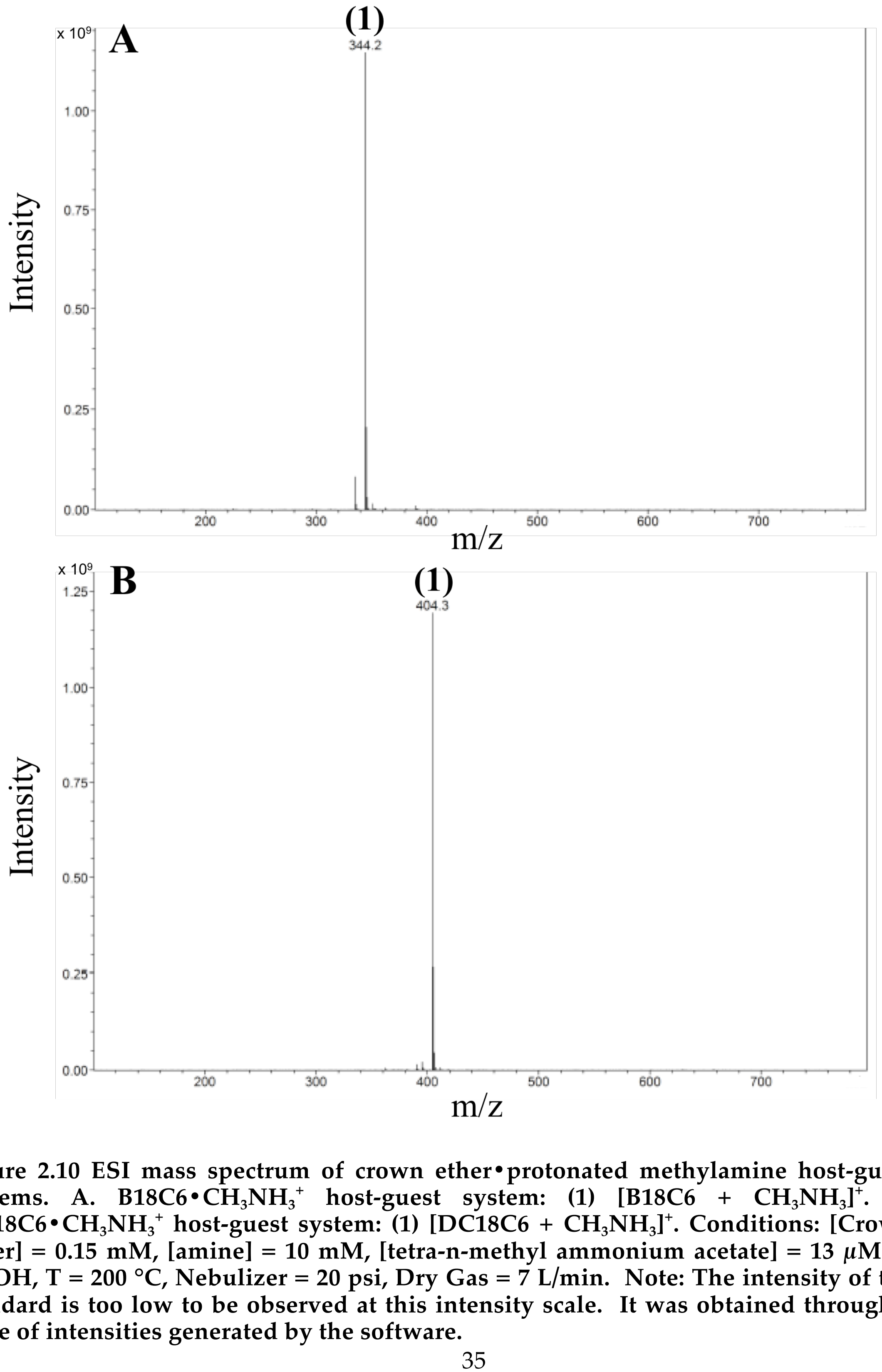

Figure 2.10 ESI mass spectrum of crown ether•protonated methylamine host-guest systems. A. B18C6•$CH_3NH_3^+$ host-guest system: (1) $[B18C6 + CH_3NH_3]^+$. B. DC18C6•$CH_3NH_3^+$ host-guest system: (1) $[DC18C6 + CH_3NH_3]^+$. Conditions: [Crown Ether] = 0.15 mM, [amine] = 10 mM, [tetra-n-methyl ammonium acetate] = 13 μM in MeOH, T = 200 °C, Nebulizer = 20 psi, Dry Gas = 7 L/min. Note: The intensity of the standard is too low to be observed at this intensity scale. It was obtained through a table of intensities generated by the software.

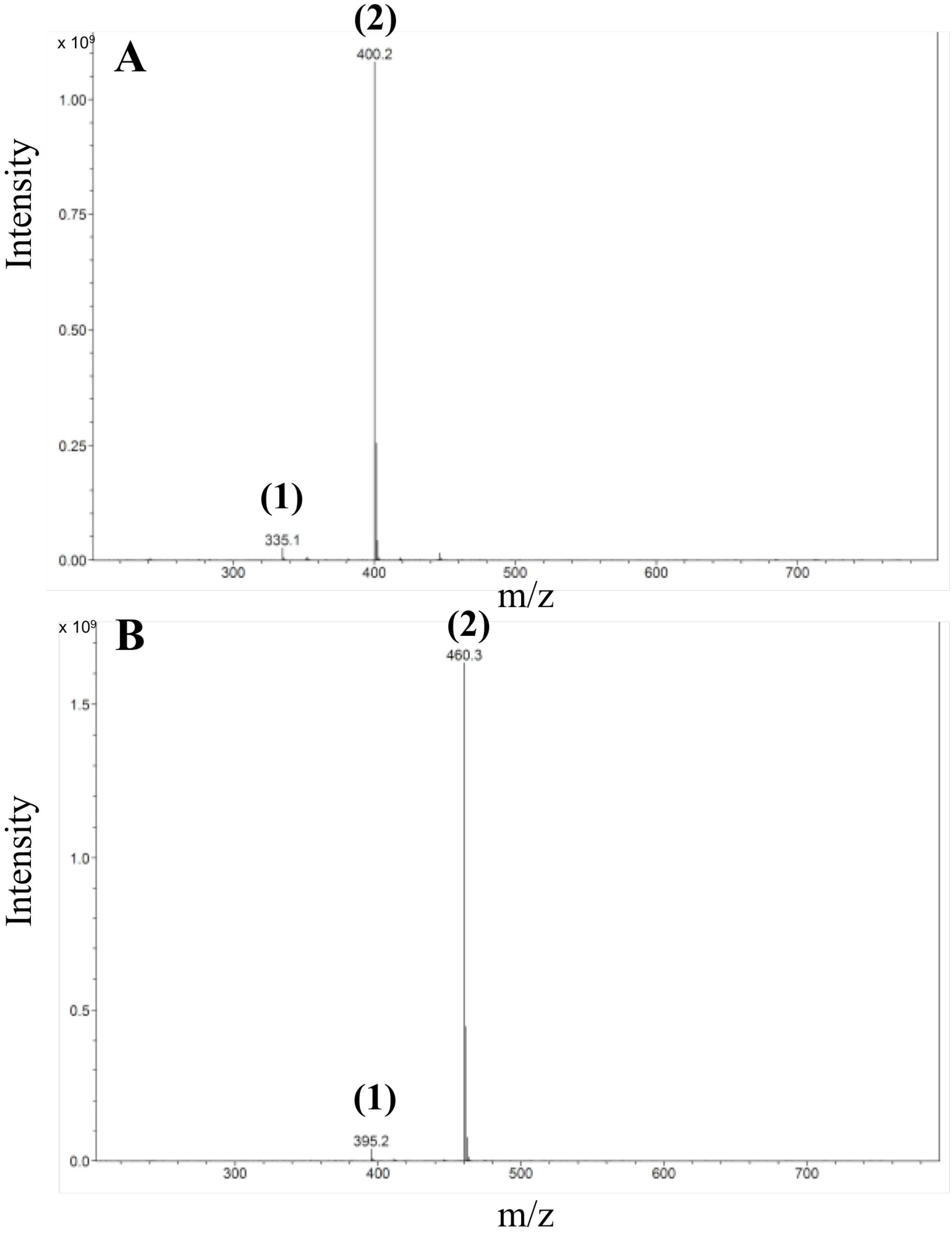

Figure 2.11 ESI mass spectrum of crown ether•protonated pentylamine host-guest systems. A. B18C6•$CH_3(CH_2)_4NH_3^+$ host-guest system: (1) $[B18C6 + H]^+$, (2) $[B18C6 + CH_3(CH_2)_4NH_3]^+$. B. DC18C6•$CH_3(CH_2)_4NH_3^+$ host-guest system: (1) $[DC18C6 + H]^+$, (2) $[DC18C6 + CH_3(CH_2)_4NH_3]^+$. Conditions: [Crown Ether] = 0.15 mM, [amine] = 10 mM, [tetra-n-methyl ammonium acetate] = 13 μM in MeOH, T = 200 °C, Nebulizer = 20 psi, Dry Gas = 7 L/min. Note: The intensity of the standard is too low to be observed at this intensity scale. It was obtained through a table of intensities generated by the software.

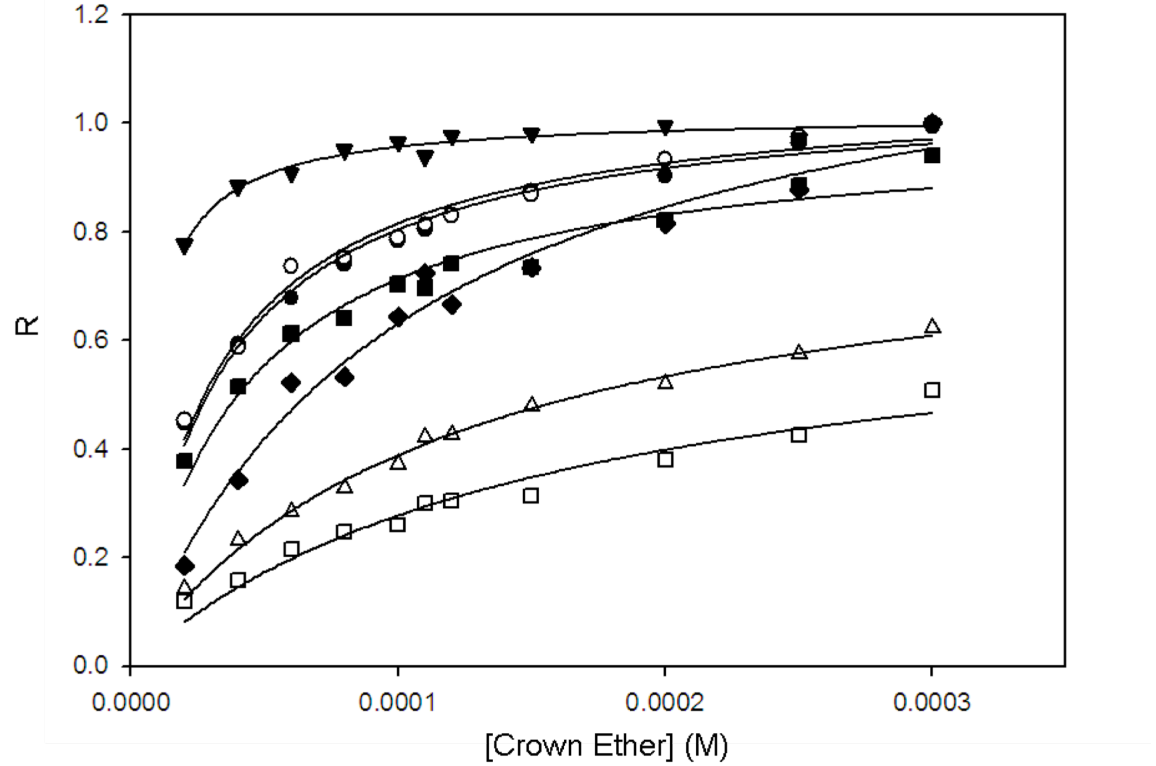

Figure 2.12 Plot of the ESI mass spectrum peak intensity ratio (R) between host-protonated amine complex and standard peaks as a function of crown ether concentration. The solid line represents a non-linear least squares fit of Equation 2.2 to the data points. Each data point represents one experimental trial. (▼) 18C6•$CH_3(CH_2)_4NH_3^+$ complex (monitored at 352 m/z) (○) B18C6•$CH_3NH_3^+$ complex (monitored at 344 m/z), (●) 18C6•$CH_3NH_3^+$ complex (monitored at 296 m/z), (◆) DC18C6•$CH_3(CH_2)_4NH_3^+$ complex (monitored at 460 m/z), (■) B18C6•NH_4^+ complex (monitored at 330 m/z), (△) B18C6•$CH_3(CH_2)_4NH_3^+$ complex (monitored at 400 m/z), (□) 18C6•NH_4^+ complex (monitored at 282 m/z). Conditions: [Crown Ether] = 20 μM - 300 μM, [NH_4Cl] = [CH_3NH_2] = [$CH_3(CH_2)_4NH_2$] = 10 mM, [tetra-n-butyl ammonium acetate] = 13 μM, in MeOH, T = 200 °C, Nebulizer = 20 psi, Dry Gas = 7 L/min.

2.4.1.2 Siderophore Guests

The host-guest complexes formed between 18C6, B18C6, DB18C6, and DC18C6 and H_4DFB^+ were studied. A representative ESI-MS spectrum of the 18C6•H_4DFB^+ system is shown in Figure 2.13. The 18C6•H_4DFB^+ complex gives an ESI-MS peak corresponding to the most abundant isotopic mass at 825 m/z, as expected. The relative host-guest complex intensities for all apo-siderophore-crown ether systems were plotted as a function of host concentration from which association constants were obtained (Figure 2.14, Table 2.1). No values exist in the literature for the host-guest complexes formed between 18C6, B18C6, and DB18C6 and H_4DFB^+ in any solvent. Our obtained K_a for the host-guest complex formed between DC18C6 and H_4DFB^+ in MeOH is lower than the literature value in $CHCl_3$ as expected due to solvent-crown ether interactions [49-51].

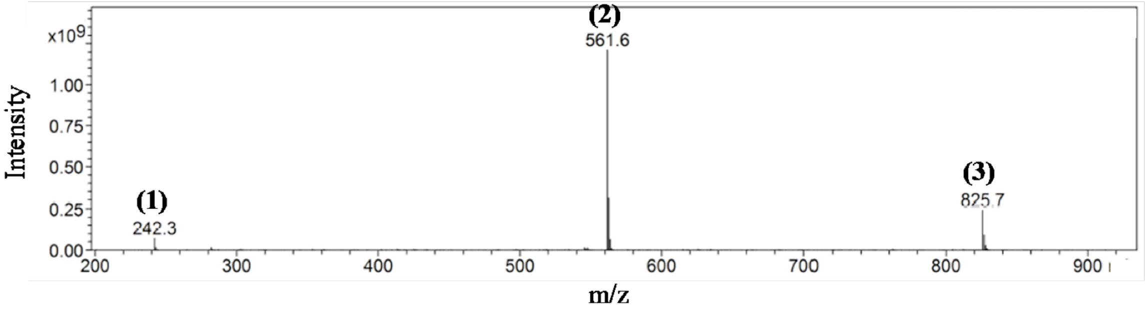

Figure 2.13 ESI mass spectrum of the 18C6•H_4DFB^+ host-guest system. (1) [Tetra-n-methyl ammonium acetate]$^+$, (2) H_4DFB^+, (3) [18C6 + H_4DFB]$^+$. Conditions: [18C6] = 150 μM, [H_4DFB^+] = 1 mM, [tetra-n-butyl ammonium acetate] = 13 μM, in MeOH, T = 200 °C, Nebulizer = 15 psi, Dry Gas = 6 L/min.

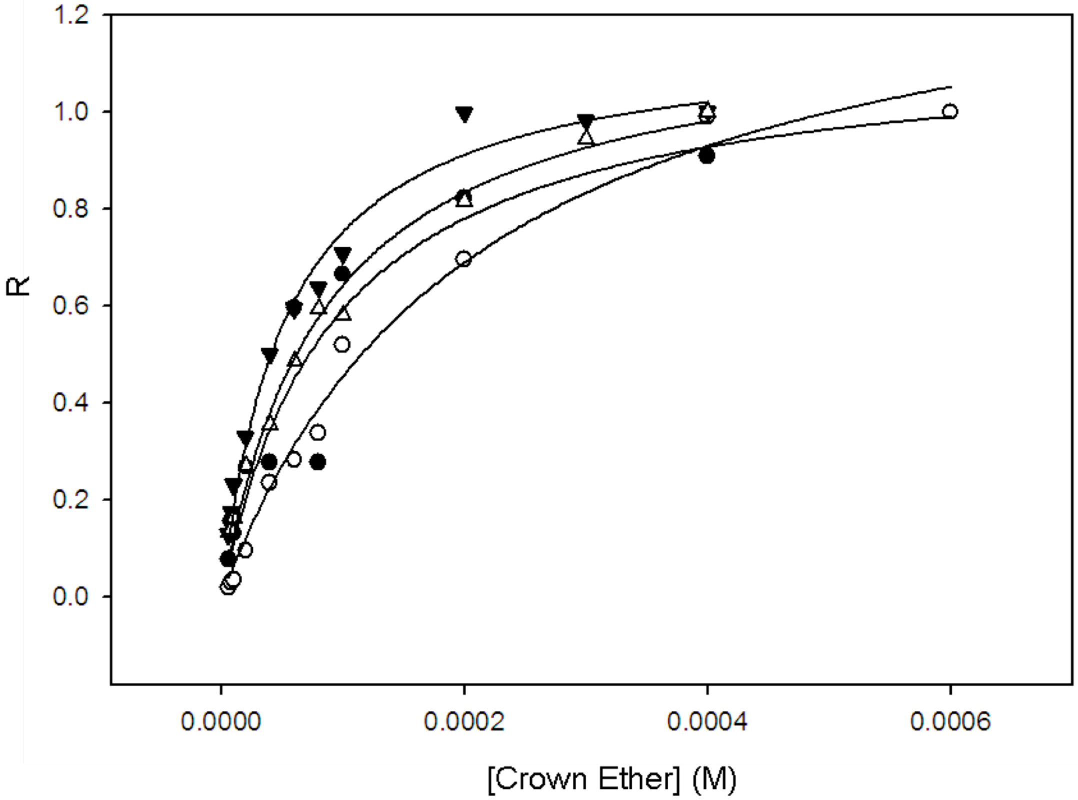

Figure 2.14 Plot of the ESI mass spectrum peak intensity ratio (R) between host-H_4DFB^+ complex and standard peaks as a function of crown ether concentration. The solid line represents a non-linear least squares fit of Equation 2.2 to the data points. Each data point represents the average of three experimental trials, with the exception of data points for the DB18C6•H_4DFB^+ assembly, where each point represents one experimental trial. (▼) DC18C6•H_4DFB^+ complex (monitored at 933 m/z), (△) 18C6•H_4DFB^+ complex (monitored at 825 m/z), (○) B18C6•H_4DFB^+ complex (monitored at 873 m/z), (●) DB18C6•H_4DFB^+ complex (monitored at 921 m/z) Conditions: [Crown Ether] = 6 μM - 600 μM, [H_4DFB^+] = 1 mM, [FeDFE] = 0.1 mM, or [tetra-n-butyl ammonium acetate] = 13 μM in MeOH, T = 200 °C, Nebulizer = 15 psi, Dry Gas = 6 L/min.

Host-guest complexes between a series of crown ethers and the iron-loaded siderophore FeHDFB$^+$ were studied. A representative ESI-MS spectrum of the 18C6•FeHDFB$^+$ system is shown in Figure 2.15. This complex gives an ESI-MS peak with a most abundant isotopic mass of 878 m/z, as expected. The isotopic distribution centered on the host-guest complex peak for the 18C6•FeHDFB$^+$ system is shown in Figure 2.16. This distribution is consistent with the natural isotope distribution of Fe (^{56}Fe(91.8%), ^{54}Fe(5.8%), ^{57}Fe(2.1%)), which provides further evidence of the presence of Fe in a host-guest complex with z = 1 [70]. A spectrum simulation based on the singly-charged 18C6•FeHDFB$^+$ host-guest complex produced an isotopic distribution consistent with that observed experimentally, as shown in Figure 2.17. Additional data showing host-guest complex formation between B18C6, DC18C6, and DB18C6 with FeHDFB$^+$ are shown in Figure 2.18.

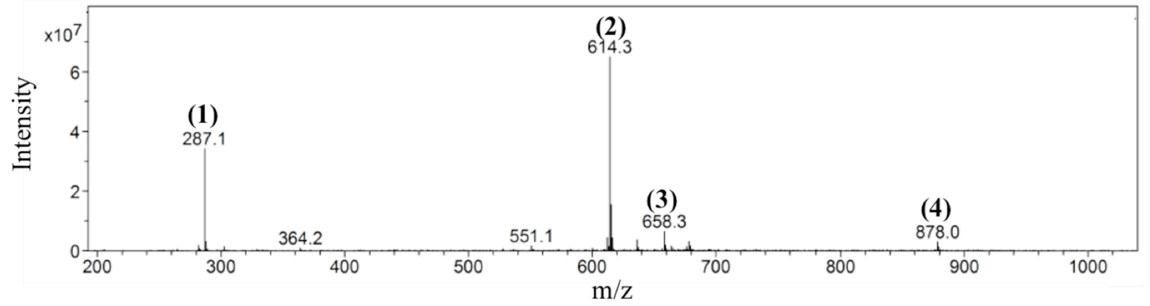

Figure 2.15 ESI mass spectrum of the 18C6•FeHDFB$^+$ host-guest system. (1) [18C6 + H]$^+$, (2) FeHDFB$^+$, (3) [FeDFE + H]$^+$, (4) [18C6 + FeHDFB]$^+$. Conditions: [18C6] = 0.3 mM, [FeHDFB$^+$] = 1 mM, [FeDFE] = 1 mM, in MeOH, T = 125 °C, Nebulizer = 15 psi, Dry Gas = 6 L/min.

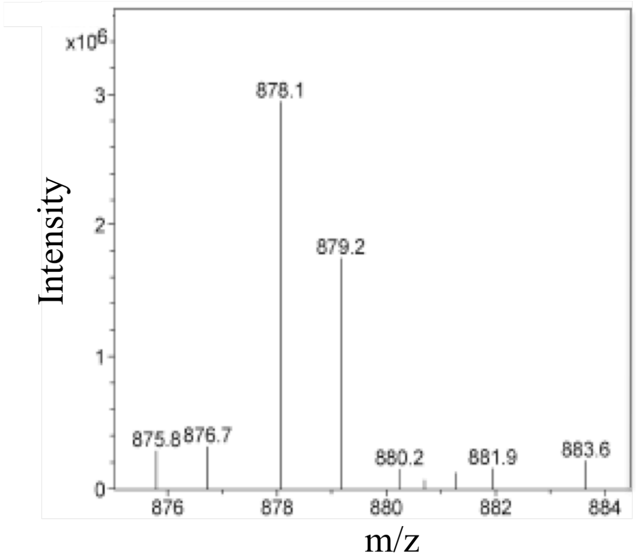

Figure 2.16 Isotopic distribution centered around the host-guest complex peak of the 18C6•FeHDFB$^+$ host-guest system. Conditions: [18C6] = 0.3 mM, [FeHDFB$^+$] = 1 mM, [FeDFE] = 1 mM, in MeOH, T = 125 °C, Nebulizer = 15 psi, Dry Gas = 6 L/min. This isotope distribution calculator and mass spec plotter can be found at http://www.sisweb.com.

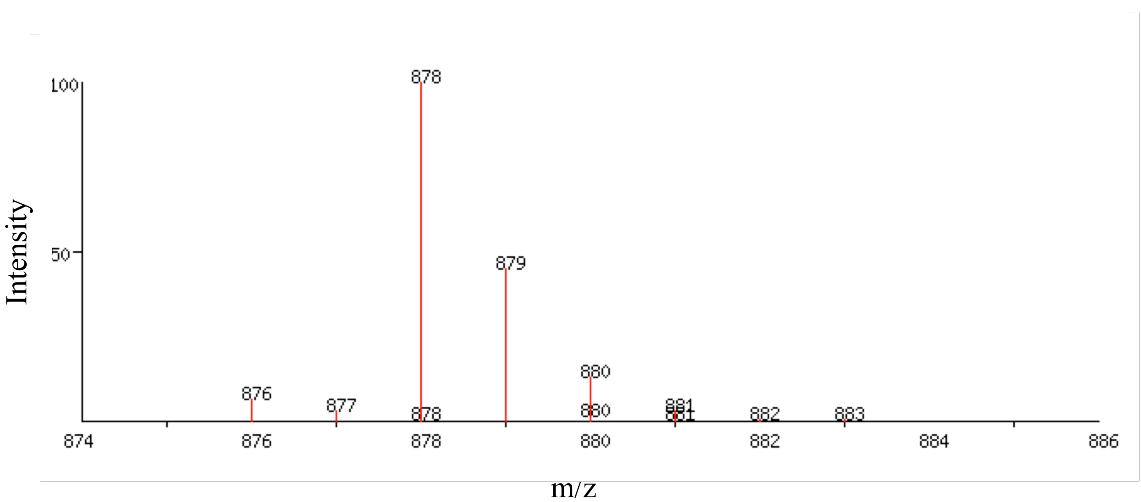

Figure 2.17 Spectrum simulation of the isotopic distribution centered around the host-guest complex peak of the 18C6•FeHDFB$^+$ host-guest system.

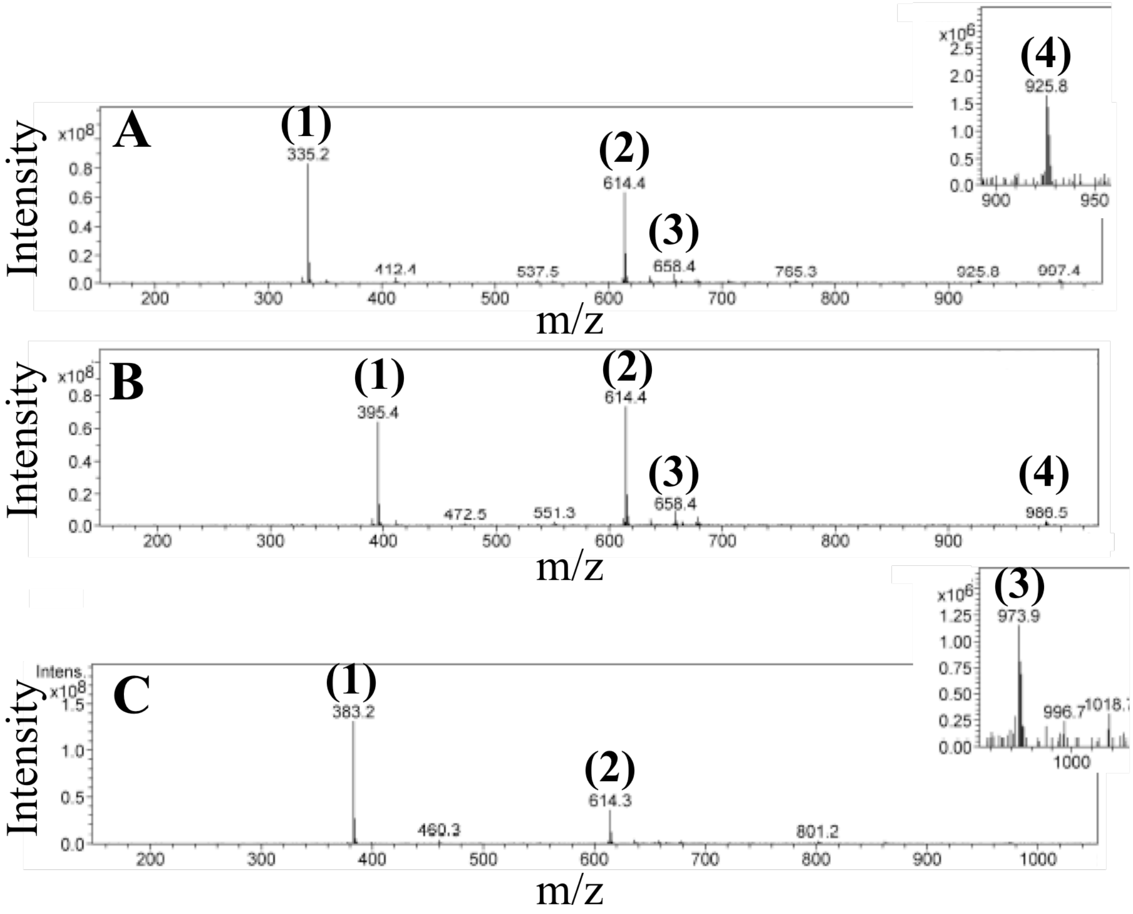

Figure 2.18 ESI mass spectrum of crown ether•FeHDFB$^+$ host-guest systems. A. (1) [B18C6 + Na]$^+$, (2) FeHDFB$^+$, (3) [FeDFE + H]$^+$, (4) [B18C6 + FeHDFB]$^+$. B. (1) [DC18C6 + Na]$^+$, (2) FeHDFB$^+$, (3) [FeDFE + H]$^+$, (4) [DC18C6 + FeHDFB]$^+$. C. (1) [DB18C6 + Na]$^+$, (2) FeHDFB$^+$, (3) [FeDFE + H]$^+$, (4) [DB18C6 + FeHDFB]$^+$. Conditions: [Crown Ether] = 0.3 mM, [FeHDFB$^+$] = 1 mM, [FeDFE] = 1 mM, in MeOH, T = 125 °C, Nebulizer = 15 psi, Dry Gas = 6 L/min. Note: Standard intensity is too small to be observed at the scale shown in C, but was added at the concentration listed, and its intensity was obtained through a table of intensities generated by the software.

Following the procedure mentioned previously, host-guest association constants were obtained (Figure 2.19, Table 2.1). As with host-guest complex systems of crown ethers and H_4DFB^+, no literature values exist for host-guest complexes of crown ethers and FeHDFB$^+$ in MeOH. However, our obtained association constants again fall within the range that would be expected for MeOH based on literature association constants in other solvents [49-51].

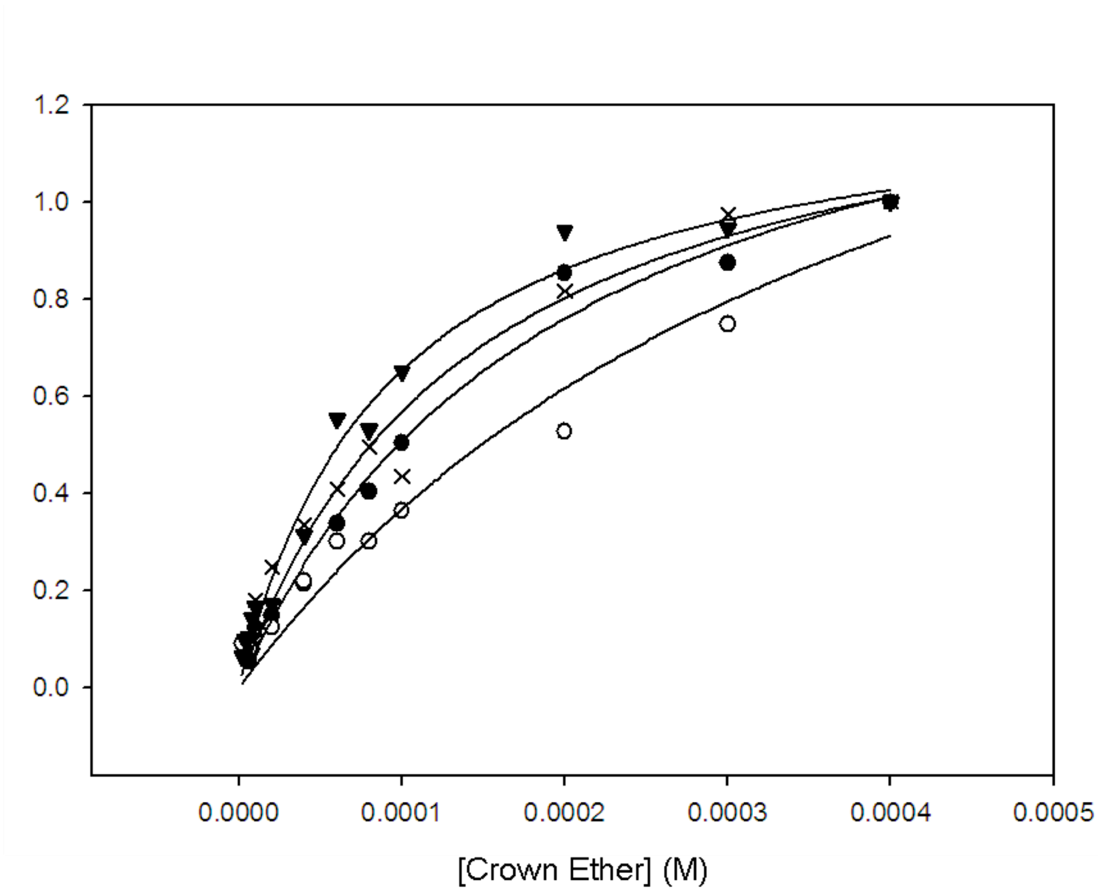

Figure 2.19 Plot of the ESI mass spectrum peak intensity ratio (R) between host-FeHDFB$^+$ complex and standard peaks as a function of crown ether concentration. The solid line represents a non-linear least squares fit of Equation 2.2 to the data points. Each data point represents the average of three experimental trials. (▼) 18C6•FeHDFB$^+$ complex (monitored at 878 m/z), (×) DC18C6•FeHDFB$^+$ complex (monitored at 986 m/z), (●) B18C6•FeHDFB$^+$ complex (monitored at 927 m/z), (○) DB18C6•FeHDFB$^+$ complex (monitored at 974 m/z). Conditions: [Crown Ether] = 6 μM - 400 μM, [FeHDFB$^+$] = 1 mM, [FeDFE] = 0.1 mM, in MeOH, T = 125 °C, Nebulizer = 15 psi, Dry Gas = 6 L/min.

2.4.1.3 Open Chain Ionophore Hosts

The host-guest complexes formed between lasalocid A, a polyether carboxylic acid antibiotic, and H_4DFB^+ and $FeHDFB^+$ were studied. Unlike cyclic crown ethers, lasalocid A has an open chain structure and acidic hydrogen, which can lead to vastly different host-guest complexation behavior [71].

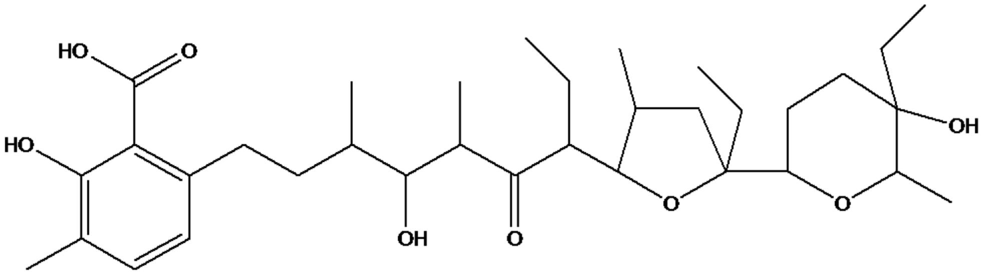

Figure 2.20 Structure of Lasalocid A

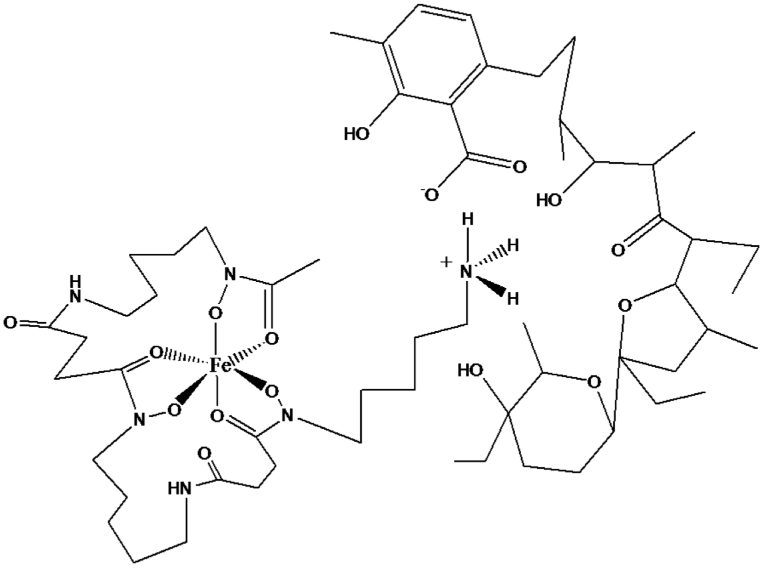

Figure 2.21 Structure of the lasalocid•FeHDFB$^+$ host-guest complex

Lasalocid alone was observed as a Na^+ adduct in the ESI-MS spectrum. The lasalocid•H_4DFB^+ host-guest complex was observed at 1151 m/z and the lasalocid•$FeHDFB^+$ host-guest complex was observed as a Na^+ adduct at 1226 m/z (Figures 2.22 and 2.23).

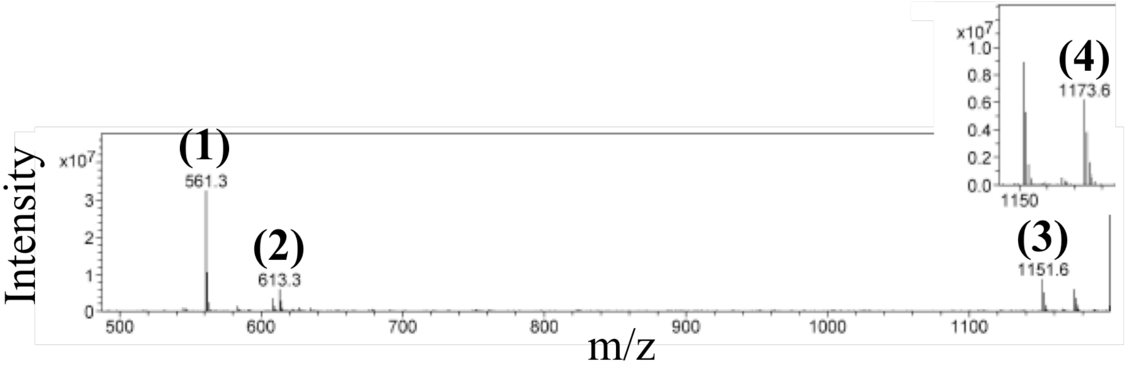

Figure 2.22 ESI mass spectrum of the lasalocid A•H_4DFB^+ host-guest system. (1) H_4DFB^+, (2) [lasalocid A + Na]$^+$, (3) [lasalocid A + H_4DFB]$^+$, (4) [lasalocid A + H_4DFB + Na]$^+$. Conditions: [lasalocid A] = 0.3 mM, [$FeHDFB^+$] = 1 mM, [FeDFE] = 1 mM, in MeOH, T = 125 °C, Nebulizer = 15 psi, Dry Gas = 6 L/min. Note: The intensity of the standard is too low to be observed at this intensity scale. It was obtained through a table of intensities generated by the software.

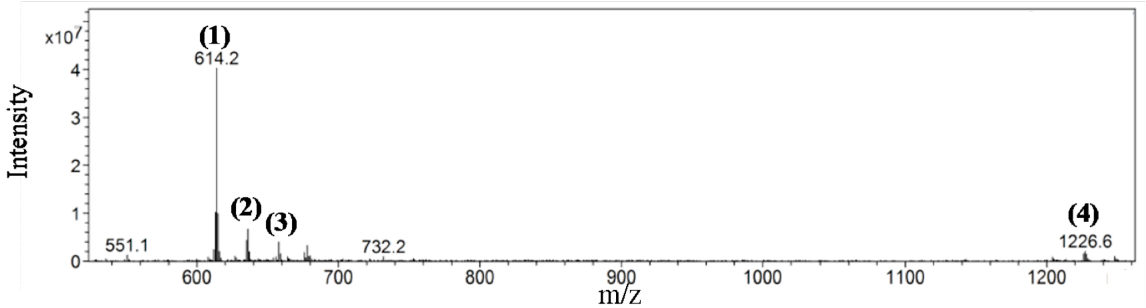

Figure 2.23 ESI mass spectrum of the lasalocid A•$FeHDFB^+$ host-guest system. (1) $FeHDFB^+$, (2) [FeHDFB + Na]$^+$, (3) [FeDFE + H]$^+$, (4) [lasalocid A + FeHDFB + Na]$^+$. Conditions: [lasalocid A] = 0.3 mM, [$FeHDFB^+$] = 1 mM, [FeDFE] = 1 mM, in MeOH, T = 125 °C, Nebulizer = 15 psi, Dry Gas = 6 L/min.

Following the procedure previously described, the host-guest complex intensities were monitored and association constants were obtained (Figure 2.24, Table 2.1). Although we do not have direct proof, we propose the structure shown above (Figure 2.21) for the lasalocid•FeHDFB$^+$ host-guest assembly, based on the similarity of the K_a value with those observed for the macrocyle hosts, and previous studies [71].

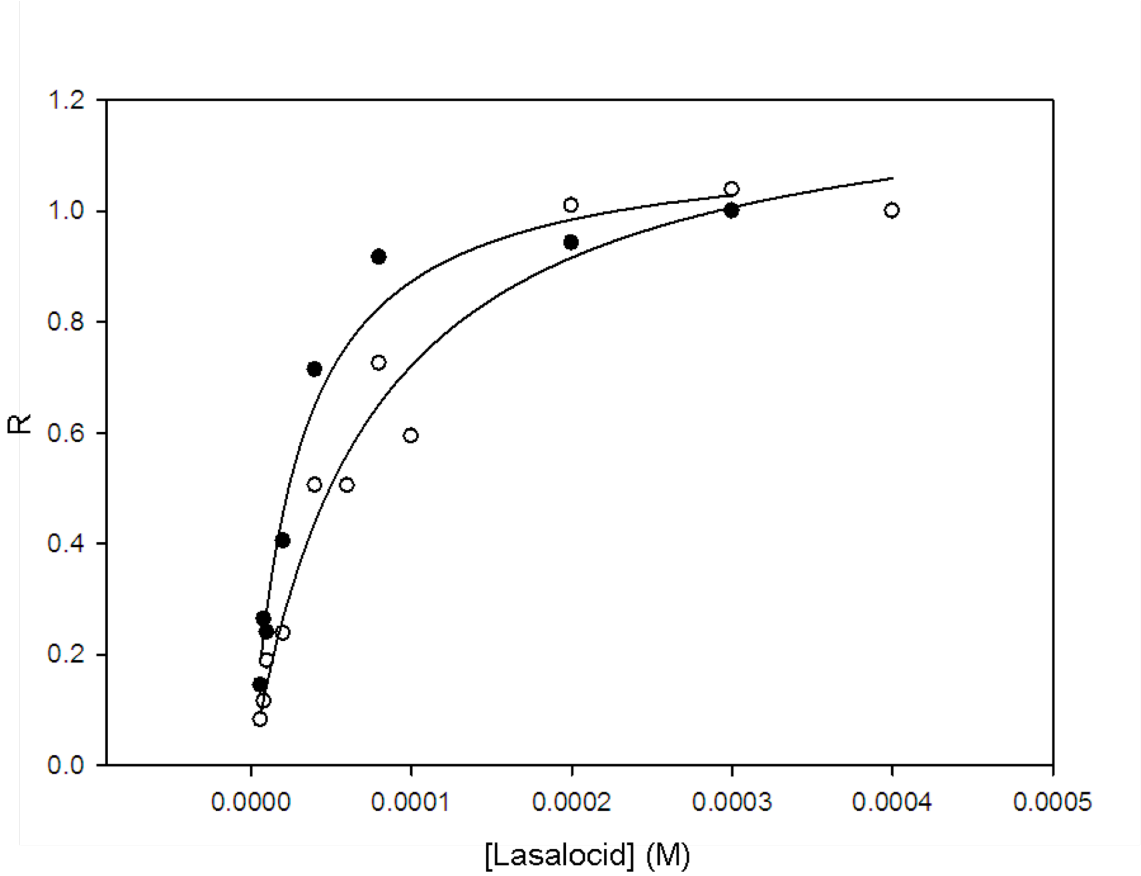

Figure 2.24 Plot of the ESI mass spectrum peak intensity ratio (R) between lasalocid A-guest complex and standard peaks as a function of crown ether concentration. The solid line represents a non-linear least squares fit of Equation 2.2 to the data points. Each data point represents the average of three experimental trials. (●) Lasalocid A•FeHDFB/Na$^+$ adduct complex (monitored at 1226 m/z), (○) Lasalocid A•H_4DFB^+ complex (monitored at 1151 m/z). Conditions: [Lasalocid A] = 6 μM - 400 μM, [FeHDFB$^+$] or [H_4DFB^+] = 1 mM, [FeDFE] = 0.1 mM, in MeOH, T = 125 °C, Nebulizer = 15 psi, Dry Gas = 6 L/min.

2.4.2 Determination of Binding Selectivities in Systems of Complex Mixtures

The applicability of the ESI-MS method for systems of complex mixtures, i.e. mixtures containing two hosts competing for one guest, was explored. This method is illustrated in Equation 2.3 and described below using 18C6, B18C6, and DC18C6 as the competing hosts, and FeHDFB$^+$ as the guest.

$$H_1 + G \overset{K_{H_1}^{mix}}{\rightleftharpoons} H_1{\bullet}G$$

$$H_2 + G \overset{K_{H_2}^{mix}}{\rightleftharpoons} H_2{\bullet}G \tag{2.3}$$

A sample containing 18C6, DC18C6, and FeHDFB$^+$ in a 1:1:20 ratio was analyzed. The spectrum is shown in Figure 2.25, which includes different peak intensities for the host-guest complexes of interest. This difference in signal intensities is related to both the concentration and the ionization efficiencies of the host-guest complexes formed. We factored out the differences in ionization efficiencies as described below so that the signal was directly related to the concentration of host-guest assembly.

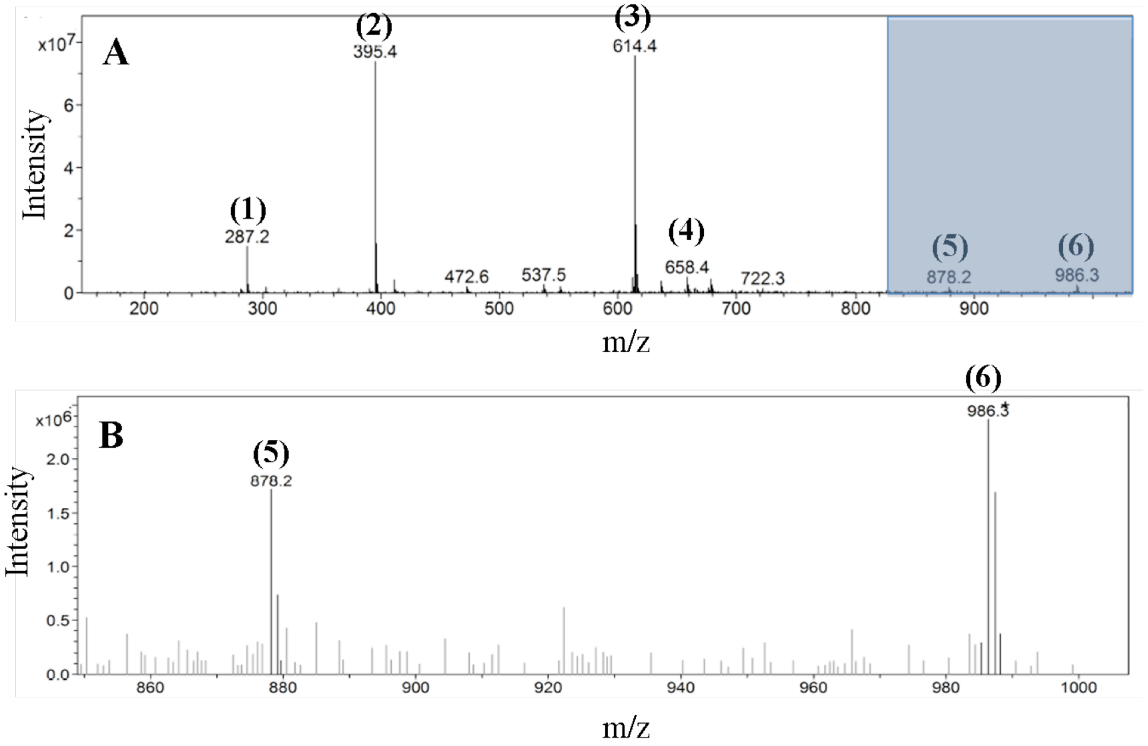

Figure 2.25 ESI mass spectrum of the complex mixture of 18C6/DC18C6•FeHDFB$^+$. A. Extended view (0-1000 m/z), (1) [18C6 + H]$^+$, (2) [DC18C6 + H]$^+$, (3) FeHDFB$^+$, (4) [FeDFE + H]$^+$, (5) [18C6 + FeHDFB]$^+$, (6) [DC18C6 + FeHDFB]$^+$. B. Focused view of shaded region of spectrum A (850-1000 m/z). Conditions: [18C6] = [DC18C6] = 6 μM - 600 μM, [FeHDFB$^+$] = 1 mM, [FeDFE] = 0.1 mM, in MeOH, T = 125 °C, Nebulizer = 15 psi, Dry Gas = 6 L/min.

Differences in ionization efficiencies have previously been accounted for in different ways [66-69]. Our approach uses a simple system of calibration plots. Calibration plots were made for each of the individual binary system host-guest complexes present in the complex mixture sample. A series of samples was analyzed at a constant FeHDFB$^+$ concentration, and varying crown ether concentration. The relative host-guest complex intensities obtained from these samples were plotted as a function of host-guest complex concentration (Figure 2.26).

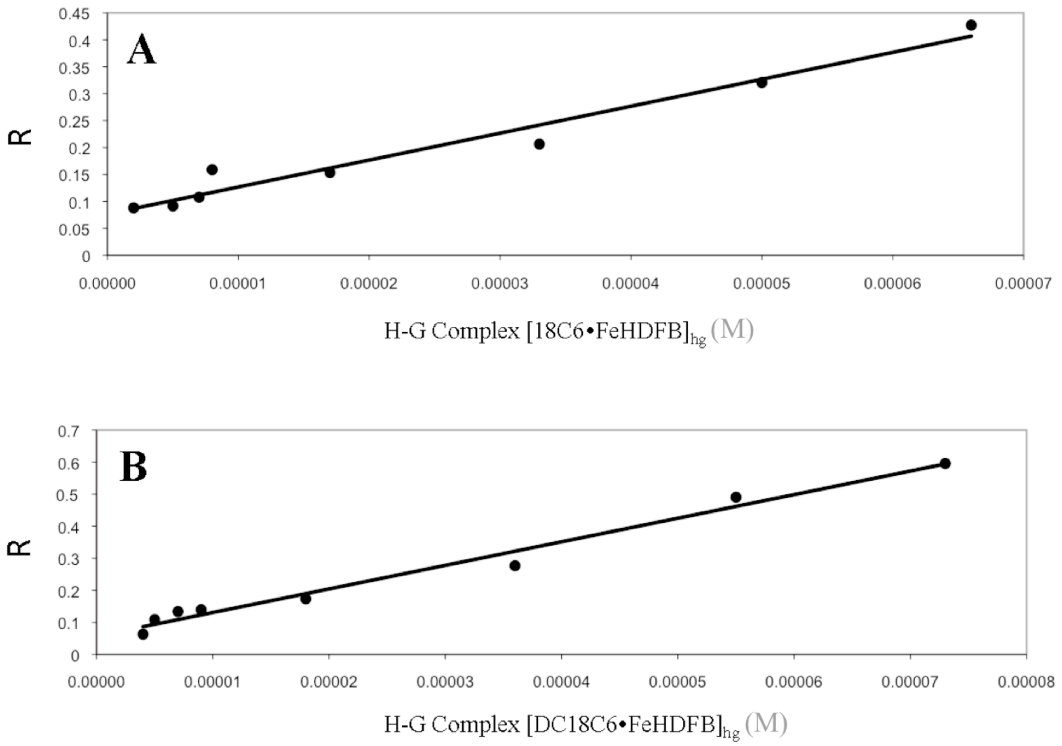

Figure 2.26 Plot of the ESI mass spectrum peak intensity ratio (R) as a function of host-guest complex concentration for systems of DC18C6•FeHDFB$^+$ (A) and 18C6•FeHDFB$^+$ (B). Each data point represents one experimental trial. Conditions: [18C6] = [DC18C6]= 6 μM - 600 μM, [FeHDFB$^+$] = 1 mM, [FeDFE] = 0.1 mM, in MeOH, T = 125 °C, Nebulizer = 15 psi, Dry Gas = 6 L/min.

These concentrations were calculated from the association constants obtained using systems of binary mixtures, as described above. The host-guest complex intensities were converted to host-guest complex concentrations from these calibration plots. Using a series of equilibrium reactions for the DC18C6•FeHDFB$^+$ and 18C6•FeHDFB$^+$ systems (Equation 2.4), and their respective equilibrium expressions, an equation for the binding selectivity was obtained, as shown in Equation 2.5.

$$DC18C6 + FeHDFB^+ \overset{K^{mix}_{DC18C6}}{\rightleftharpoons} DC18C6{\cdot}FeHDFB^+$$

$$18C6 + FeHDFB^+ \overset{K^{mix}_{18C6}}{\rightleftharpoons} 18C6{\cdot}FeHDFB^+ \tag{2.4}$$

$$\left(\frac{K^{mix}_{DC18C6}}{K^{mix}_{18C6}}\right) = \frac{[\mathrm{DC18C6{\cdot}FeHDFB^+}][\mathrm{18C6}]}{[\mathrm{18C6{\cdot}FeHDFB^+}][\mathrm{DC18C6}]} \tag{2.5}$$

Using the above equations and the data provided in Figure 2.26, the binding selectivity ($K^{mix}_{DC18C6}/K^{mix}_{18C6}$) for the DC18C6•FeHDFB$^+$ and 18C6•FeHDFB$^+$ mixed system was found to be 2.0. This experimental value compares well with the binding selectivity ratio calculated from the individual association constants (2.13, Table 2.1) obtained through the system of binary mixtures using the method discussed in the previous section.

We have also used the complex mixture competition technique for other crown ether mixtures and FeHDFB$^+$; e.g. 18C6 and B18C6. Here the host-guest binding selectivity was found to be 2.06, in excellent agreement with that calculated from the individual association constants (Table 2.1) obtained for the system of binary mixtures, 2.0.

2.5 *Summary and Conclusions*

We have presented a strategy by which ESI-MS has been extended to derive host-guest association constants and binding affinities for systems of binary and complex mixtures with applications to crown ether and linear ionophore hosts, and ammonium and protonated alkyl amine guests, as well as to siderophore-ionophore supramolecular assemblies involving an apo and ferri-siderophore guest. It is significant that we are able to study in the gas phase second coordination shell host-guest complexes formed in solution.

Our results in MeOH solvent demonstrate a general lack of sensitivity to changes in host and guest structure for the systems investigated (Table 2.1). However, we find that the ferri-siderophore $FeHDFB^+$ exhibits slightly lower affinity for complexation by the various crown ethers than does the iron-free apo form, H_4DFB^+. This was also observed for DC18C6 in $CHCl_3$ using a liquid – liquid extraction method and may be due to a small steric effect [32]. We also note that the more flexible open chain lasalocid host forms slightly more stable host-guest complexes with H_4DFB^+ and $FeHDFB^+$ than the cyclic crown ethers, perhaps for steric reasons (Table 2.1).

Further, we have established that competitive host-guest association constants for complex mixtures may be obtained by ESI-MS. These data would be very difficult or impossible to obtain by other methods.

3. Mass Spectral Determination of Host-Guest Assemblies Involving Novel Redox Active Aza Crown Ether Hosts and the Thermodynamic Parameters Associated with These Interactions

3.1 *Background and Significance*

We previously developed a method in which ESI-MS was successfully used to determine association constants and binding selectivities for host–guest systems of binary and complex mixtures, including a metal complex guest (Chapter 2). Specifically, our previous study involved the complexation of ammonium, protonated methylamine and pentylamine, and H_4DFB^+ with 18C6, B18C6, DC18C6, and DB18C6 macrocycles, and the linear ionophore lasalocid. The complexation of a metal complex guest, i.e. $FeHDFB^+$, with these macrocycles and the linear ionophore host was also studied [37].

Crown ethers such as the ones discussed above can complex different ions depending on the size, shape and donor atoms in the cavity. Our interest lies in modulating the uptake or release of these ionic guests by using externally controlled methods. Redox-active macrocyclic ligands are functional host molecules that can sense the presence of a guest and whose complexation ability can be altered through redox processes [72]. Macrocycles such as these, whose properties can be altered by physical and chemical means, have many potential uses, including redox switches, sensors, transport agents, and electrocatalysts [73-75].

Wurster's crowns are a class of aza crown ethers that incorporate the redox active moiety N,N,N′,N′-tetraalkyl-1,4-phenylenediamine, a derivative of Wurster's Reagent [76] (Figure 3.1, **I**) [77-82].

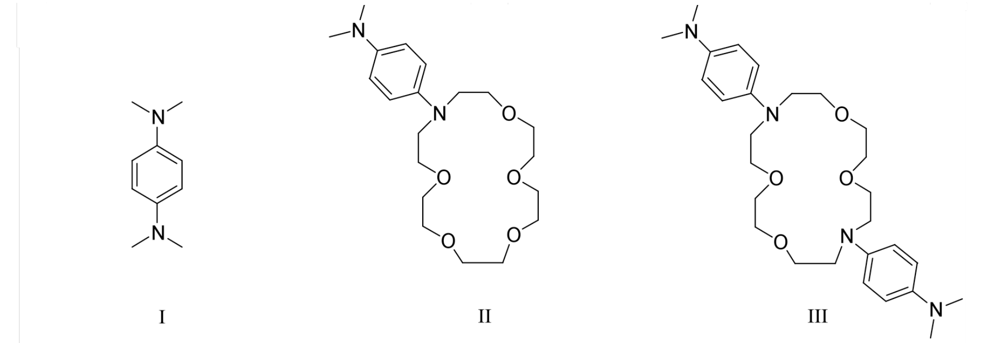

I II III

N,N,N',N'-tetramethyl-*p*-phenylenediamine Mono substituted Wurster's Crown Bis substituted Wurster's Crown

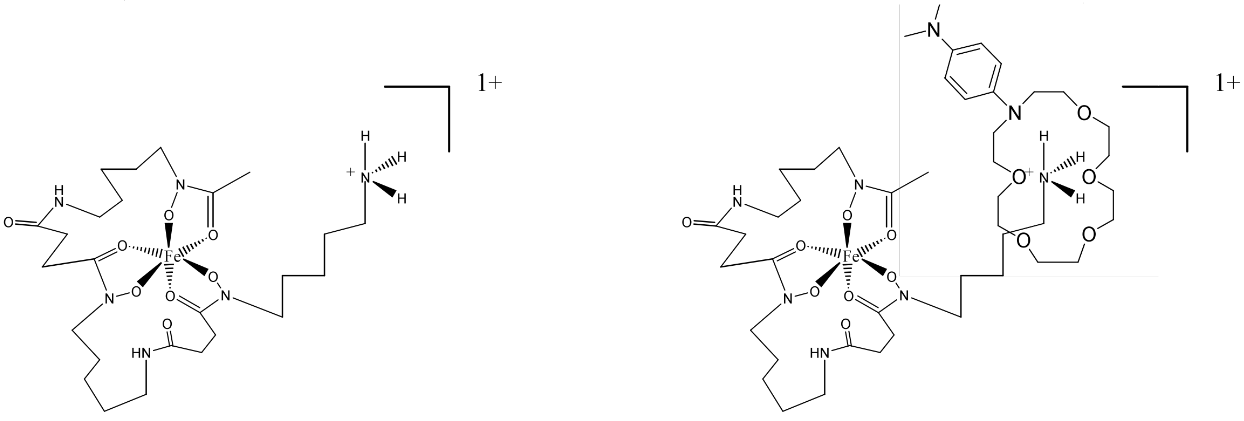

Ferrioxamine B, $FeHDFB^+$ $FeHDFB^+$•II Host-Guest Complex

Figure 3.1 Structures of aza-crown hosts, siderophore guest, and host-guest assembly.

The redox properties of Wurster's crowns and their affinity for cations have been studied [72,73,79-85]. Similar to their Wuster's reagent counterpart, Wurster's crowns undergo two successive one electron oxidations resulting in cationic hosts, Figure 3.2 [72]. In both cases, the first oxidation generates a radical cation. Removal of a second electron results in a quinoid-type molecule, in which a positive charge is localized on the N atoms [72].

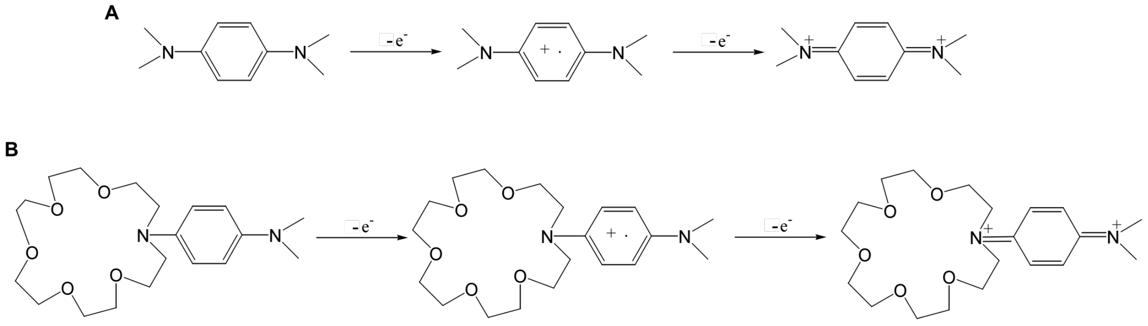

Figure 3.2 Scheme showing the two successive one electron oxidations of A. N,N,N′,N′-tetraalkyl-1,4-phenylenediamine (I) and B. Wurster's crown II. Adapted from Backer, M. D.; Hureau, M.; Depriester, M.; Deletoille, A.; Sargent, A. L.; Forshee, P. B.; Sibert, J. W. *J. Electroanal. Chem.* 2008, *612*, 97.

The vast majority of Wurster's crowns studied are redox-active analogues of crown ethers [72,73,79-85]. These systems display affinities for Group I and Group II metal ions because of their predominance of hard oxygen-donor atoms [84] and form an additional interaction with cationic guests through the pendant nitrogen moiety in the dimethylamino group [82]. The interactions between a variety of Wurster's crowns and Group I and Group II metal ions have been well characterized [73,79-86], but to date there are no examples in the literature of host-guest complex formation between Wurster's crowns and large assemblies containing transition metal-ions, or of the affinities between these hosts and guests.

3.1.1 Electrochemical Behavior of Novel Redox Active Aza Crown Ether Hosts

Our interest in these aza crown ether systems stems from the unique voltammetric behavior they display. Previous work in the Crumbliss group has found that a shift in redox potential towards more positive values is observed upon addition of a cationic guest to a solution of either a mono-substituted Wurster's crown (Figure 3.1, **II**) or a bis-substituted Wurster's crown (Figure 3.1, **III**) [38,87].

Wurster’s salt (Figure 3.1, **I**) exhibits reversible voltammetry in acetonitrile with $E_{1/2}$ = 148 mV vs Ag/AgCl [38,87]. When incorporated into the 18C6 cavity, this redox couple remains reversible and is negligibly shifted to 150 mV vs Ag/AgCl for **II** and 156 mV vs Ag/AgCl for **III** (Table 3.1). Similar behavior is observed in chloroform, although with less ideal reversible behavior (Table 3.2). This demonstrates that incorporation of Wurster’s Blue into the crown ether structure has no effect on the reduction potential [82].

Addition of $FeHDFB^+$ (Figure 3.1) to solutions containing **II** or **III** resulted in a positive shift in $E_{1/2}$. A representative voltammogram in acetonitrile is shown in Figure 3.3A. The observed positive shifts in reduction potential are in agreement with previously observed results studying redox active host-guest assemblies [74,75,82]. Cyclic voltammetric data were obtained in chloroform, as well as acetonitrile (Tables 3.1 and 3.2). No significant shift was observed when $FeHDFB^+$ was added to **I** (Figure 3.1). This strongly suggests that interactions between the cationic guest and the crown ether host cavities are responsible for the positive $E_{1/2}$ shifts observed and not effects due to interactions with the redox active N,N,N′,N′-tetraalkyl-1,4-phenylenediamine group. Similar positive shifts were observed when other cationic guests such as potassium, ammonium, and pentylamine were added to **II** or **III** [87].

All of the reduction potentials in chloroform showed a larger positive shift in reduction potential on combining **II** or **III** with $FeHDFB^+$, compared to the analogous acetonitrile experiments. The same overall trends were exhibited: a positive shift for compounds **II** and **III** in the presence of $FeHDFB^+$, with the larger shift observed for compound **II**.

Table 3.1 Electrochemical Data in Acetonitrile[≠]

Species	C [a] (mM)	$[M^+]$ [b] (mM)	$E_{1/2}$ [c] (V)	ΔE [d] (V)	ν [e] (V/s)	i_c / i_a [f]	D_c [g] (cm^2/s)	D_a [h] (cm^2/s)	K_R / K_O [i]
I	10.9	0.0	0.148	0.091	0.010	1.05	3.2×10^{-5}	2.8×10^{-5}	NA
II	3.7	0.0	0.150	0.060	0.010	0.82	3.6×10^{-6}	3.2×10^{-6}	NA
III	0.096	0.0	0.156	0.063	0.010	1.03	4.5×10^{-5}	4.0×10^{-5}	NA
I / $Fe(HDFB)^+$	0.61	1.3	0.158	0.108	0.010	1.04	7.0×10^{-6}	1.8×10^{-6}	NA
II / $Fe(HDFB)^+$	1.3	2.2	0.272	0.147	0.025	0.69	1.3×10^{-6}	6.4×10^{-7}	>120
III/ $Fe(HDFB)^+$	0.24	1.7	0.209	0.122	0.025	1.50	5.3×10^{-5}	3.7×10^{-6}	39

[≠] Table adapted from references [38] and [87].

[a] Concentration of the redox active host **I, II** or **III**.

[b] Concentration of the $FeHDFB^+$ guest

[c] Most positive value obtained by CV at the concentrations in columns 2 and 3 vs Ag/AgCl, in acetonitrile, and with 0.2 M Bu_4NPF_6.

[d] Peak-to-peak separation at the scan rate in column 6.

[e] Scan rate corresponding to the data in columns 4 & 5.

[f] Ratio of the cathodic current to the anodic current at the scan rate in column 6.

[g] Diffusion coefficient calculated from the cathodic peak currents.

[h] Diffusion coefficient calculated from the anodic peak currents.

[i] The binding enhancement as defined by Equation (3.1).

Table 3.2 Electrochemical Data in Chloroform[≠a]

Species	**C(mM)**	**[M$^+$] (mM)**	**$E_{1/2}$(V)^b**	**ΔE(V)**	**ν(V/s)**	**i_c / i_a**	**D_c(cm^2/s)**	**D_a(cm^2/s)**	**K_R / K_O**
I	5.1	0.0	0.253	0.253	0.010	1.04	4.4×10^{-6}	4.2×10^{-6}	NA
II	2.0	0.0	0.242	0.208	0.025	1.02	4.4×10^{-7}	7.9×10^{-7}	NA
III	2.6	0.0	0.283	0.407	0.025	1.06	1.9×10^{-5}	1.2×10^{-5}	NA
I / Fe(HDFB)$^+$	0.73	1.0	0.223	0.270	0.025	0.97	3.2×10^{-6}	2.1×10^{-6}	NA
II / Fe(HDFB)$^+$	0.077	1.15	0.790	0.200	0.300	0.64	NA	NA	1.9×10^{9}
III / Fe(HDFB)$^+$	0.10	1.15	0.720	0.219	0.075	0.97	5.7×10^{-5}	1.6×10^{-5}	2.5×10^{7}

[≠] Table adapted from references [38] and [87].

[a] Column headings are as defined in Table 1

[b] Versus Ag/AgCl, in cloroform, with 0.2 M Bu_4N

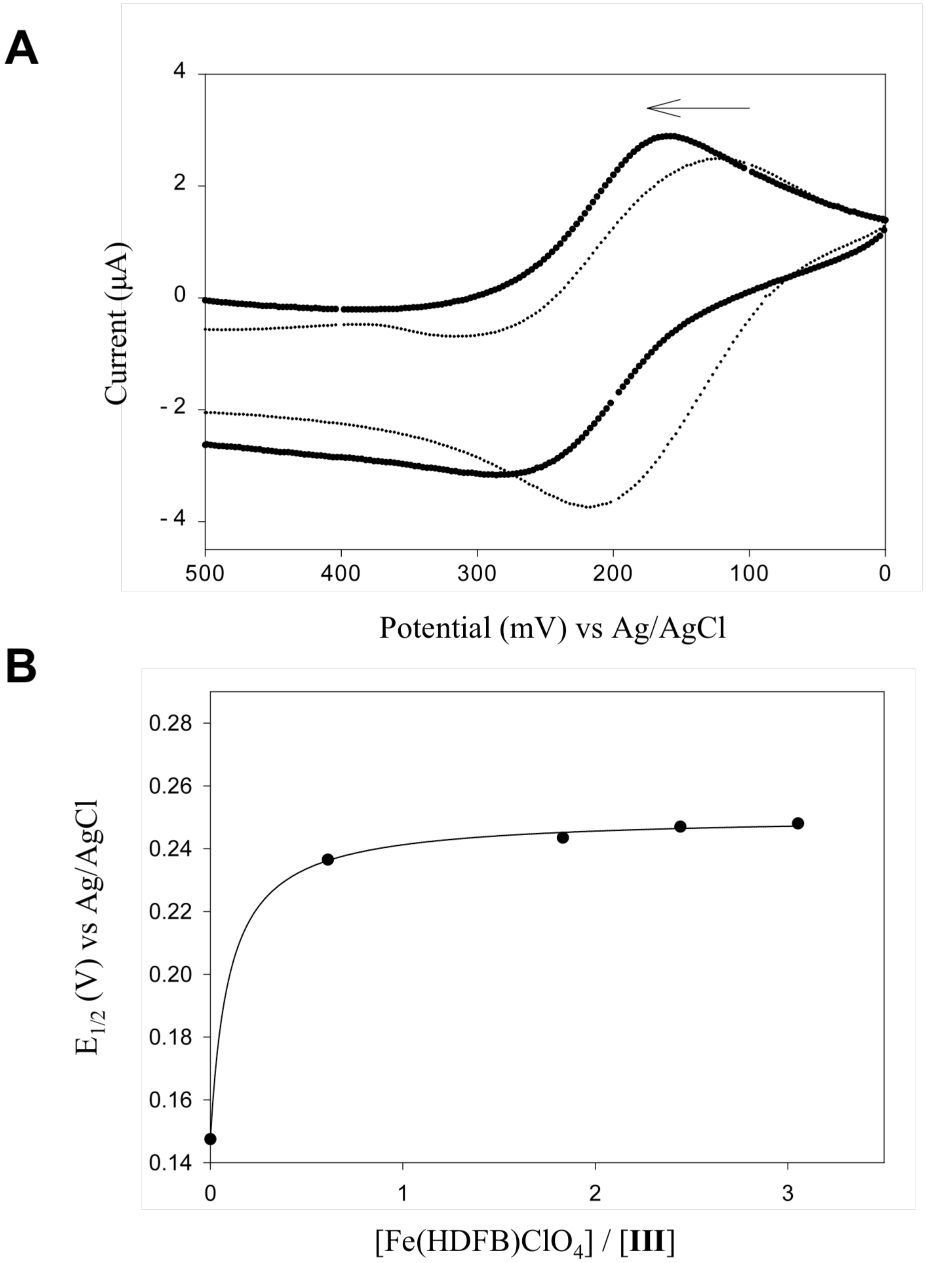

Figure 3.3 A. Representative cyclic voltammograms of III (•) and of III in the presence of Fe(HDFB)$^+$ (●). The cyclic voltammograms indicate the reversible first oxidation of III to form the radical cation III$^+$ and the return reduction to form the neutral parent III. The voltammograms shown in the figure begin with the oxidized Wurster crown and initially sweep in the direction of reduction. The arrow indicates the direction of shift in the cyclic voltammetric trace for III in the presence of FeHDFB$^+$. Conditions: Scan rate = 0.025 V s^{-1}, 0.2 M Bu_4NPF_6 in acetonitrile, 0.24 mM III, and 1.7 mM FeHFDB$^+$. B. Reduction potential ($E_{1/2}$) as a function of the FeHDFB$^+$ClO$_4^-$ to di aza crown ether (III) ratio. Conditions: Scan rate = 0.025 V s^{-1}, 0.2 M Bu_4NPF_6 in acetonitrile, 0.41 mM III, and 0 – 1.6 mM FeHDFB$^+$ClO$_4^-$. The solid line represents the mathematical fit of $E_{1/2}$ = 0.148 V + {a([FeHDFB$^+$ClO$_4^-$] / [III]) / {b + ([FeHDFB$^+$ClO$_4^-$] / [III])}} to the data where a = 0.1029(11) V and b = 0.098(14). Figure adapted from references [38] and [87].

3.2 Statement of Objectives

This chapter examines the interactions between Wurster's crowns **II** and **III** and a series of cationic guests. We propose that the redox shifts observed upon addition of a cationic guest to a solution containing a Wurster's crown (e.g. Figure 3.3A) are due to host-guest complex formation between the Wurster's crown and the cationic guest. Here we present studies that test this hypothesis using mass spectral and thermodynamic techniques. We discuss the mass spectral characterization of host-guest assemblies between the Wurster's crowns and cationic guests, including interactions of the *para*-Wurster's crown and a mono-substituted Wurster's crown with a siderophore guest, using ESI-MS and FAB-MS. We establish the limitations of these methods for redox active systems, as well as present the characterization of the proposed host-guest complexes using isothermal calorimetry (ITC). Finally, we discuss the significance and potential applications of these systems.

3.3 Experimental

3.3.1 Materials

Wurster's crowns **II** and **III** were synthesized as previously published and provided to us by the Sibert Group at the University of Texas, Dallas [80-82]. All referenced crown ethers, 18C6, B18C6, DB18C6, DC18C6 were purchased from Acros Organics and used without further purification. Methylamine ($CH_3NH_3^+$), and pentylamine ($CH_3(CH_2)_4NH_3^+$) were also purchased from Acros Organics and used without further purification. H_4DFB^+ was obtained from Sigma Aldrich. $FeHDFB^+$ was prepared as previously described [88], using acetonitrile or methanol as the solvent, depending on the experiment.

3.3.2 Methods

3.3.2.1 Electrospray Ionization Mass Spectrometry (ESI-MS)

Details of the ESI-MS process have been discussed in Chapter 2. For the experiments presented here, a series of samples was prepared containing an excess of guest (1 mM) with respect to the Wurster's crown host concentration (40 μM) in acetonitrile for systems of **II** and **III** with $CH_3NH_3^+$, $CH_3(CH_2)_4NH_3^+$, H_4DFB^+, and $FeHDFB^+$.

3.3.2.2 Fast Atom Bombardment Mass Spectrometry (FAB-MS)

FAB-MS is part of a family of desorption ionization techniques that can simultaneously volatilize and ionize condensed phase samples. In general, a sample is dissolved in a polar and relatively less volatile liquid matrix. Inert gas atoms (in our case Xe) are used to produce a beam of fast atoms. In an atom gun, the neutral gas atoms are first ionized by collisions with electrons. These ions are then accelerated, and subsequently neutralized by excess neutral gas atoms. Thus, fast ions are converted to fast atoms, Figure 3.4 [89].

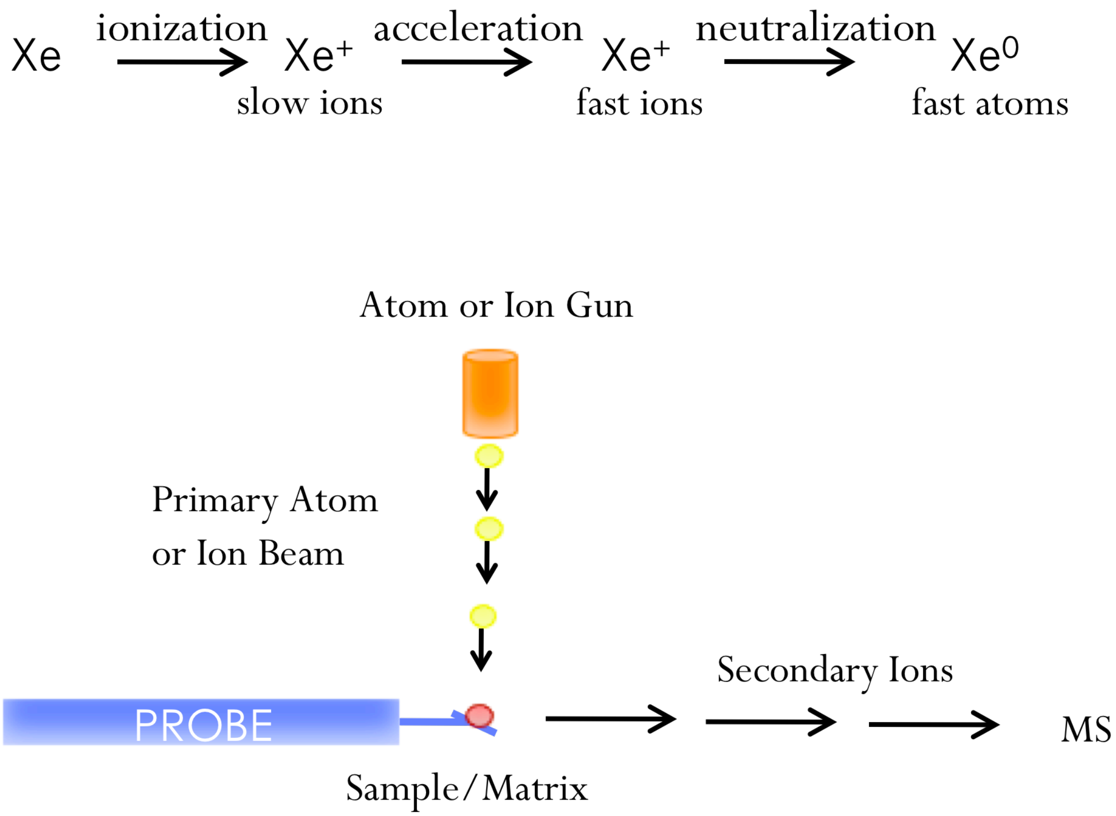

Figure 3.4 Illustration of the experimental process of Fast Atom Bombardment (FAB-MS). Adapted from Daas, C. ***Principles and Practice of Biological Mass Spectrometry;*** **Wiley: New York, 2001.**

All mass spectrometry experiments were performed using a JEOL JMS-SX102A mass spectrometer in positive ion mode with a high frequency magnet, using a gun voltage of 3 kV, an accelerating voltage of 10 kV and an emission current of 5 mA. Xenon gas was used as the primary source of ionization under a pressure of 10^{-5} Torr. 3-Nitrobenzylalcohol (3-NBA) was used as the matrix for all samples. Peaks corresponding to 3-NBA can be observed at 307, 460, 613, 766, and 919 m/z. The addition of the matrix to samples in the FAB-MS experiments reflects a change in starting point in comparison to the samples studied via ESI-MS, which contained no matrix. This change may be responsible for the difference in host-guest complex behavior observed between ESI-MS and FAB-MS and discussed in subsequent sections.

A series of samples was prepared containing an excess of FeHDFB$^+$ (1 mM) with respect to the Wurster's crown host concentration (40 μM) in acetonitrile or methanol, depending on the experiment.

3.3.2.2.1 Method Validation

In order to determine the validity of the FAB-MS method for host-guest complex formation, several cation–crown ether host–guest complexes, whose mass spectra were previously reported in the literature using ESI-MS [37], were studied using FAB-MS in acetonitrile. These include complexes formed between 18C6 and K$^+$, NH$_4^+$, CH$_3$(CH$_2$)$_4$NH$_3^+$, and FeHDFB$^+$ (Figures 3.5-3.8). These systems show intense host-guest complex peaks at 303, 282, 352, and 878 m/z, respectively.

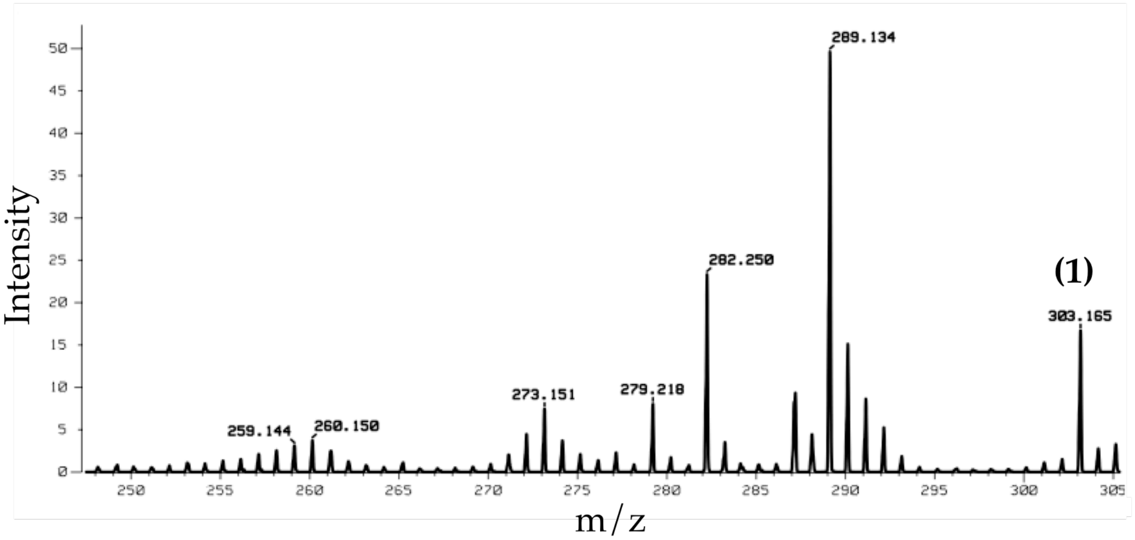

Figure 3.5 FAB mass spectrum of 18C6•K$^+$ host–guest system. (1) [18C6 + K]$^+$. Conditions: [18C6] = 4x10^{-4} M, [KCl] = 1x10^{-3} M, in acetonitrile, gun voltage = 3 kV, accelerating voltage = 10 kV, emission current = 5 mA, pressure = 10^{-5} Torr, Xe gas.

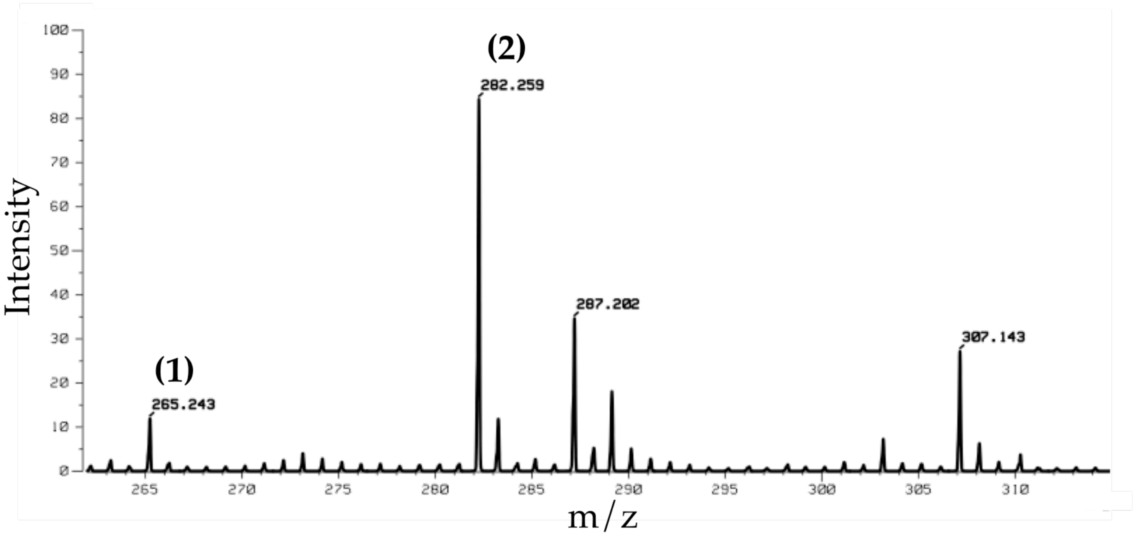

Figure 3.6 FAB mass spectrum of 18C6•NH_4^+ host–guest system. (1) [18C6 + H]$^+$, (2) [18C6 + NH_4]$^+$. Conditions: [18C6] = 4x10^{-4} M, [NH_4Cl] = 1x10^{-3} M, in acetonitrile, gun voltage = 3 kV, accelerating voltage = 10 kV, emission current = 5 mA, pressure = 10^{-5} Torr, Xe gas.

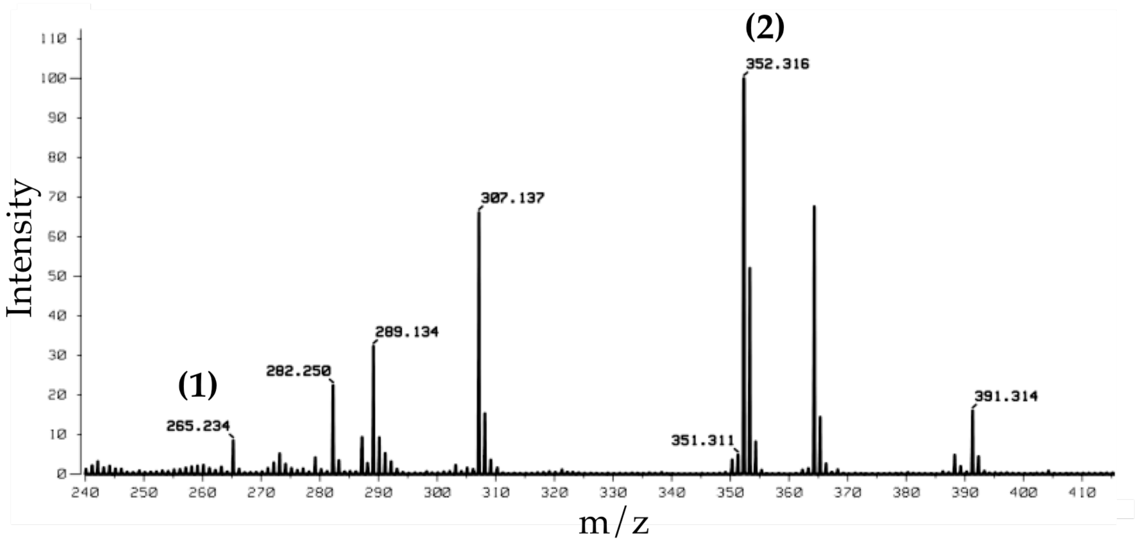

Figure 3.7 FAB mass spectrum of 18C6•$CH_3(CH_2)_4NH_3^+$ host–guest system. (1) [18C6 + H]$^+$, (2) [18C6 + $CH_3(CH_2)_4NH_3$]$^+$. Conditions: [18C6] = 4x10^{-4} M, [$CH_3(CH_2)_4NH_3$] = 1x10^{-3} M, in acetonitrile, gun voltage = 3 kV, accelerating voltage = 10 kV, emission current = 5 mA, pressure = 10^{-5} Torr, Xe gas.

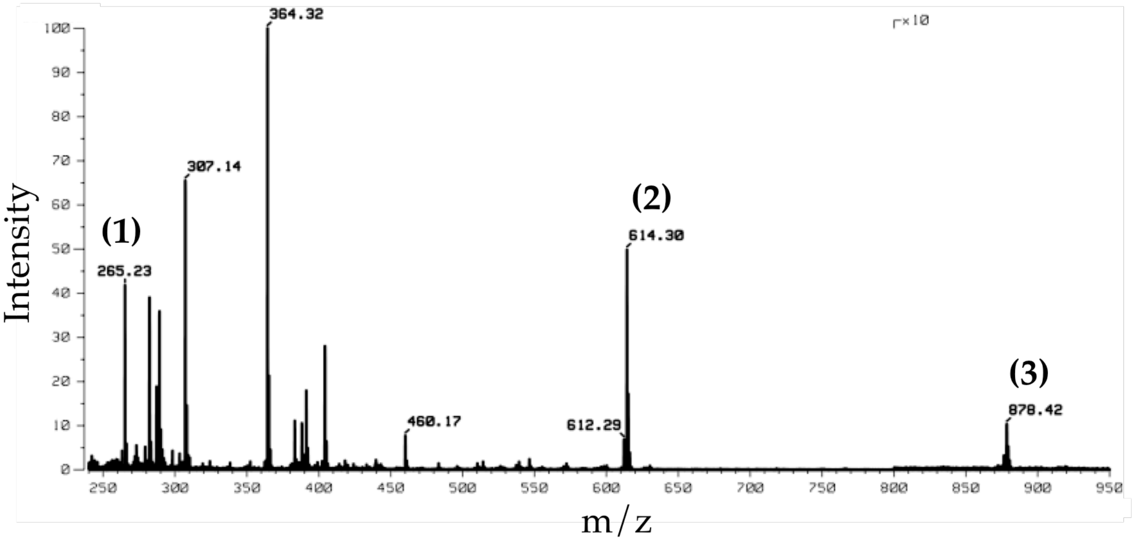

Figure 3.8 FAB mass spectrum of 18C6•FeHDFB$^+$ host–guest system. (1) [18C6 + H]$^+$, (2) FeHDFB$^+$, (3) [18C6 + FeHDFB]$^+$. Conditions: [18C6] = 4x10^{-4} M, [FeHDFB$^+$] = 1x10^{-3} M, in acetonitrile, gun voltage = 3 kV, accelerating voltage = 10 kV, emission current = 5 mA, pressure = 10^{-5} Torr, Xe gas.

The system involving 18C6 and $CH_3NH_3^+$ was also studied in acetonitrile, but no host-guest complex peak was observed using FAB-MS. This is important to note, as the same behavior was observed for systems involving **II**, **III**, and $CH_3NH_3^+$. The presence of intense host-guest complex peaks observed for most of the systems studied indicates that FAB-MS is a promising technique by which to monitor host-guest complex formation.

3.3.2.3 Isothermal Calorimetry

We can directly obtain the stoichiometry of the interaction, the binding affinity, and the enthalpy through the use of an isothermal titration calorimeter (ITC), Figure 3.9. The ITC is equipped with a stirring syringe filled with the macromolecule of interest that can be inserted into the sample cell of the instrument. The sample cell contains the ligand of interest, in this case methylamine, pentylamine, H_4DFB^+, or FeHDFB$^+$. A reference cell is filled with the buffer or solvent used in both the syringe and sample cells. The reference cell and sample cell are held at the same temperature through the constant application of a low amount of power.

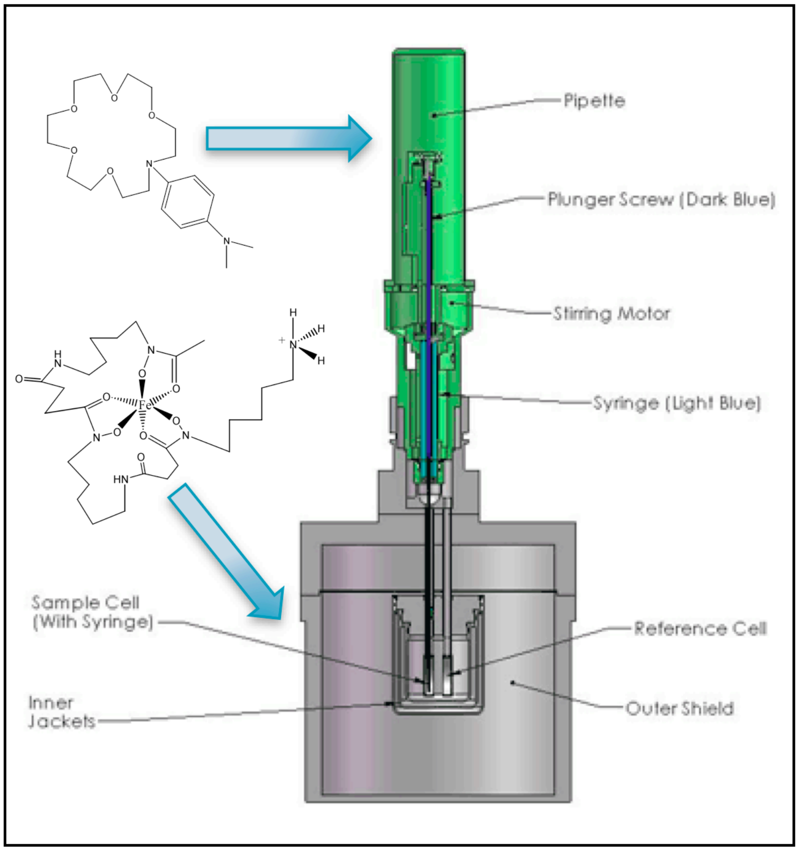

Figure 3.9 Diagram of an isothermal calorimeter. For our experiments, the host was loaded into the syringe and the guest was placed in the sample cell in acetonitrile or methanol, depending on the experiment. Wurster's crown II and FeHDFB$^+$ are shown above as the host and guest, respectively. Adapted from www.microcal.com.

Upon injection of the macromolecule into the ligand solution, heat is either evolved or absorbed, and the ITC compensates by either adding or removing heat from the sample cell until it is again at the same temperature as the reference cell. The measured change in power is plotted against time to give the plot such as shown in Figure 3.10A. The individual injections can then be integrated to give a plot of enthalpy per mole of injectant versus the molar ratio of macromolecule to ligand, Figure 3.10B.

The data are fit to a one-site binding model, from which enthalpy (ΔH), stoichiometry (n), and binding constant (K_a) can be obtained.

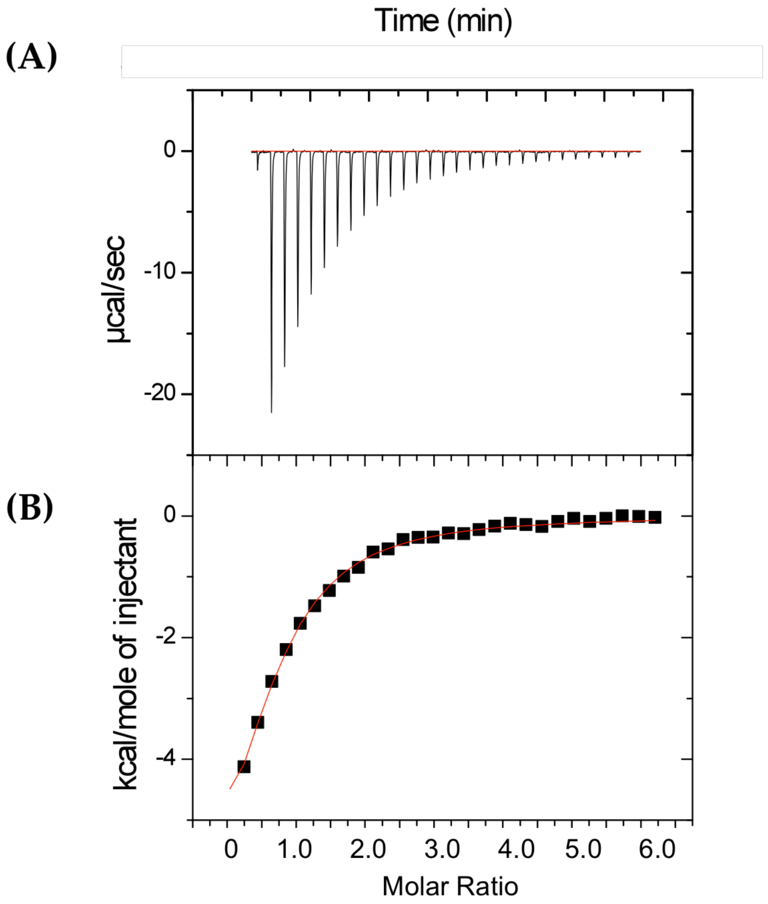

Figure 3.10 Sample data for a microcalorimetry titration. (A) Heat evolved per time during each injection. The area under each peak is calculated, yielding (B) the heat evolved per injection in kcal/mol as a function of molar ratio of macromolecule to ligand. Adapted from www.microcal.com.

It is important to obtain a binding isotherm that provides the maximum data points for analysis, as the shape of the binding curve dictates how accurately the binding constant can be determined. This shape is dependent on the binding constant as well as on the concentration of the component in the calorimeter cell. The product of these two terms gives a number referred to as the C value, where $C = n \times K_a \times$ [component in sample cell] and *n* is the stoichiometry of the interaction [90]. An appropriate C value should ideally be between 10 and 100, Figure 3.11. Under the concentrations adopted for ITC experiments, data sets with low *C* values are not sigmoidal, meaning that the complex formed changes little from injection to injection. Isotherms with very high *C* values suffer from too angular sigmoidal shapes. Here, all of the ligand binds to form complex in early injections and, once a saturation point is reached, the final injections show no net heat. Both instances make the determination of free versus bound ligand concentrations inaccurate [90].

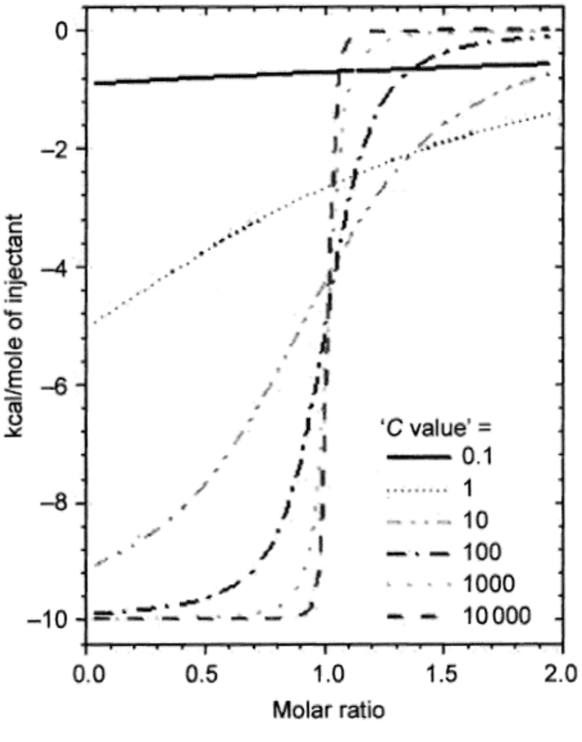

Figure 3.11 Plot of the effects of different C values on the binding isotherm. Adapted from Thomson, J. A.; Ladbury, J. E. In *Biocalorimetry 2: Applications of Calorimetry in the Biological Sciences*; Ladbury, J. E., Doyle, M. L., Eds.; Wiley: New Jersey, 2004.

Although *C* values between 10 and 100 are ideal, binding studies with low *C* values have been reported [91,92]. Based on the concentrations used in our experiments, *C* values between 10 and 100 were not always possible, and so *C* values between 1 and

10 were used in these cases. These were estimated based on binding constants for similar systems, since the binding constants for the systems of interest are not known.

An isothermal VP-ITC titration calorimeter from MicroCal, Inc. (Northampton, MA) was used for the titration experiments. The volume of the sample cell was 1.4346 mL. The calorimeter was calibrated using electrical pulses. All samples were degassed before loading the calorimeter cells and syringe. All experiments were carried out at 25 °C. In a typical calorimetry experiment, 2 mL of a methanol solution of guest (methylamine, pentylamine, or H_4DFB^+) were placed in the calorimeter. This solution was titrated with host in 60-100 injections of 2.0-2.5 μL each, depending on the experiment. During the titration, the stir rate was 310 rpm. The compensating power required to maintain thermal equilibrium between the sample and reference cells was recorded as a function of time and integrated to yield a plot of enthalpy per injection as a function of molar ratio. The heat evolved during each injection is a function of the enthalpy of binding ΔH and the amount of complex formed during that injection. This latter quantity is a function of the concentration of guest, host, complex and the host-guest association constant, K_a. A nonlinear least-squares fit of the appropriate equation relating these values to the data provides estimates of ΔH, K_a, and the stoichiometry of binding n. Origin software was used to construct all plots.

3.3.2.3.1 ITC Method Validation

In order to determine the accuracy and precision of our experimental method, the association constants of a cationic metal-ligand assembly and several cation–crown ether host–guest complexes, whose association constants were previously reported in the literature using different experimental methods, were compared with association constants derived using our method.

The binding between Ca^{2+} and EDTA was studied in MES buffer, as this system has been previously well characterized in the literature [93]. Concentrations were chosen so as to obtain a *C* value of 1044. The thermogram, corresponding to an exothermic process (Figure 3.12A), was then integrated to obtain the binding isotherm (Figure 3.12B). From the curve fit of this isotherm (obtained using Origin software), the following parameters were determined: the association constant, $K_a = 2.0 \times 10^6\ M^{-1}$, the enthalpy, $\Delta H = -3.7$ kcal/mol, and the stoichiometry, $n = 1.0$. These correlate nicely with literature data in MES buffer, where the association constant was $K_a = 2.0 \times 10^6\ M^{-1}$, the enthalpy was $\Delta H = -4.1$ kcal/mol, and the stoichiometry was $n = 1.0$ [93]. This correlation validates our ITC method for obtaining thermodynamic parameters between hosts and guests.

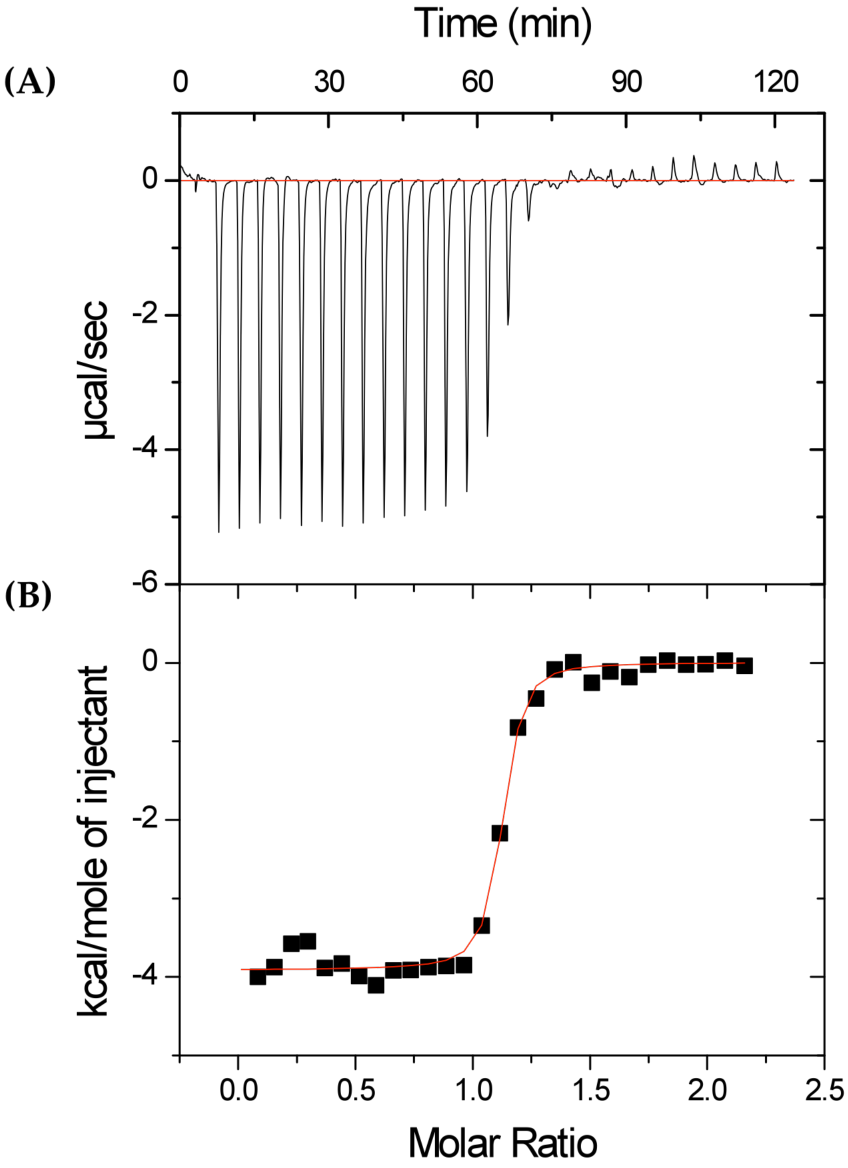

Figure 3.12 Thermogram (A) and binding isotherm (B) showing the addition of Ca^{2+} into EDTA in MES buffer at pH 6. Conditions: [$CaCl_2$] = 5 mM in syringe, [EDTA] = 0.5 mM in sample cell, MES buffer in reference cell, T = 25 °C. From the curve fit (using Origin software), the following parameters have been determined: the association constant, K_a = (2.09 ± 0.82)× 10^6 M^{-1}, the enthalpy, Δ*H* = -3.70 ± 0.05 kcal/mol, and the stoichiometry, *n* = 1.09 ± 0.01.

The binding between 18C6 and protonated methylamine and pentylamine, H_4DFB^+, and $FeHDFB^+$ was also studied in MeOH (Figures 3.13-3.16, Table 3.3). These systems have been well characterized and offer a good comparison to those of **II** and **III**, due to the interaction between a cationic guest and a crown-type cavity.

Injecting 18C6 into methylamine or pentylamine resulted in thermograms displaying saturation behavior (C values of 9 and 10, respectively). The thermograms were integrated and binding isotherms were obtained whose fit to a single site binding model gave a stoichiometry of $n = 0.3$, Figures 3.13-3.14. This is unexpected, as it would indicate a conformation where three protonated amine guests bind to every crown cavity. It is possible that this behavior is observed as an intermediate to the final 1:1 configuration. The association constants obtained from these data in MeOH are shown in Table 3.3. These data do not correlate with literature data obtained in MeOH using ESI-MS (Table 3.3 and Chapter 2). However, the association constant values are strongly influenced by the stoichiometry, which in this case may not reflect the final configuration of the host-guest complex, and may explain the deviation from the literature values. The fact that we are still able to observe binding between these systems is promising and deserves further studies.

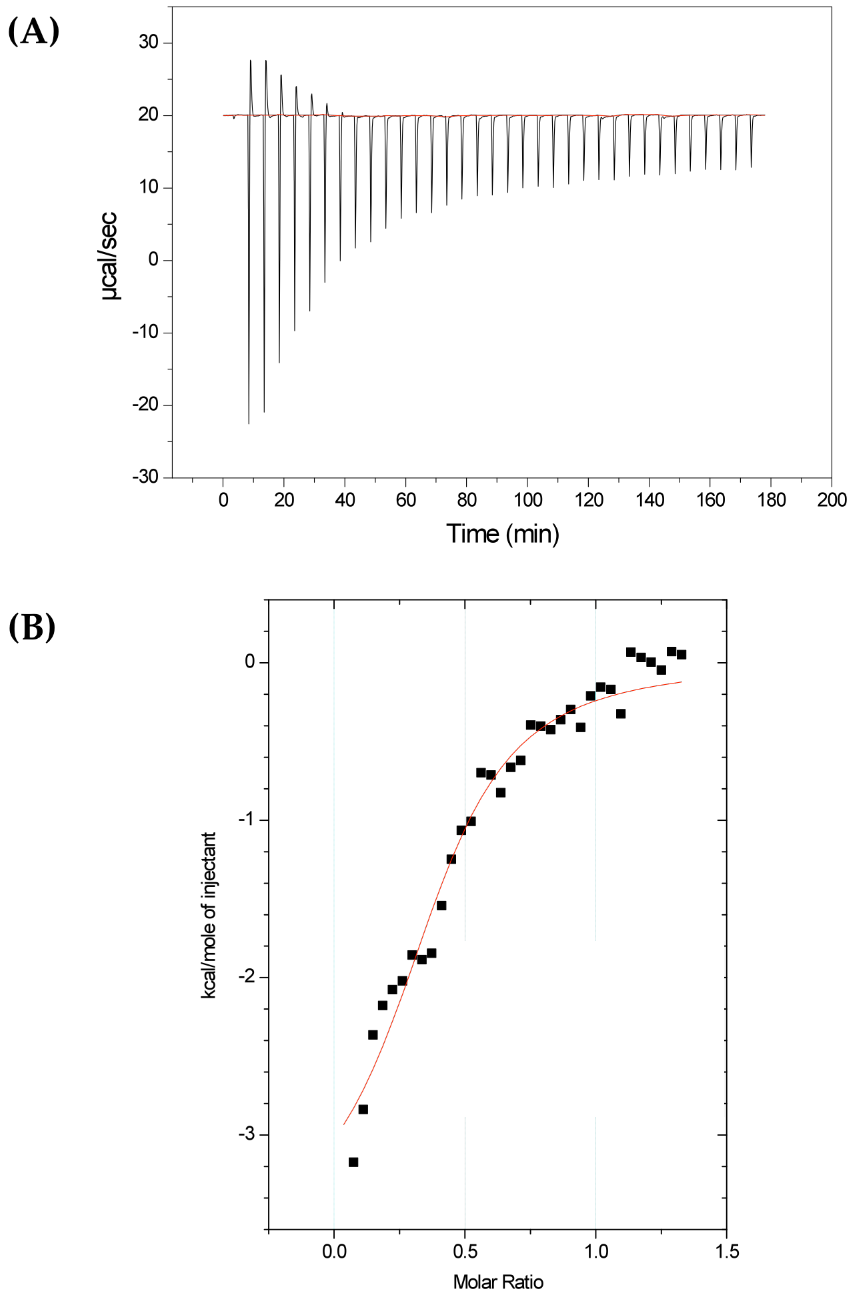

Figure 3.13 Thermogram (A) and binding isotherm (B) showing the addition of 18C6 into $CH_3NH_3^+$ in MeOH. Conditions: [18C6] = 65 mM in syringe, $[CH_3NH_3^+]$ = 2.5 mM in sample cell, MeOH in reference cell, T = 25 °C. From the curve fit (using Origin software), the following parameters have been determined: the association constant, K_a = $(3.89 \pm 0.81)\times 10^3$ M^{-1}, the enthalpy, ΔH = -3.83 ± 0.33 kcal/mol, and the stoichiometry, n = 0.39 ± 0.03.

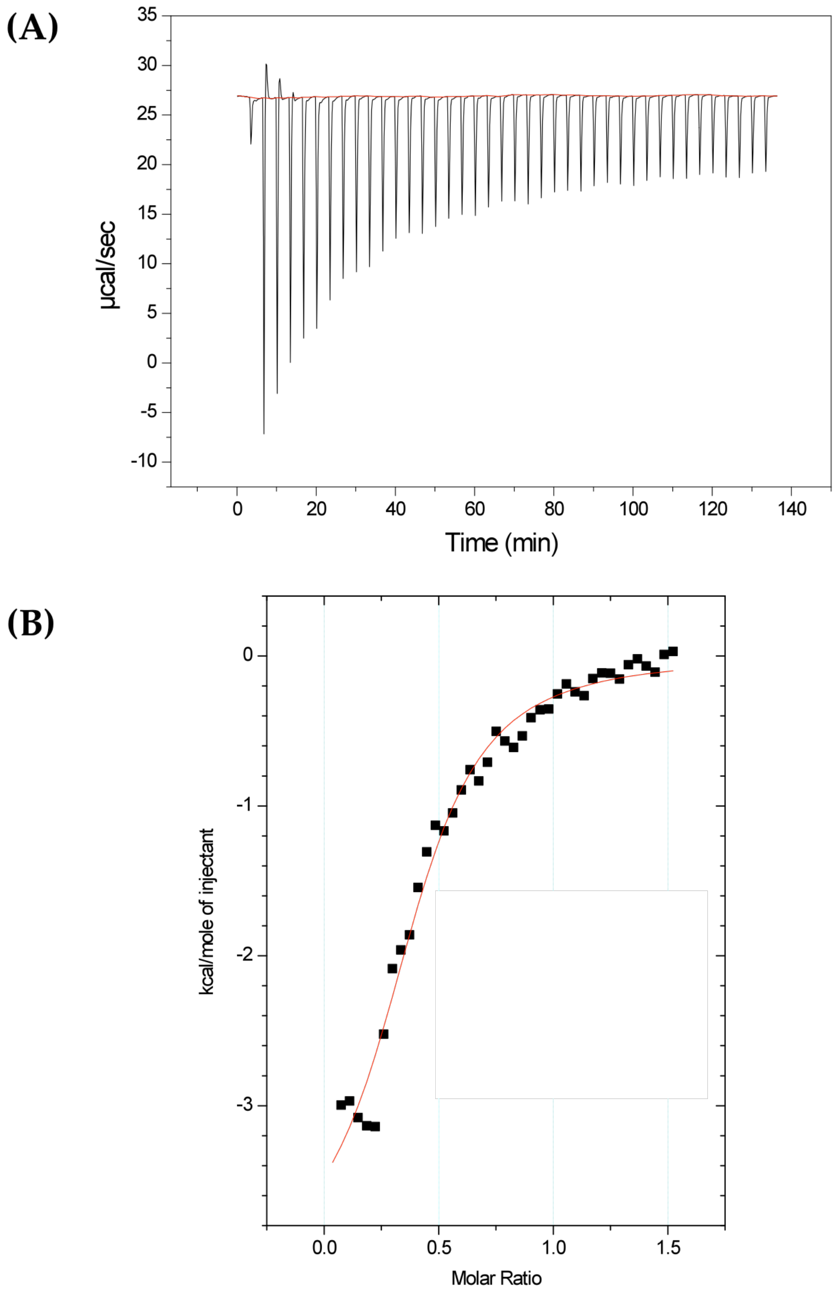

Figure 3.14 Thermogram (A) and binding isotherm (B) showing the addition of 18C6 into $CH_3(CH_2)_4NH_3^+$ in MeOH. Conditions: [18C6] = 65 mM in syringe, $[CH_3(CH_2)_4NH_3^+]$ = 2.5 mM in sample cell, MeOH in reference cell, T = 25 °C. From the curve fit (using Origin software), the following parameters have been determined: the association constant, $K_a = (3.75 \pm 0.56) \times 10^3\ M^{-1}$, the enthalpy, $\Delta H = -5.37 \pm 0.66$ kcal/mol, and the stoichiometry, $n = 0.32 \pm 0.03$.

Injecting 18C6 into H_4DFB^+ or $FeHDFB^+$ in MeOH resulted in thermograms displaying sigmoidal behavior (C values of 53 and 75, respectively). The thermograms were integrated and binding isotherms were obtained whose fit to a single site binding model gave a stoichiometry of n~1.0, Figures 3.15-3.16. This behavior is expected and indicates a conformation where one guest binds to every crown ether host.

Both binding isotherms show a sharp decrease in enthalpy per mole of injectant between the molar ratios of 0.5 and 1.0 for H_4DFB^+ (Figure 3.15B) and between 1.0 and 1.5 for $FeHDFB^+$ (Figure 3.16B). This sharp decrease could indicate that more than one process is occurring during the measurement and culminates between the molar ratios indicated. The cause of the decrease in these two cases in unknown. In general, this behavior could occur due to a deprotonation step, or solvent interactions due to a difference in solvent composition between the syringe and the cell, if, for example, some water remained in the cell from a previous washing step. The sharp decrease in enthalpy per mole of injectant results in a different than ideal fit to the binding isotherm, in turn affecting the stoichiometry value and the association constant calculated from the data. The association constants obtained from these data in MeOH are shown in Table 3.3, along with literature values for these systems obtained using ESI-MS. Although the values obtained using ITC are in the same range as the literature data obtained using ESI-MS, they are not within error. This is easily explained based on the fit of the binding isotherm.

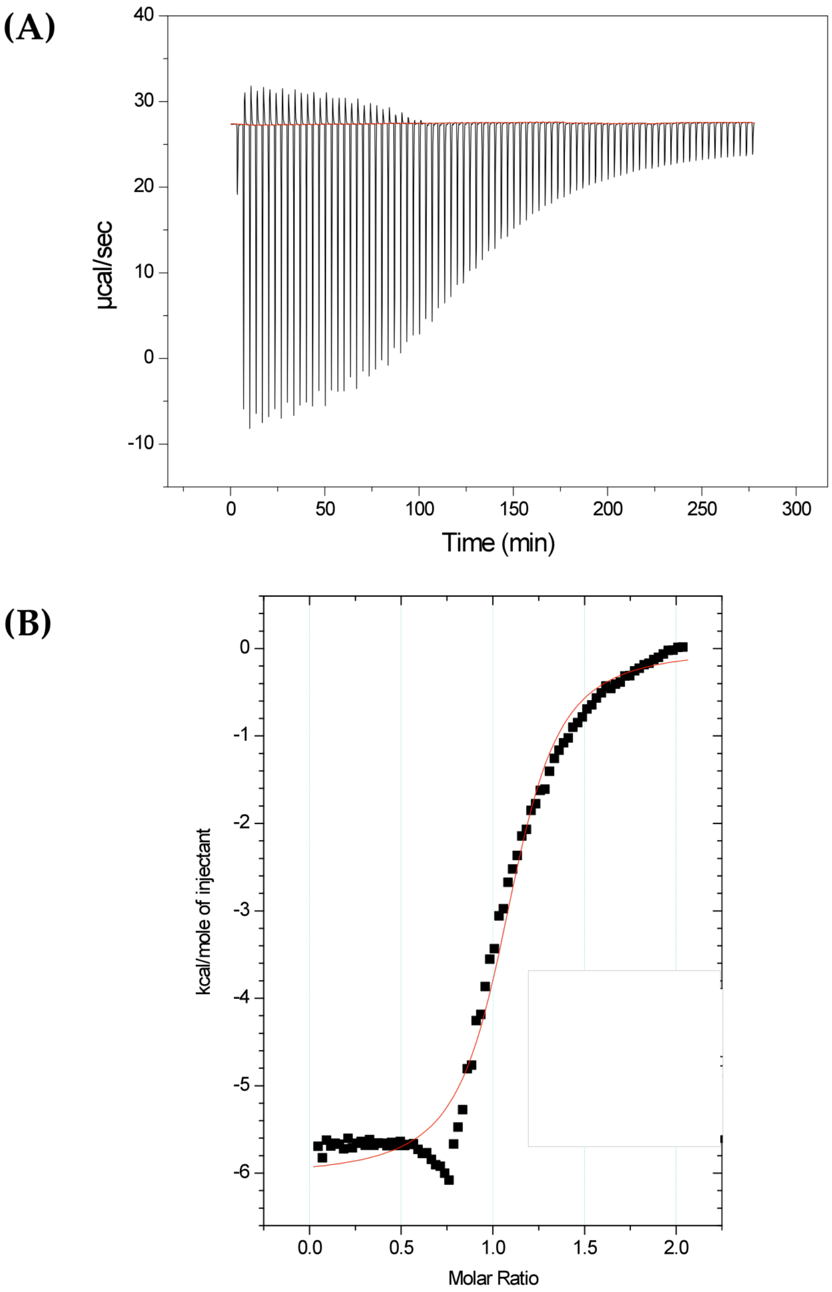

Figure 3.15 Thermogram (A) and binding isotherm (B) showing the addition of 18C6 into H_4DFB^+ in MeOH. Conditions: [18C6] = 65 mM in syringe, [H_4DFB^+] = 2.5 mM in sample cell, MeOH in reference cell, T = 25 °C. From the curve fit (using Origin software), the following parameters have been determined: the association constant, $K_a = (2.12 \pm 0.22)\times 10^4\ M^{-1}$, the enthalpy, $\Delta H = -6.03 \pm 0.06$ kcal/mol, and the stoichiometry, $n = 1.07 \pm 0.01$.

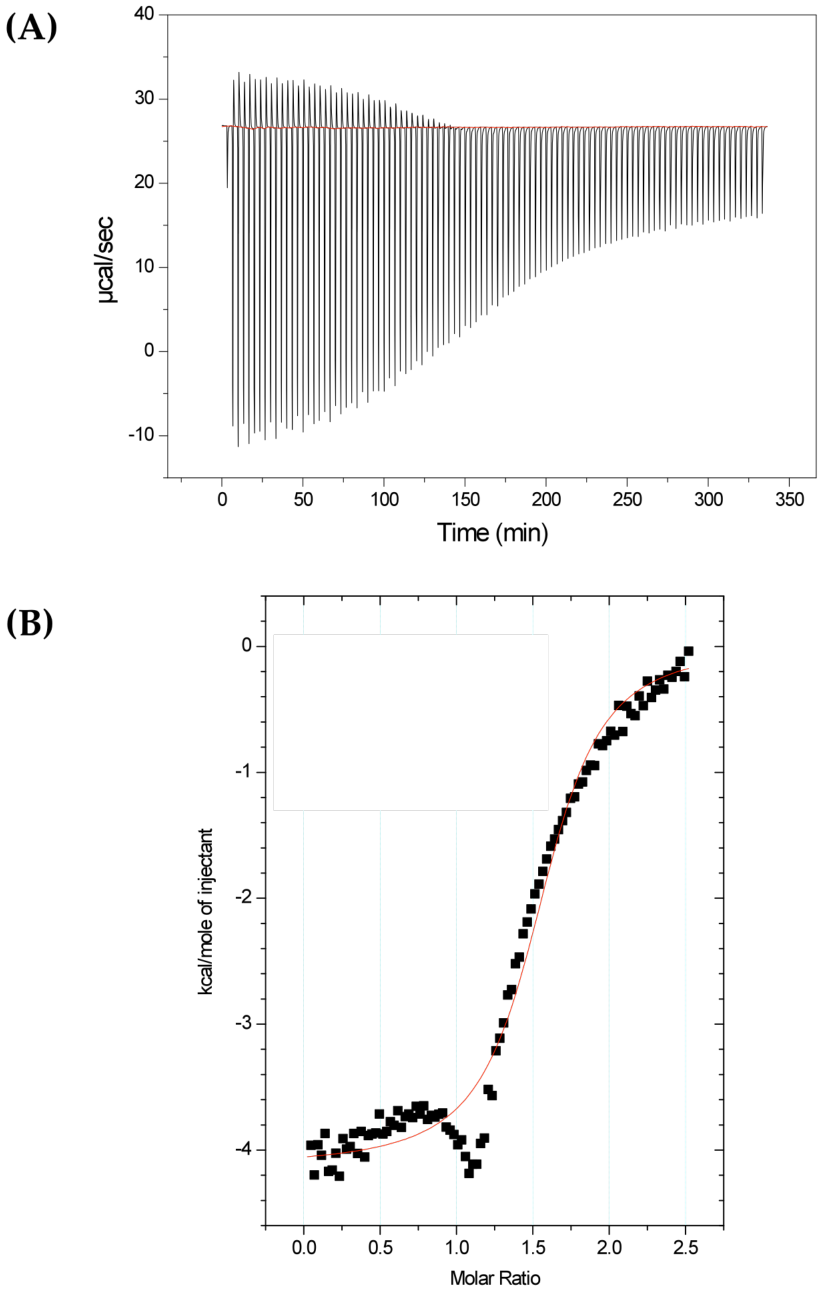

Figure 3.16 Thermogram (A) and binding isotherm (B) showing the addition of 18C6 into FeHDFB$^+$ in MeOH. Conditions: [18C6] = 32.5 mM in syringe, [FeHDFB$^+$] = 2.5 mM in sample cell, MeOH in reference cell, T = 25 °C. From the curve fit (using Origin software), the following parameters have been determined: the association constant, $K_a = (3.01 \pm 0.41) \times 10^4\ M^{-1}$, the enthalpy, $\Delta H = -4.15 \pm 0.04$ kcal/mol, and the stoichiometry, $n = 1.32 \pm 0.01$.

Table 3.3 Thermodynamic Parameters of Cation Binding to 18C6 in MeOH using ITC[a]

Cationic Guest	[Guest] (mM)	[Host] (mM)	n	ΔH (kcal/mol)	log K_a	log $K_{a\ \mathrm{literature}}$[b]
$CH_3NH_3^+$	2.5	65	0.39 ± 0.03	-3.83 ± 0.33	3.59 ± 0.09	4.49 ± 0.03
$CH_3(CH_2)_4NH_3^+$	2.5	65	0.32 ± 0.03	-5.37 ± 0.66	3.57 ± 0.07	5.21 ± 0.03
H_4DFB^+	2.5	65	1.07 ± 0.1	-6.03 ± 0.06	4.32 ± 0.05	4.07 ± 0.05
$FeHDFB^+$	2.5	32.5	1.32 ± 0.01	-4.15 ± 0.04	4.49 ± 0.06	3.70 ± 0.07

[a] Data obtained from ITC measurements, Figures 3.13-3.16.

[b] Data obtained by ESI-MS in MeOH. See Chapter 2 and Reference[37].

Using ITC we successfully validated the method for a well-studied system, that of Ca^{2+} and EDTA in MES at pH 6. The association constants that we obtained correlate well with those in the literature [93]. In addition, we conducted preliminary studies using systems similar to that of the Wurster's crowns to be studied later, specifically 18C6 and protonated methylamine and pentylamine, H_4DFB^+ and $FeHDFB^+$ in MeOH. These ITC data show promising results in that we can observe binding between host and guest. Although the association values obtained do not always correlate with literature values, they offer a good starting point form which to conduct further experiments.

3.4 Results

3.4.1 Mass Spectral Evidence of Host-Guest Complex Formation Via ESI-MS

From the work of Wirgau [38,87], as discussed in the Introduction, a shift in $E_{1/2}$ is observed in the voltammogram of a Wurster's crown upon addition of a cationic guest. Our working hypothesis is that this electrochemical behavior is due to host-guest complex formation. It is further hypothesized that this occurs through H-bond interaction of the protonated amine with the aza crown cavity (Figure 3.1), as shown previously for complexes between 18C6, a structurally similar crown ether, and cationic guests [94]. In an attempt to obtain mass spectral evidence of host-guest complex formation for complexes involving aza-crowns **II** and **III** and to understand the nature of the observed electrochemical shift, host-guest assemblies with K^+, NH_4^+, $CH_3NH_3^+$, and $CH_3(CH_2)_4NH_3^+$ in acetonitrile were studied using ESI-MS. Our goal was to use the previously developed method for obtaining association constants using ESI-MS (Chapter 2) to obtain the association constants for these Wurster's crown systems.

Although all ESI-MS spectra of presumed complexes between **II** and cationic guests show a peak at 383 m/z corresponding to **II**, showing that the host is ionizable and can be viewed through MS, evidence of host-guest complex formation was obtained only with $CH_3(CH_2)_4NH_3^+$, with a host-guest complex peak observable at 470 m/z (Figure 3.17). The presumed assembly involving **II** with $FeHDFB^+$ was also studied, with no observable host-guest complex formation, although both host and guest were observed with peaks at 383 and 614 m/z, respectively (Figure 3.18). Although ionization chamber temperature, flow rate, nebulizer pressure, and dry gas flow rate were varied to optimize host-guest complex formation, none was observed.

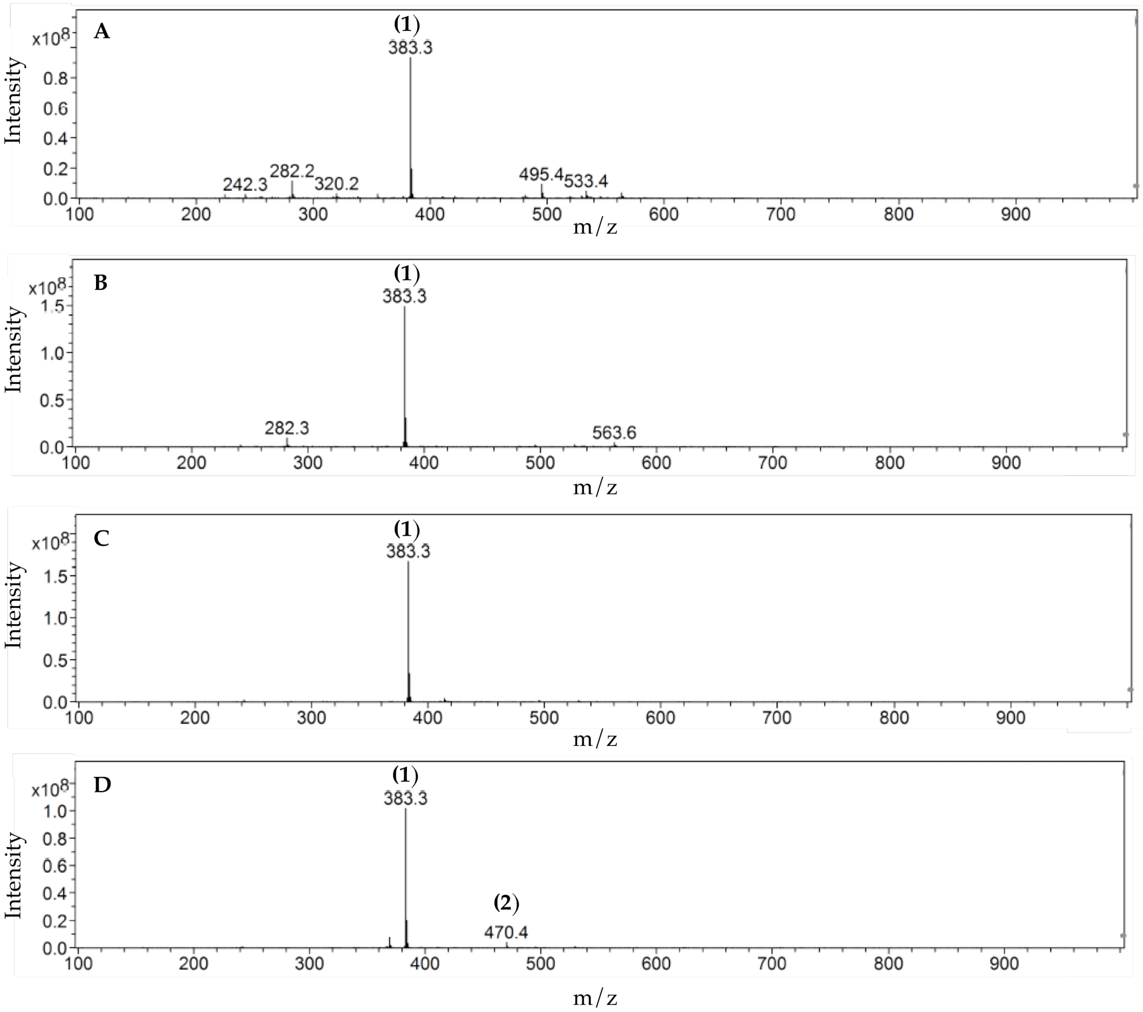

Figure 3.17 ESI mass spectrum of II•cation host–guest systems. A. II•K^+ host-guest system: (1) $[II + H]^+$. B. II•NH_4^+ host–guest system: (1) $[II + H]^+$. C. II•$CH_3NH_3^+$ host–guest system: (1) $[II + H]^+$. D. II•$CH_3(CH_2)_4NH_3^+$ host-guest system: (1) $[II + H]^+$, (2) $[II + CH_3(CH_2)_4NH_3^+]$. Conditions: [II] = $4x10^{-5}$ M, [cation guest] = $1x10^{-3}$ M, in acetonitrile, T = 125 °C, Nebulizer = 20 psi, Dry Gas = 7 L/min.

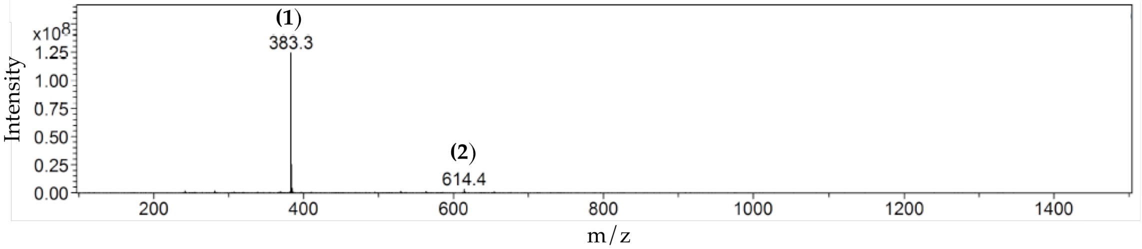

Figure 3.18 ESI mass spectrum of II•$FeHDFB^+$ host–guest system. (1) $[II + H]^+$, (2) $FeHDFB^+$. Conditions: [II] = $4x10^{-5}$ M, [$FeHDFB^+$] = $1x10^{-3}$ M, in acetonitrile, T = 125 °C, Nebulizer = 20 psi, Dry Gas = 7 L/min.

Assemblies involving **III** with K^+, NH_4^+, $CH_3NH_3^+$, and $CH_3(CH_2)_4NH_3^+$ were also studied in acetonitrile using ESI-MS. Evidence of host-guest complex formation was only observed for K^+ and $CH_3(CH_2)_4NH_3^+$, in which host-guest complex peaks were observable at 539 and 588 m/z, respectively (Figure 3.19). As with **II**, the peak corresponding to the host was observable in all spectra (501 m/z).

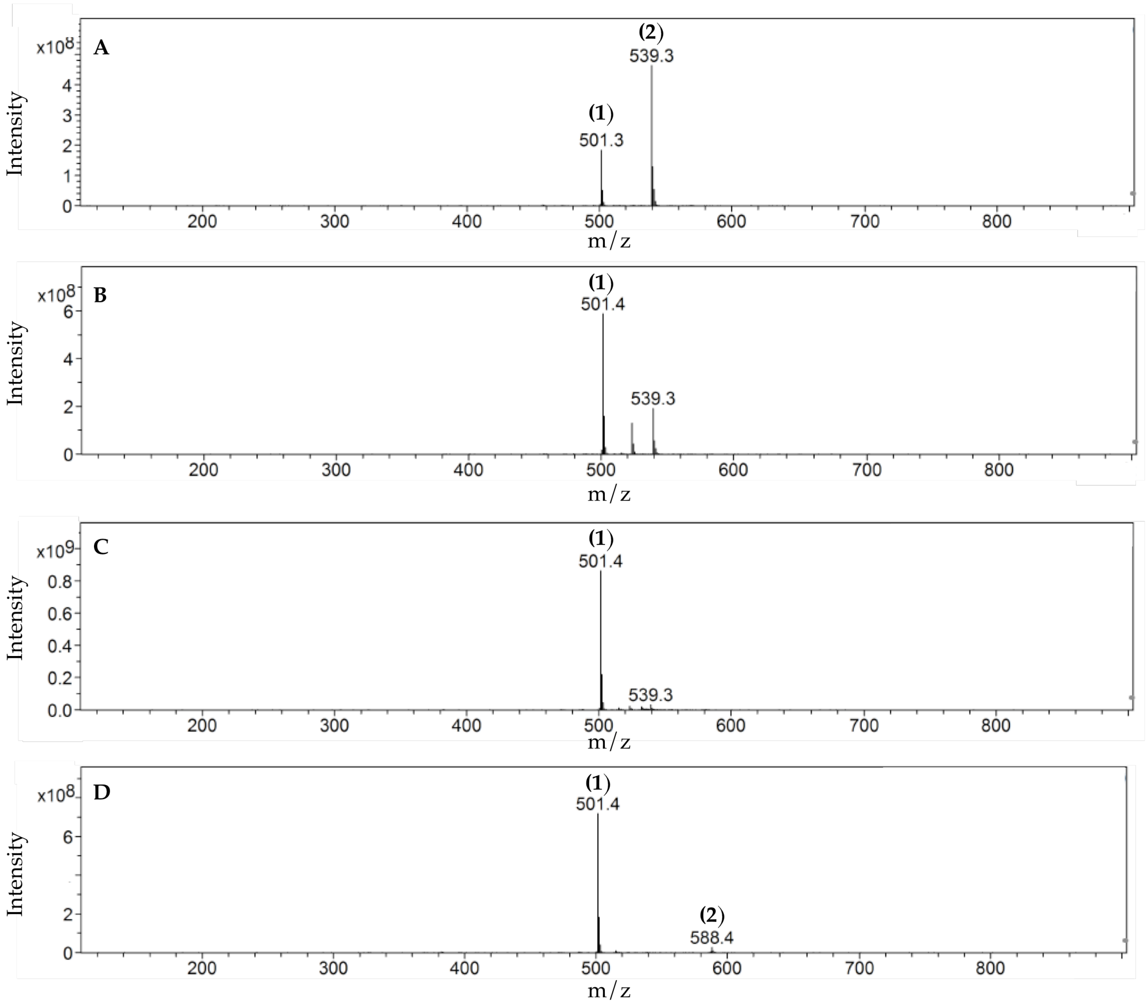

Figure 3.19 ESI mass spectrum of III•small cation host–guest systems. A. III•K^+ host-guest system: (1) [III + H]$^+$, (2) [III + K]$^+$ B. III•NH_4^+ host–guest system: (1) [III + H]$^+$. C. III•$CH_3NH_3^+$ host–guest system: (1) [III + H]$^+$. D. III•$CH_3(CH_2)_4NH_3^+$ host-guest system: (1) [III + H]$^+$, (2) [III + $CH_3(CH_2)_4NH_3^+$]. Conditions: [III] = $4x10^{-5}$ M, [cation guest] = $1x10^{-3}$ M, in acetonitrile, T = 125 °C, Nebulizer = 20 psi, Dry Gas = 7 L/min.

Formation of a host-guest complex was observed in the case of **III** and FeHDFB$^+$ in acetonitrile. Peaks were observed for **III** at 501 m/z, FeHDFB$^+$ at 614 m/z, and the **III**•FeHDFB$^+$ host-guest complex at 1114 m/z (Figure 3.20).

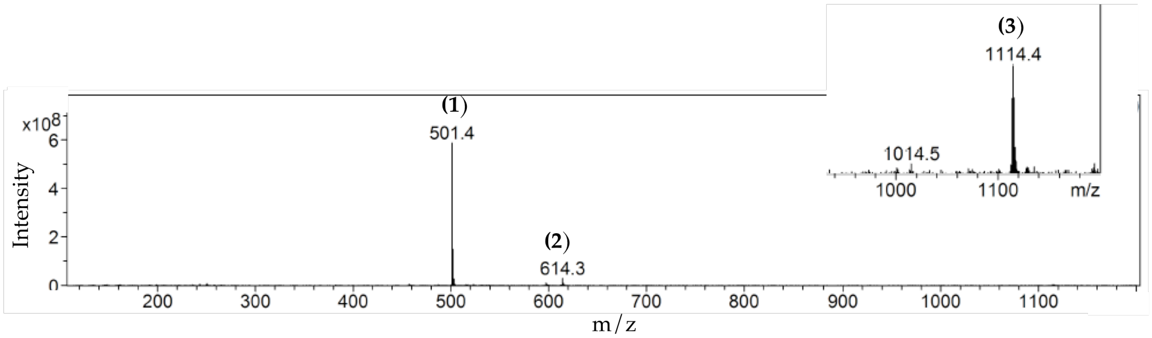

Figure 3.20 ESI mass spectrum of III•FeHDFB$^+$ host–guest system. (1) [III + H]$^+$, (2) FeHDFB$^+$, (3) [III + FeHDFB]$^+$. Conditions: [III] = 4x10^{-5} M, [FeHDFB$^+$] = 1x10^{-3} M, in acetonitrile, T = 125 °C, Nebulizer = 20 psi, Dry Gas = 7 L/min.

The reasons for the lack of ability to detect host-guest complex formation in the case of complexes between **II** and K$^+$, NH_4^+, $CH_3NH_3^+$ and FeHDFB$^+$ and between **III** and NH_4^+, and $CH_3NH_3^+$ in acetonitrile are not clear and are unexpected based on previous findings with structurally similar crown ether hosts such as 18C6 and the above guests, for which host-guest complex formation was detectable (see Chapter 2). Although there is no literature precedent, we hypothesize that the redox nature of the host affects the detection of host-guest formation in the instrument. Oxidation may take place within the instrument due to the large positive potential (3.7 kV) applied to the needle in order to charge the droplets. Oxidation of the host within the system would result in a positive charge that would make binding of the guests to the cavity less favorable [72]. Weaker binding may not be detected by the instrument, which would explain why in most instances no host-guest assemblies were observed.

3.4.2 Mass Spectral Evidence of Host-Guest Complex Formation Via FAB-MS

Due to the lack of evidence for host-guest complex formation using ESI-MS, we turned to FAB-MS as an alternate technique. FAB-MS offers a different form of ionization without the direct application of a potential, while still enabling us to monitor host-guest complex intensity as a function of concentration of host, from which we could construct saturation plots and obtain association constants, as with the ESI-MS method.

Assemblies between **II** and K^+, NH_4^+ and $CH_3(CH_2)_4NH_3^+$ were studied using FAB-MS in acetonitrile, Figure 3.21. Host-guest complex formation was observed in all cases for these three guests. No host-guest complex formation was observed between $CH_3NH_3^+$ and **II** (Figure 3.22), as was the case with ESI-MS (Figure 3.17).

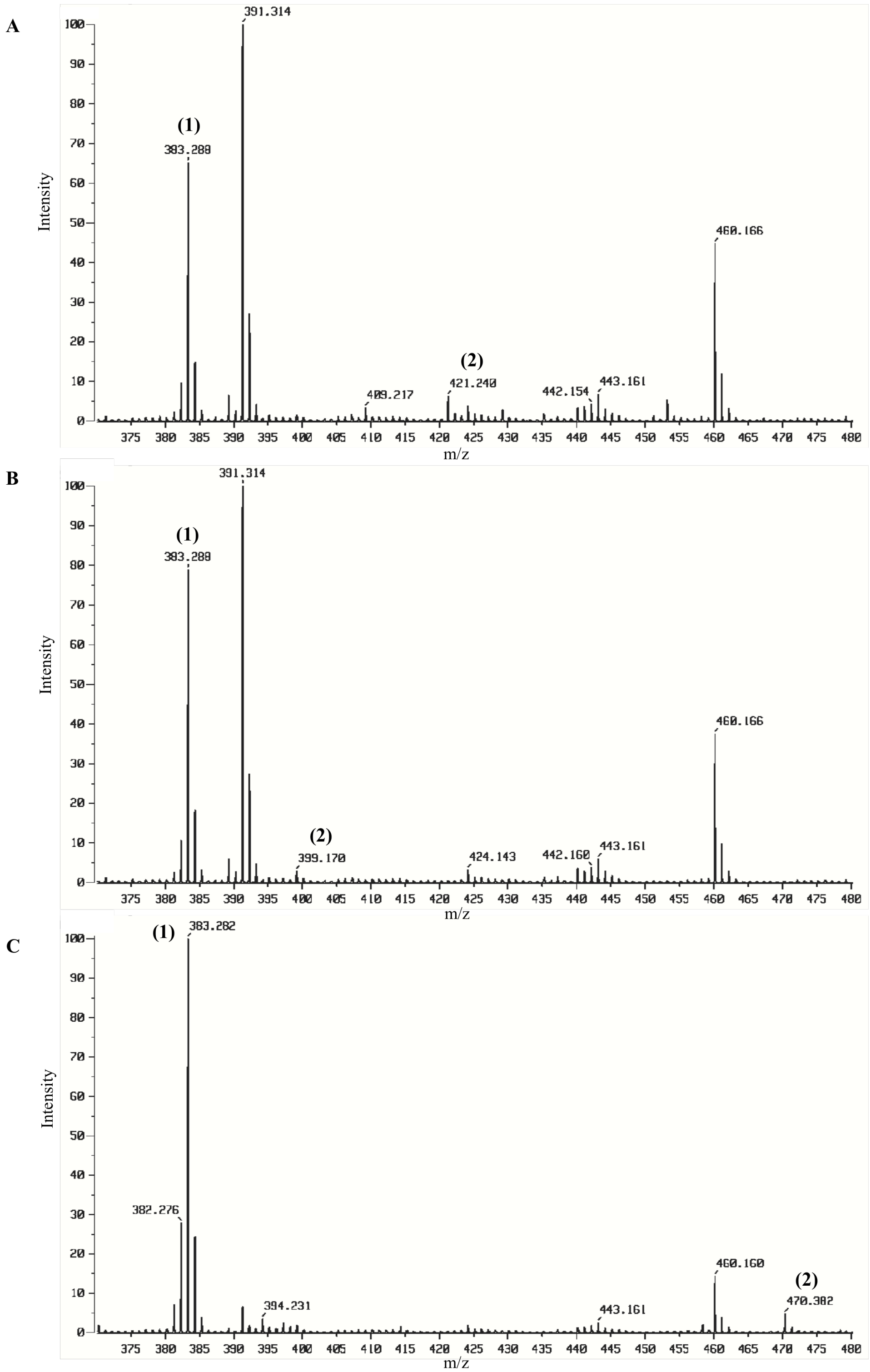

Figure 3.21 FAB mass spectrum of A. II•K$^+$ host–guest system. (1) [II + H]$^+$, (2) [II + K]$^+$. B. II•NH$_4^+$ host–guest system. (1) [II + H]$^+$, (2) [II + NH$_4$]$^+$. C. II•CH$_3$(CH$_2$)$_4$NH$_3^+$ host–guest system. (1) [II + H]$^+$, (2) [II + CH$_3$(CH$_2$)$_4$NH$_3$]$^+$. Conditions: [II] = 4x10^{-4} M, [KCl] = 1x10^{-3} M, in acetonitrile, gun voltage = 3 kV, accelerating voltage = 10 kV, emission current = 5 mA, pressure = 10^{-5} Torr, Xe gas.

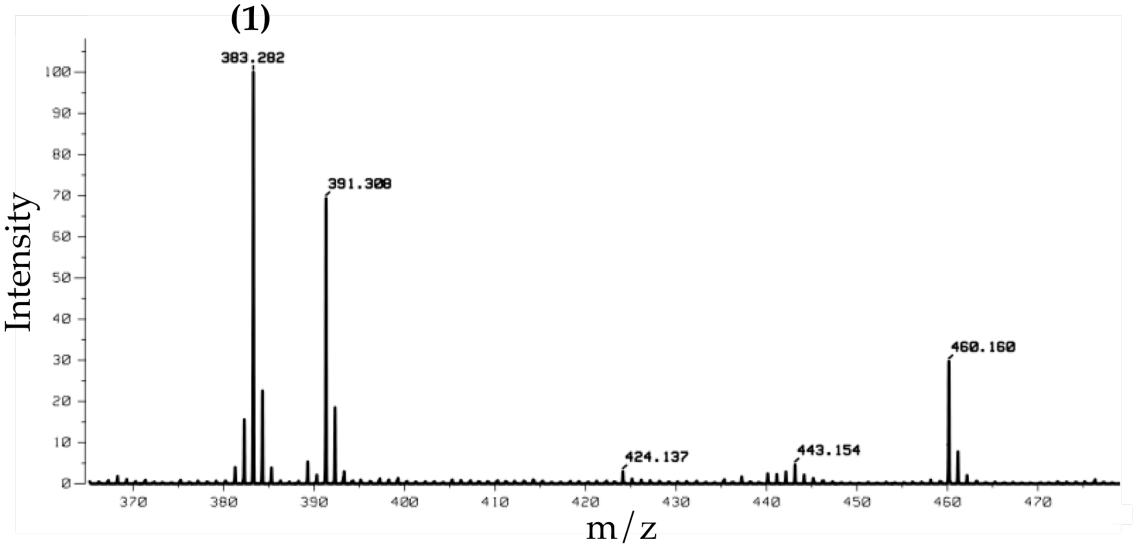

Figure 3.22 FAB mass spectrum of A. II•$CH_3NH_3^+$ host–guest system. (1) $[II + H]^+$. Conditions: [II] = $4x10^{-4}$ M, [KCl] = $1x10^{-3}$ M, in acetonitrile, gun voltage = 3 kV, accelerating voltage = 10 kV, emission current = 5 mA, pressure = 10^{-5} Torr, Xe gas.

Assemblies between **III** and K^+, NH_4^+ and $CH_3NH_3^+$, and $CH_3(CH_2)_4NH_3^+$ were also studied in acetonitrile using FAB-MS, Figures 3.23-3.25. Host-guest complex formation was only observed for complexes between **III** and K^+ and $CH_3(CH_2)_4NH_3^+$, Figure 3.23.

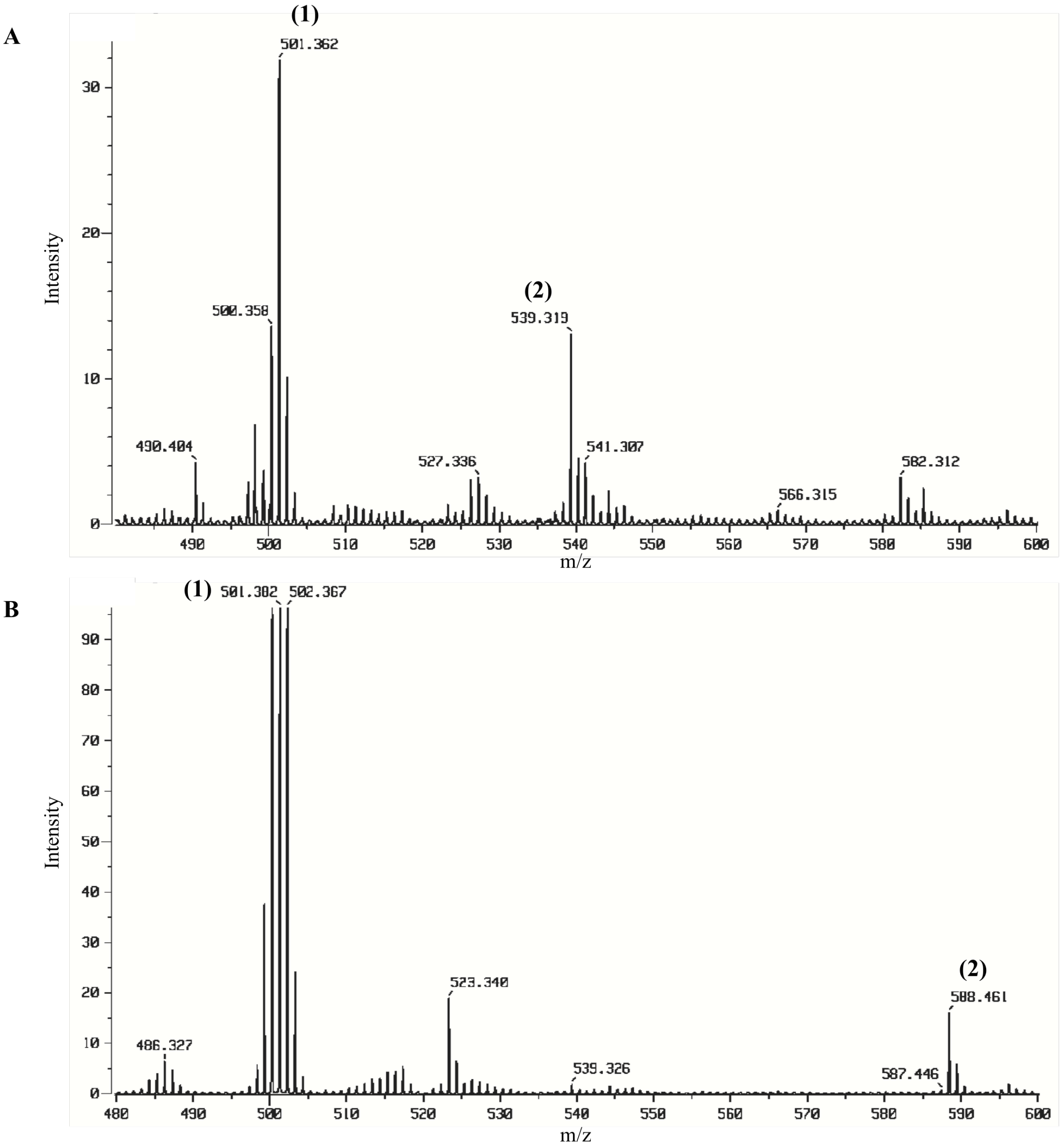

Figure 3.23 FAB mass spectrum of A. III•K$^+$ host–guest system. (1) [III + H]$^+$, (2) [III + K]$^+$. B. III•$CH_3(CH_2)_4NH_3^+$ host–guest system. (1) [III + H]$^+$, (2) [III + $CH_3(CH_2)_4NH_3$]$^+$. Conditions: [III] = 4x10^{-4} M, [KCl] = 1x10^{-3} M, in acetonitrile, gun voltage = 3 kV, accelerating voltage = 10 kV, emission current = 5 mA, pressure = 10^{-5} Torr, Xe gas.

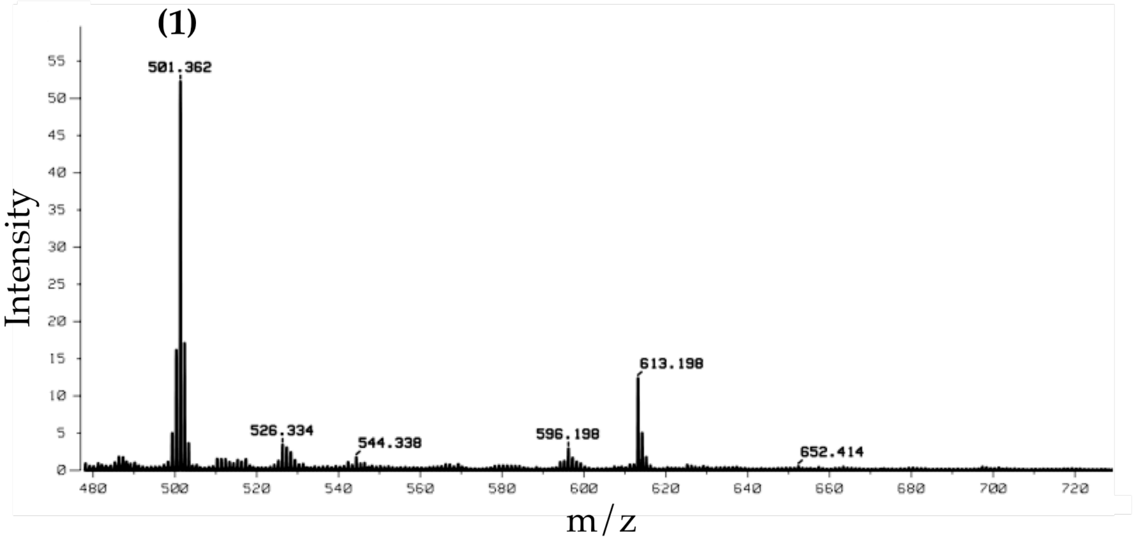

Figure 3.24 FAB mass spectrum of III•NH_4^+ host–guest system. (1) [III + H]$^+$. Conditions: [III] = 4x10^{-4} M, [KCl] = 1x10^{-3} M, in acetonitrile, gun voltage = 3 kV, accelerating voltage = 10 kV, emission current = 5 mA, pressure = 10^{-5} Torr, Xe gas.

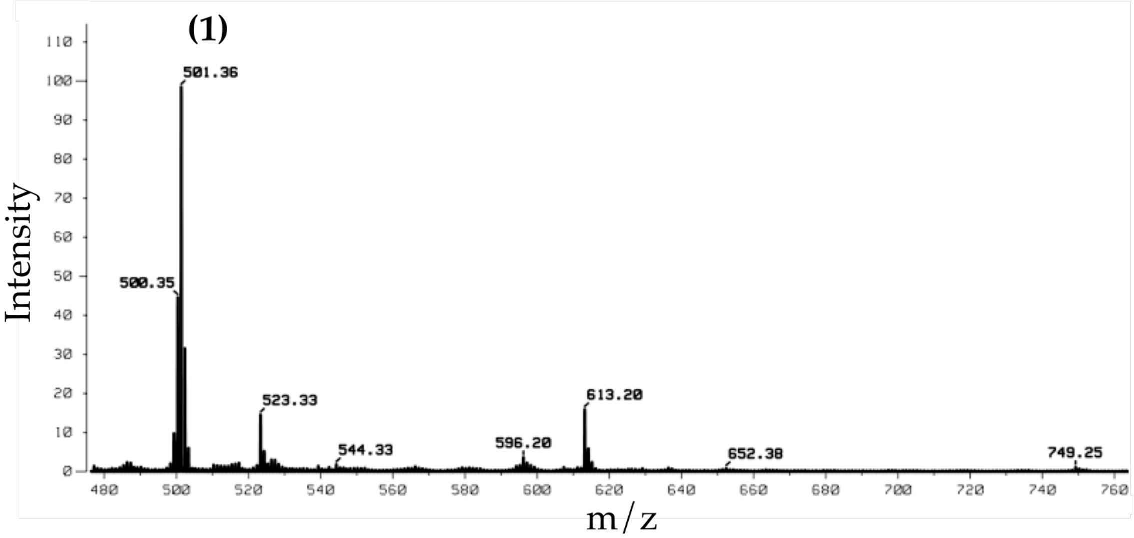

Figure 3.25 FAB mass spectrum of III•$CH_3NH_3^+$ host–guest system. (1) [III + H]$^+$. Conditions: [III] = 4x10^{-4} M, [KCl] = 1x10^{-3} M, in acetonitrile, gun voltage = 3 kV, accelerating voltage = 10 kV, emission current = 5 mA, pressure = 10^{-5} Torr, Xe gas.

Formation of a host-guest complex was observed in the case of **II** and FeHDFB$^+$ and **II** and FeHDFB$^+$ in acetonitrile. Peaks were observed for **II** at 383 m/z, FeHDFB at

614 m/z, and the **II**•FeHDFB$^+$ host-guest complex at 996 m/z (Figure 3.26A). Peaks were observed for **III** at 501 m/z, FeHDFB at 614 m/z, and the **III**•FeHDFB$^+$ host-guest complex at 1114 m/z (Figure 3.26B).

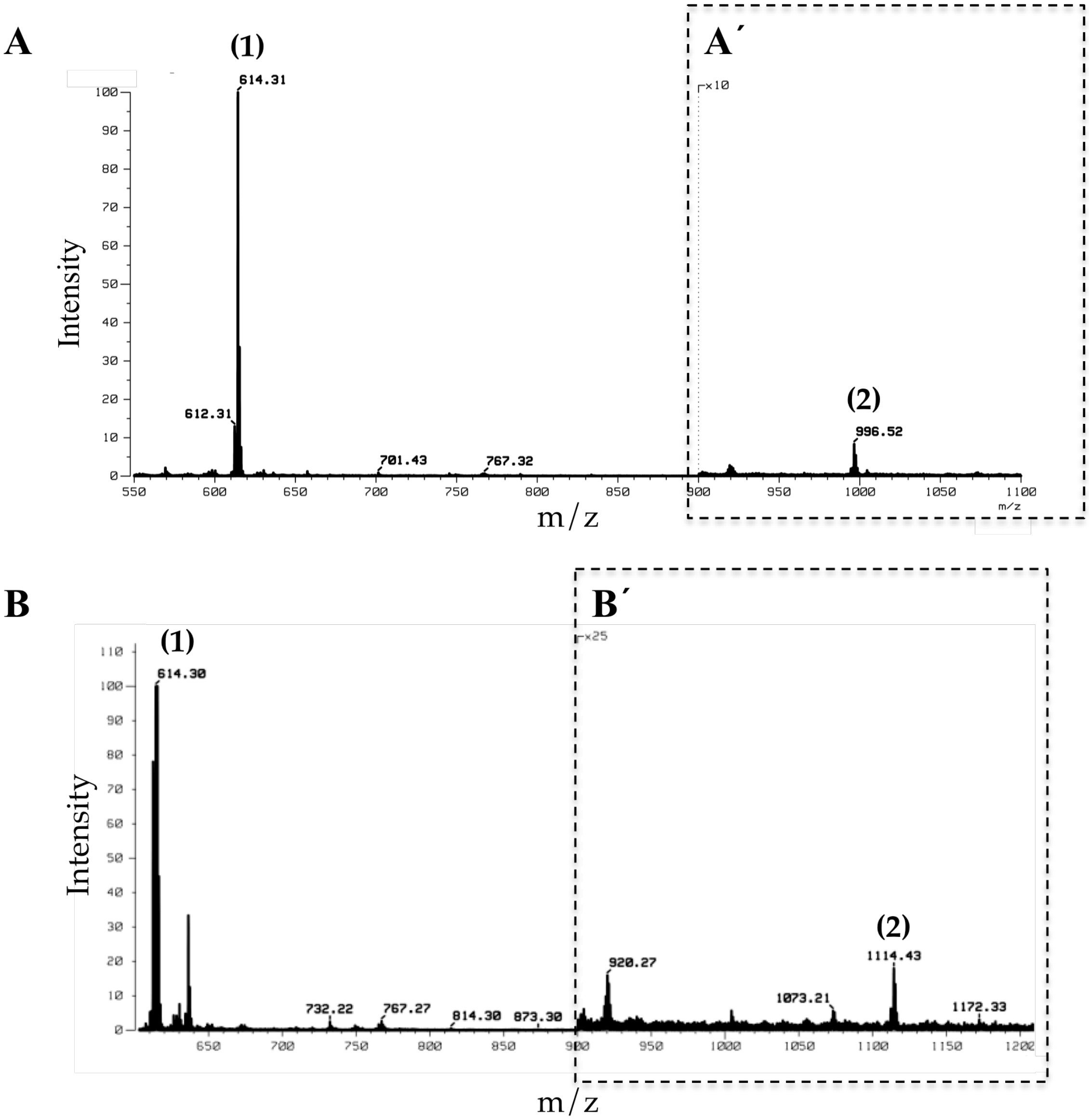

Figure 3.26 FAB mass spectrum of A. II•FeHDFB$^+$ host–guest system. (1) FeHDFB$^+$, (2) [II + FeHDFB]$^+$. A´ shows a 10x intensity magnification of a section of the spectrum. B. III•FeHDFB$^+$ host–guest system. (1) FeHDFB$^+$, (2) [III + FeHDFB]$^+$. B´ shows a 25x intensity magnification of a section of the spectrum. Conditions: [II] = [III] = 4×10^{-4} M, [FeHDFB$^+$] = 1×10^{-3} M, in acetonitrile, gun voltage = 3 kV, accelerating voltage = 10 kV, emission current = 5 mA, pressure = 10^{-5} Torr, Xe gas.

As with the other Wurster's crown host-guest complexes studied by FAB-MS, the intensities of the host guest complex peaks for these two systems are very low and intensity maginifications of 10x and 25x are needed, respectively, for these peaks to be noticeable in the spectra. This presented a problem for monitoring these peaks as a function of concentration since, at lower concentrations, these peaks were not present. This made it impossible to adapt the method developed in Chapter 2 to FAB-MS. It is likely that these aza-crown host-guest complexes are not as strongly associated as those previously studied with 18C6. In general, replacement of oxygen donor atoms by nitrogen atoms decreases the binding affinity of cationic species to a crown cavity [51]. The presence of the N,N,N',N'-tetraalkyl-1,4-phenylenediamine in the aza-crown, may also alter the geometry of the binding pocket or make binding sterically difficult due to the presence of the ring in comparison to binding in a crown ether cavity. It is also possible that the host-guest complex assembly does not ionize as well as previously studied assemblies.

Even though no association constants were calculated, mass spectral evidence of host-guest complex formation was observed between **II** and K^+, NH_4^+, $CH_3(CH_2)_4NH_3^+$, and $FeHDFB^+$, and between **III** and K^+, $CH_3(CH_2)_4NH_3^+$, and $FeHDFB^+$ in acetonitrile using FAB-MS. This lends credence to the hypothesis that the shift in redox potential observed upon addition of a cationic guest to a solution of Wurster's crown is the result of host-guest complex formation.

3.4.3 Microcalorimetric Determination of the Thermodymamic Parameters of Host-Guest Complex Formation

3.4.3.1 Determination of Affinity Constants Using ITC

In order to further characterize host-guest complex formation between a Wurster's crown and the cationic guests studied in this Chapter, including the siderophore guest $FeHDFB^+$, we aimed to obtain binding constants of the complexes formed between **II** in its native reduced state and the guests mentioned previously via ITC.

Initially, the binding between **II** and protonated methylamine and pentylamine, H_4DFB^+, and $FeHDFB^+$ was studied in acetonitrile, so as to correlate the data with those previously obtained using FAB-MS. However, this solvent presented many obstacles, and no usable ITC data could be obtained. Although the systems under study should show exothermic calorimetry data upon host-guest complex formation, only endothermic scatter was obtained in this solvent. Methanol was chosen as the solvent instead since it had been shown to produce reasonable data for systems involving 18C6 and a range of protonated amine guests (see Experimental Section).

Injecting **II** into methylamine or pentylamine in MeOH resulted in thermograms displaying saturation behavior (*C* values of 10 and 7.5, respectively). The thermograms were integrated and binding isotherms were obtained whose fit to a single site binding model gave a stoichiometry between n = 0.1 and n = 0.2, Figures 3.27-3.28. This behavior was also observed when injecting 18C6 into the same guests (Figures 3.13-3.14) and indicated a binding ratio other than 1:1. The association constants obtained from these data in MeOH are shown in Table 3.4 ($\log K_a = 3.60 \pm 0.02$ and $\log K_a = 3.47 \pm 0.03$ for methylamine and pentylamine, respectively). These values are comparable to those obtained for 18C6 with the same guests using ITC in MeOH ($\log K_a = 3.59 \pm 0.09$ and $\log K_a = 3.57 \pm 0.07$ for methylamine and pentylamine, respectively, Table 3.3).

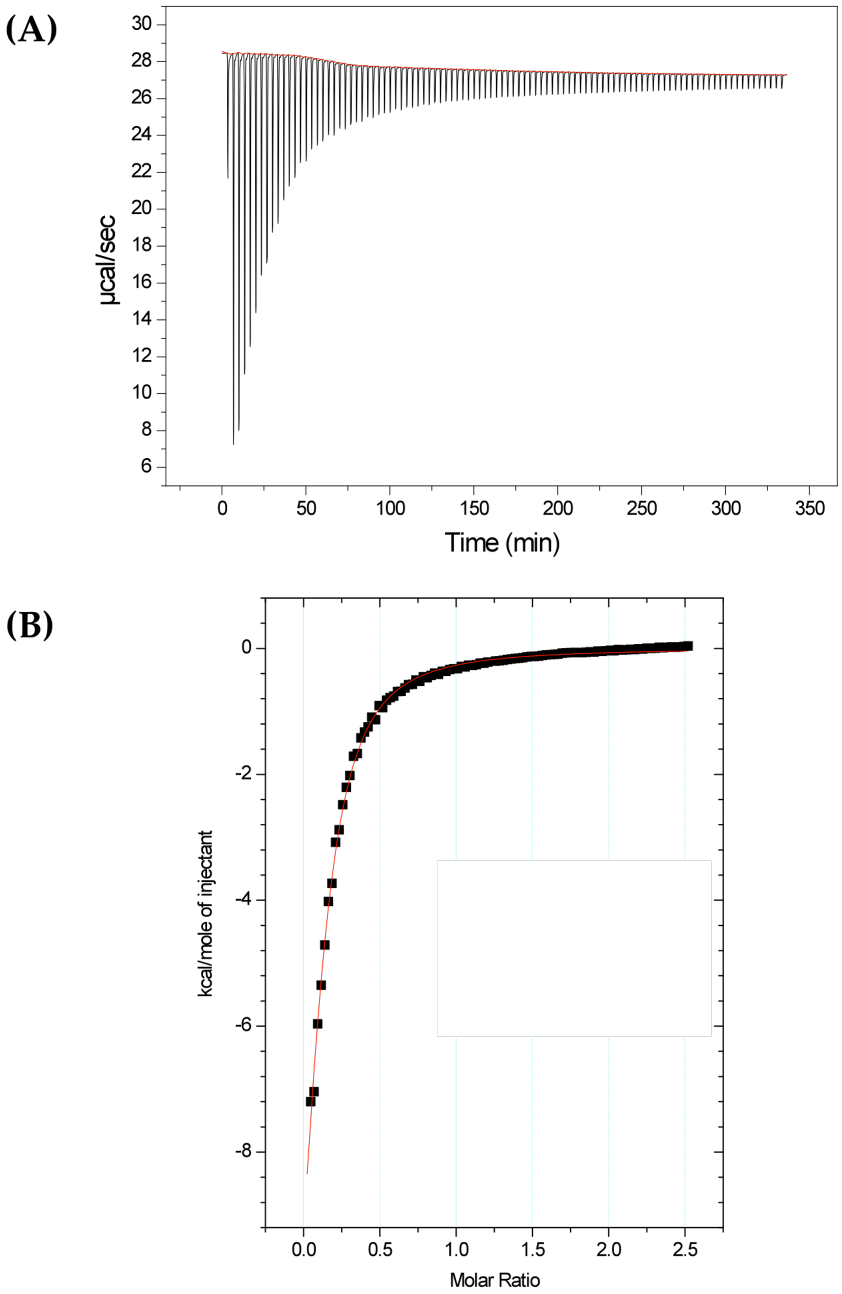

Figure 3.27 Thermogram (A) and binding isotherm (B) showing the addition of II into $CH_3NH_3^+$ in MeOH. Conditions: [II] = 32.5 mM in syringe, $[CH_3NH_3^+]$ = 2.5 mM in sample cell, MeOH in reference cell, T = 25 °C. From the curve fit (using Origin software), the following parameters have been determined: the association constant, K = (3.97 ± 0.20)× 10^3 M^{-1}, the enthalpy, ΔH° = -14.8 ± 0.07 kcal/mol, and the stoichiometry, n = 0.13 ± 0.01.

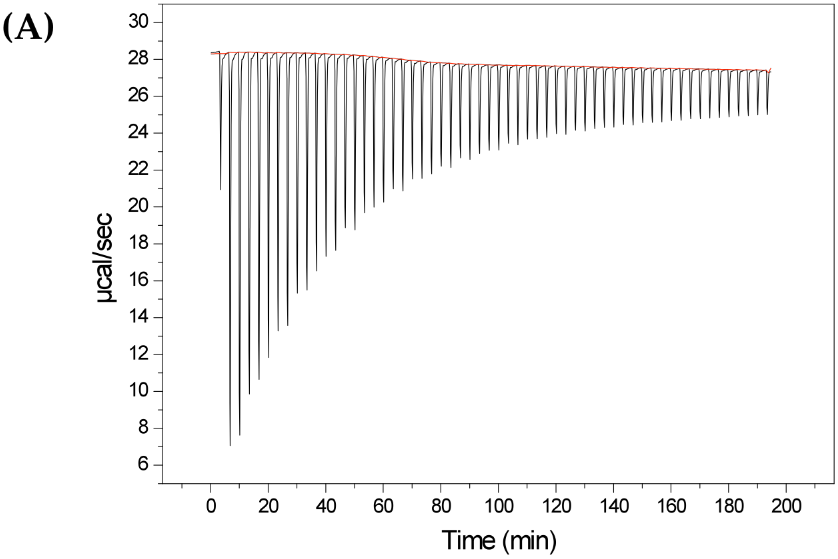

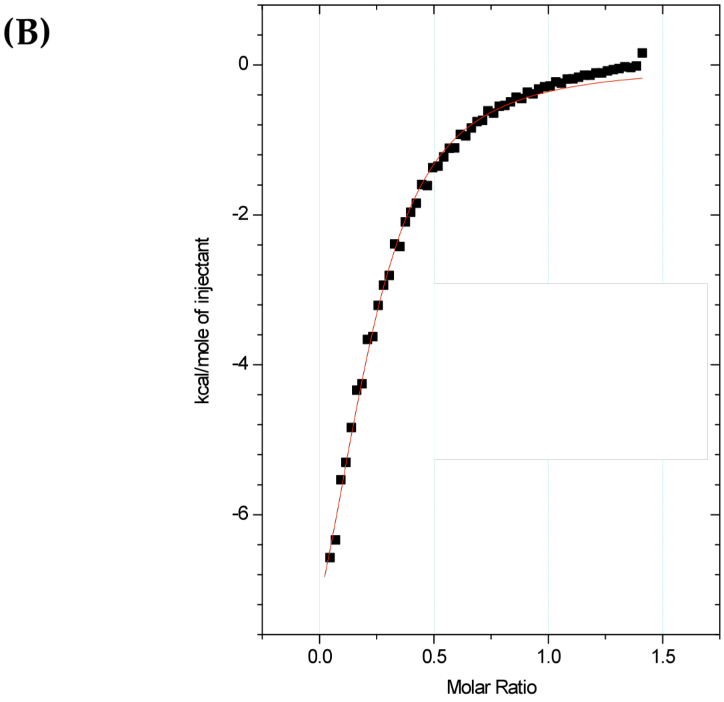

Figure 3.28 Thermogram (A) and binding isotherm (B) showing the addition of II into $CH_3(CH_2)_4NH_3^+$ in MeOH. Conditions: [II] = 32.5 mM in syringe, $[CH_3(CH_2)_4NH_3^+]$ = 2.5 mM in sample cell, MeOH in reference cell, T = 25 °C. From the curve fit (using Origin software), the following parameters have been determined: the association constant, $K_a = (2.98 \pm 0.18)\times 10^3\ M^{-1}$, the enthalpy, $\Delta H = -11.4 \pm 0.05$ kcal/mol, and the stoichiometry, $n = 0.22 \pm 0.01$.

Injecting **II** into H_4DFB^+ in MeOH resulted in a thermogram displaying sigmoidal behavior (*C* value of 14). The thermogram was integrated and a binding isotherm was obtained whose fit to a single site binding model gave a stoichiometry of n~1.0, Figure 3.29. This behavior indicates a conformation where one guest binds to every crown ether host. The association constants obtained from these data are shown in Table 3.4. The value obtained ($\log K_a = 3.74 \pm 0.02$) is lower than that obtained for 18C6 with the same guest in MeOH ($\log K_a = 4.07 \pm 0.05$, Table 3.3), confirming that the assembly formed between **II** and H_4DFB^+ is less stable than that with 18C6, as expected based on the replacement of oxygen atoms by nitrogen atoms in the aza-crown host [51]. The lower binding affinity for the larger cationic guest H_4DFB^+ could be attributed to steric hindrance to the binding pocket caused by the N,N,N′,N′-tetraalkyl-1,4-phenylenediamine moiety on the Wurster's crown., since this group is positioned perpendicular to the crown ring. This would not be a factor for smaller cationic guests, such as protonated methylamine and pentylamine, but would affect a cationic guest such as H_4DFB^+.

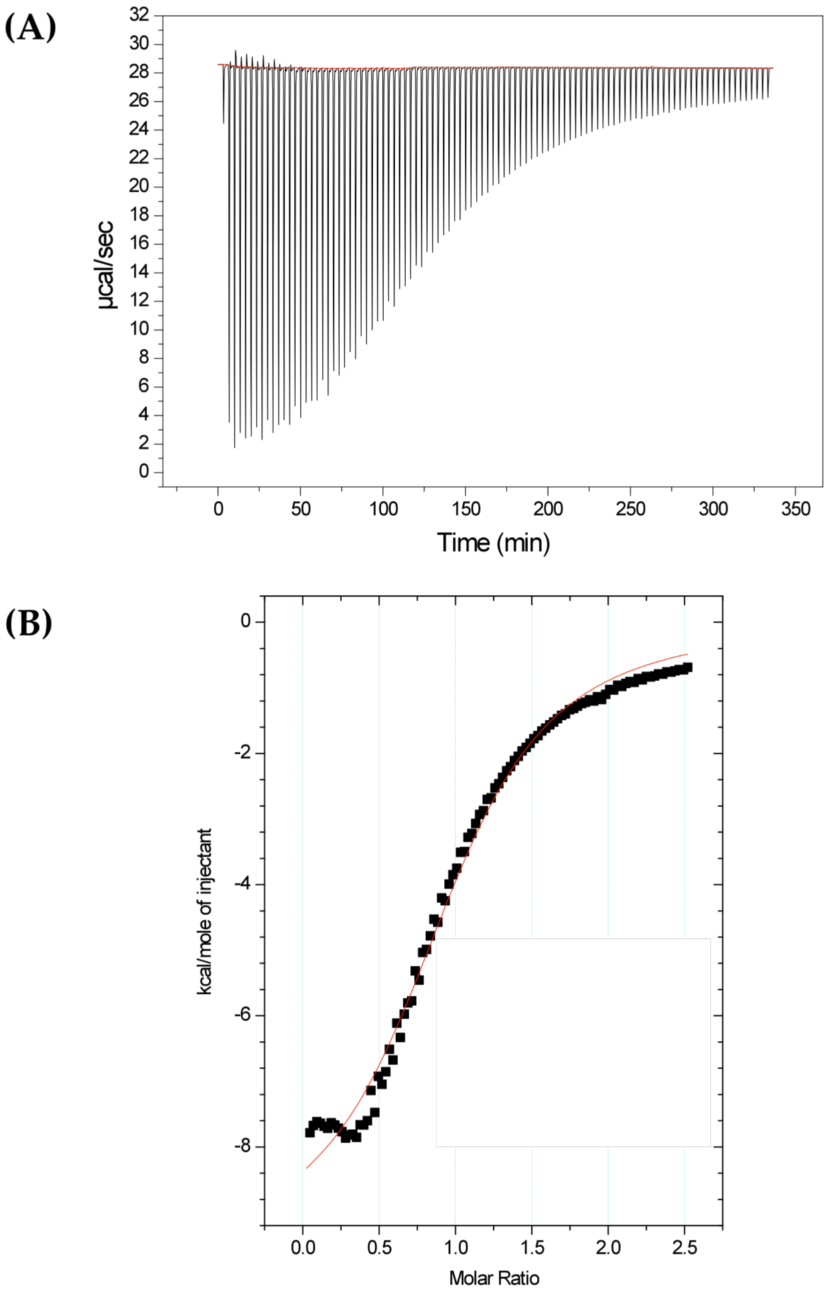

Figure 3.29 Thermogram (A) and binding isotherm (B) showing the addition of II into H_4DFB^+ in MeOH. Conditions: [II] = 32.5 mM in syringe, [H_4DFB^+] = 2.5 mM in sample cell, MeOH in reference cell, T = 25 °C. From the curve fit (using Origin software), the following parameters have been determined: the association constant, $K_a = (5.52 \pm 0.30) \times 10^3\ M^{-1}$, the enthalpy, $\Delta H = -7.86 \pm 0.08$ kcal/mol, and the stoichiometry, $n = 0.92 \pm 0.01$.

Injecting **II** into FeHDFB$^+$ in MeOH resulted in a thermogram displaying very high heats of dilution, meaning that too much heat was liberated upon injection and so each thermogram peak continues past the baseline in the upwards direction, Figure 3.30. In addition, each peak reached the limit of accurate detection of the calorimeter (-40 μcal/sec). Decreasing the concentration of guest in the sample cell did not change the behavior observed (data not shown). Due to the complications listed above, no useful data could be obtained for this system.

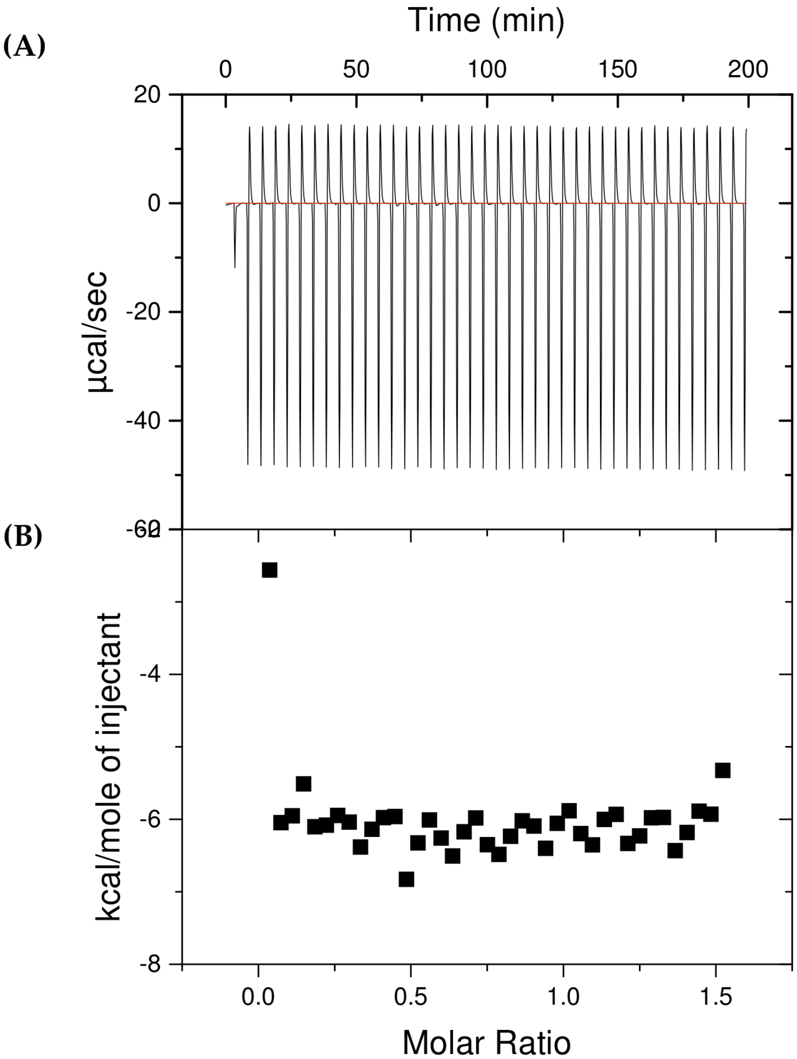

Figure 3.30 Thermogram (A) and binding isotherm (B) showing the addition of II into FeHDFB$^+$ in MeOH. Conditions: [II] = 65 mM in syringe, [FeHDFB$^+$] = 2.5 mM in sample cell, MeOH in reference cell, T = 25 °C. No parameters could be determined.

In an effort to understand the behavior observed above, independent experiments were conducted to study the effects of injecting **II** into MeOH, and MeOH into FeHDFB$^+$ in MeOH. Injecting **II** into MeOH resulted in a thermogram equivalent to a straight line, Figure 3.31. Although upon first glance it seems to display saturation behavior, the scale at which this behavior is observed is too small to be taken into account. These data indicate that **II** alone is not responsible for the large heats of dilution observed when **II** is injected into FeHDFB$^+$.

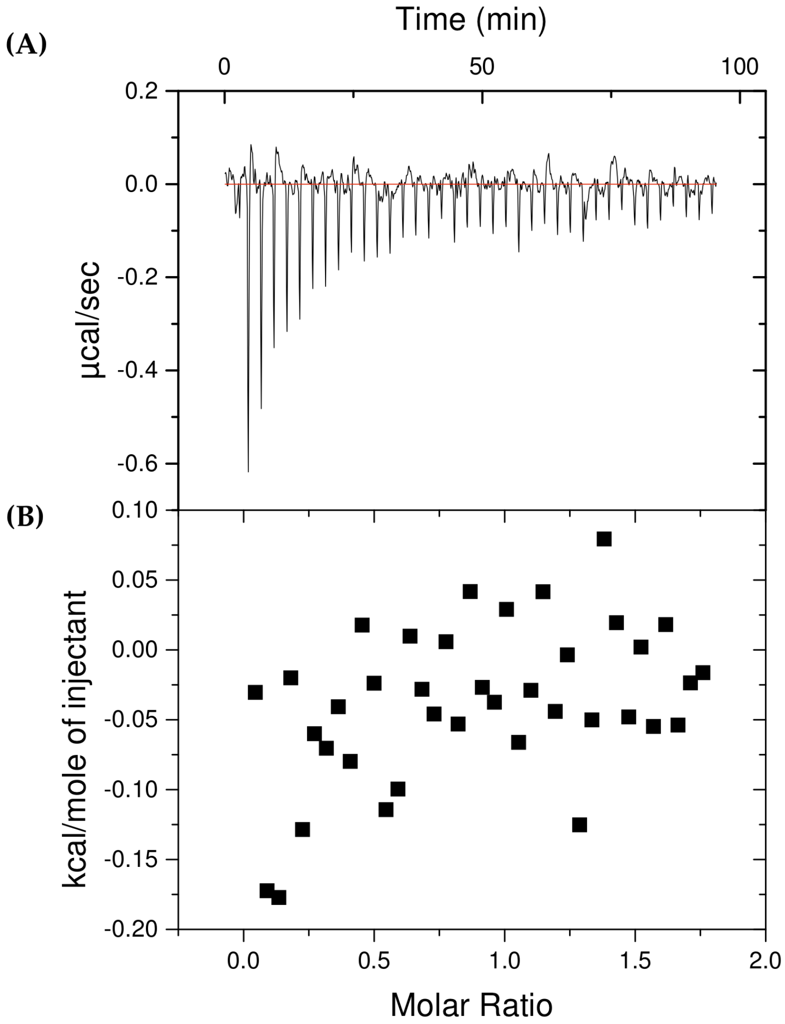

Figure 3.31 Thermogram (A) and binding isotherm (B) showing the addition of II into MeOH. Conditions: [II] = 65 mM in syringe, MeOH in sample cell, MeOH in reference cell, T = 25 °C.

A dilution experiment whereby MeOH was injected into FeHDFB$^+$ in MeOH solvent resulted in a thermogram similar to that observed when injecting **II** into FeHDFB$^+$, but to a smaller scale (Figure 3.32). This indicates that when a new component (be it **II** or MeOH solvent) is injected into FeHDFB$^+$ the amount of heat released is too great to be accurately measured by the calorimeter. This is true regardless of the concentration of FeHDFB$^+$, within a reasonable limit of *C* value (data not shown).

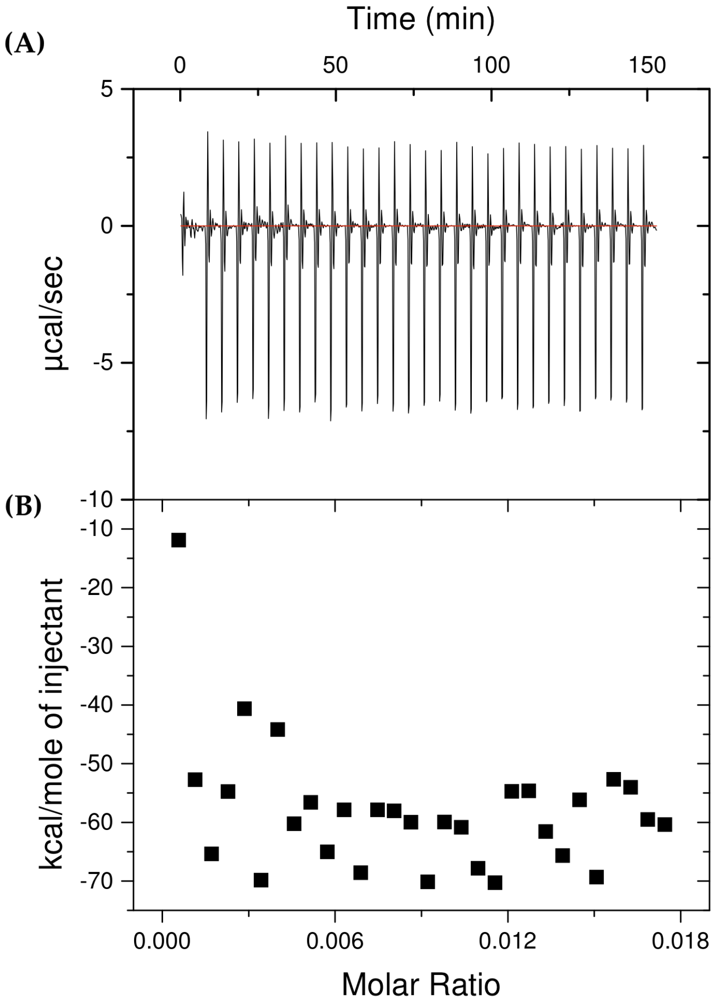

Figure 3.32 Thermogram (A) and binding isotherm (B) showing the addition of MeOH into FeHDFB$^+$ in MeOH. Conditions: MeOH in syringe, [FeHDFB$^+$] = 2.5 mM in sample cell, MeOH in reference cell, T = 25 °C.

Table 3.4 Thermodynamic Parameters of Cation Binding to Wurster's Crown II in MeOH using ITC[a]

Cationic Guest	[Guest] (mM)	[Host] (mM)	n	ΔH (kcal/mol)	log K_a
$CH_3NH_3^+$	2.5	32.5	0.13 ± 0.01	-1.48 ± 0.07	3.60 ± 0.02
$CH_3(CH_2)_4NH_3^+$	2.5	32.5	0.22 ± 0.01	-1.14 ± 0.05	3.47 ± 0.03
H_4DFB^+	2.5	32.5	0.92 ± 0.1	-7.86 ± 0.08	3.74 ± 0.02

[a] Data obtained from ITC measurements, Figures 3.29-3.31.

In summary, using ITC we successfully obtained binding affinities between **II** and methylamine, pentylamine, and H_4DFB^+ (Figures 3.27-3.29, Table 3.4). Although not all binding affinity values correlate with previous data, these data do demonstrate that there is binding between the Wurster's crown host and guests, which strengthens our host-guest complex hypothesis.

3.5 Discussion

Based on previous observations by Wirgau [38,87], it is clear that there is a shift in redox potential upon the addition of a cationic guest to a solution of Wurster's crown host. We hypothesized that this binding was due to host-guest complex formation between the Wurster's crown and the cationic guest. This was successfully shown by FAB-MS studies (Figures 3.21-3.36). ITC data further demonstrated that binding occurred between a Wurster's crown and cationic guests, with binding affinities for the reduced form of the host and cations on the order of 10^3 M^{-1} (Figures 3.27-3.29, Table 3.4), which is an order of magnitude lower than binding between 18C6 and the cationic guests studied (Table 3.3) [37]. Replacement of the oxygen donor atoms by nitrogen atoms in the aza-crown is expected to result in lower binding affinities to cationic species [51]. The addition of the N,N,N′,N′-tetraalkyl-1,4-phenylenediamine moiety to the crown may result in added steric hindrance to binding of a cationic guest.

A closed thermodynamic cycle can be derived to illustrate the changes in binding affinity that occur as a result of redox state of the host, Figure 3.33.

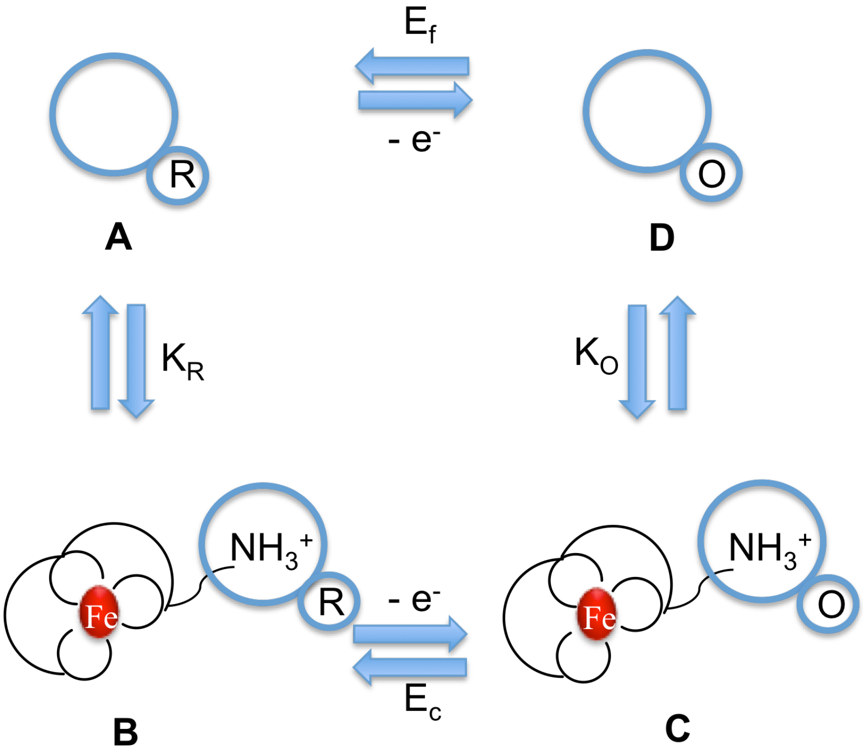

Figure 3.33 Thermochemical cycle describing oxidation/reduction of free aza crown ether (A⇔D), oxidation/reduction of the host-guest assembly (B⇔C), and host-guest assembly formation for the reduced (A⇔B) and oxidized (D⇔C) form of the host. See Equation (3.1) for the derived algebraic relationship based on this thermochemical cycle. Figure adapted from reference [38].

Equation 3.1 may be derived for this thermodynamic cycle, where K_R is the binding constant of the reduced aza crown ether host for the cationic guest, K_O is the binding constant of the oxidized aza crown ether host for the cationic guest, n is the number of electrons transferred, F is Faraday's constant, E_f is the reduction potential of the aza crown ether, and E_c is the reduction potential of the host-guest assembly [95].

$$K_R \,/\, K_O = \exp\{-nF\,(E_f - E_c)\,/\,RT) \qquad (3.1)$$

Equation 3.1 demonstrates that a shift in observed reduction potential indicates there is a corresponding change in the relative stability of the host-guest assembly between the oxidized and reduced form of the host. A positive shift in reduction potentials ($E_f - E_c < 0$) indicates $K_R/K_O > 1$ and that the reduced form of the aza crown ether host provides a more stable host-guest assembly than in the oxidized state. This loss in stability can be explained in that the first oxidation of the redox moiety generates a delocalized radical cation, making the insertion of a cation guest into the crown binding pocket less favorable.

The changes in redox aza crown affinity for $FeHDFB^+$ with changes in oxidation state of the hosts **II** and **III** in acetonitrile and chloroform are shown in Tables 3.1 and 3.2. Larger binding enhancements are observed for **II** over **III** both in acetonitrile ($K_R/K_O > 10^2$ vs. 10^1) and cloroform ($K_R/K_O = 10^9$ vs. 10^7), with binding enhancements in cloroform being larger than in acetonitrile. The smaller binding enhancements observed for **III** in both solvents can be explained in that **III** can better delocalize the positive charge obtained upon oxidation due to the presence of the two aza groups. The larger shifts ($\Delta E_{1/2}$) and binding enhancements (K_R/K_O) in chloroform compared to those in acetonitrile can be explained by the ability of acetonitrile to act as a H-bond acceptor and compete with the aza crowns for the protonated amine arm of the cationic guest ($FeHDFB^+$, Figure 3.1). Literature data support this explanation as the crown ether 18C6 binds t-$C_4H_9NH_3^+$ more tightly in chloroform than acetonitrile (log K = 7.36 [96] and 3.54 [97], respectively).

3.6 Summary and Conclusions

A shift in reduction potential towards more positive values is observed upon addition of a cationic siderophore guest to a solution of either a *para*-Wurster's crown (**III**) or a mono-substituted Wurster's crown (**II**) [87]. We have established through FAB-MS that the observed electrochemical behavior can be explained in terms of host-guest complex formation, through H-bond interaction of the protonated amine arm of

$FeHDFB^+$ with the aza crown cavity. Efforts towards independently establishing host-guest complex formation using the previously developed ESI-MS method failed in that host-guest complex formation was not detected for all complexes of interest, and no association constants were determined using this technique. This could be due to the oxidation of the Wurster's crowns in the ESI instrument, which would result in a positive charge within the ring and weaker host-guest complex formation, which may not be detected by the instrument. Evidence of this host-guest complex formation was obtained between **II** and K^+, NH_4^+, $CH_3(CH_2)_4NH_3^+$, and $FeHDFB^+$, and between **III** and K^+, $CH_3(CH_2)_4NH_3^+$, and $FeHDFB^+$ using FAB-MS. Although host-guest complex formation was observed, the intensity of the host-guest complex peak was too low to be monitored over a range of concentrations, and so no association constants could be obtained.

To further characterize host-guest complex formation, the thermodynamic parameters of binding between **II** and protonated methylamine and pentylamine, and H_4DFB^+ were obtained in MeOH using ITC. The binding constants obtained show that binding between **II** and protonated methylamine and pentylamine is comparable to that observed for 18C6 and these cationic guests. Binding between **II** and H_4DFB^+ is one order of magnitude weaker than the binding observed for 18C6 and H_4DFB^+. This weaker binding is likely due to the replacement of oxygen donor atoms with nitrogen atoms [51], and to steric hindrance resulting from the presence of the N,N,N′,N′-tetraalkyl-1,4-phenylenediamine moiety, which affects the binding of a larger cationic guest such as H_4DFB^+.

The shift in redox potential observed upon addition of a guest to **II** or **III** represents a difference in binding affinity between the reduced and oxidized forms of the host. A closed thermodynamic cycle can be derived showing the corresponding change in the relative stability of the host-guest assembly between the oxidized and reduced forms of the host (Figure 3.33).

The systems studied here present a unique means by which to modulate the uptake or release of ionic guests from a cavity by using externally controlled methods. Redox-active macrocyclic ligands such as **II** and **III**, whose binding affinities to guests can be controlled by redox potential, have many potential uses in the biological and environmental fields and deserve to be studied further.

3.7 Application to Selective Metal Ion Compartmentalization

The data and discussion presented in this Chapter serve as proof of principle that an ion selective chelator, such as H_4DFB^+, in combination with a redox tunable selective host, such as **II** and **III**, can undergo ion recognition through first coordination shell interactions and specifically bind and sequester a metal ion, in this case Fe^{3+}, in the presence of other metals (Figure 3.34, left side). A unique aspect of this specific chelator is the presence of a recognition factor in the form of a pendant protonated amine side-chain. Due to the presence of this recognition factor, this metal complex, $FeHDFB^+$, can subsequently undergo a molecular recognition event with a redox active host though second coordination shell interactions between the redox-active host and the protonated pendant amine, creating a host-guest complex (Figure 3.34, **B**). The affinity of this redox-active host for the guest depends on the redox state of the host, and is larger for the reduced form of the host (Figure 3.34, **B**), as demonstrated by our electrochemical studies. Upon oxidation of the host (Figure 3.34, **C**), the affinity for the guest decreases and the release of the guest is facilitated, and the free redox-active host can cycle back to its reduced form (Figure 3.34, **A**), where it can again pick up the metal complex guest. This combination of bulk liquid membrane transport with a redox switch in principle creates a unidirectional flow of guest from one side of the membrane to the other, resulting in facilitated transport, and compartmentalization and concentration of the metal. This application to selective metal ion compartmentalization can be harnessed for use in toxic waste cleanup and other environmental purposes.

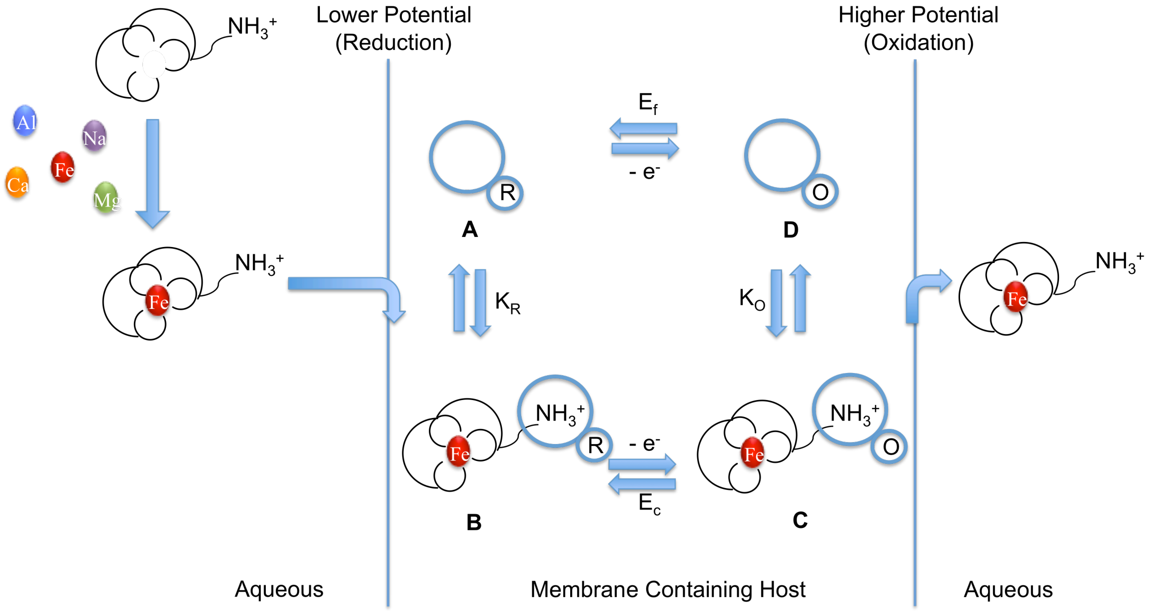

Figure 3.34 Central segment A–B-C-D. Thermochemical cycle describing oxidation/reduction of free aza crown ether (A⇔D), oxidation/reduction of the host-guest assembly (B⇔C), and host-guest assembly formation for the reduced (A⇔B) and oxidized (D⇔C) form of the host. See Equation (1) for derived algebraic relationship based on this thermochemical cycle. When the chemical events described by the thermochemical cycle are placed in a liquid membrane separating two liquid phases with different relative applied potentials at the two interfaces this describes a prototype for selective metal ion compartmentalization. A metal specific chelator (siderophore) selectively binds Fe from a pool of metal ions. The iron-loaded siderophore undergoes a molecular recognition event at the membrane surface with a redox-active host in its reduced state (A), wherein a host-guest assembly is formed (B). Subsequent to diffusion across the membrane the host undergoes oxidation (C), upon which the affinity of the host for the siderophore guest decreases, causing the release of the siderophore guest and leaving a free host in its oxidized state (D). The host is then reduced upon diffusion across the membrane and can undergo another reduction (A) and molecular recognition event with a guest (B). Figure adapted from references [38] and [87].

4. The Trojan Horse Approach: Interactions Between the Tuberculosis Siderophore Mycobactin and the Antimalarial Drug Artemisinin

4.1 Background and Significance

Tuberculosis (TB) is one of the most widespread and lethal infectious diseases in the world. Approximately one-third of the world's population is presently infected with TB, amounting to 2 million deaths worldwide each year [98,99]. The current chemotherapeutic treatment of tuberculosis is inadequate. This is partly due to the fact that microbes are continually evolving and increasing their ability to prevent the uptake of new antibiotics, thereby developing antibiotic resistance. The development of multidrug resistant (MDR) and extensively drug resistant (XDR) forms of TB has stimulated research efforts globally [100]. MDR refers to TB that is resistant to isoniazid and rifampicin, two of the best anti-TB drugs, Figure 4.1. XDR refers to TB that is resistant to isoniazid and rifampicin, as well as any fluoroquinolone and at least one of three injectable second-line drugs such as amikacin, kanamycin, and capreomycin, Figure 4.1. A second factor contributing to the inadequacy of current drug design and delivery methods is the fact that the permeability barrier of Gram positive pathogens due to their peptidoglycan-rich cell wall is a crucial resistance factor and can effectively prevent delivery of the drug to the target site [101]. New approaches to increase the efficacy of traditional anti-bacterials and a new class of antimicrobials with novel mechanisms of action are urgently needed for the effective treatment of such human pathogens [102,103].

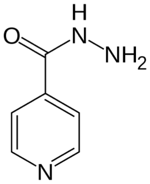

Isoniazid

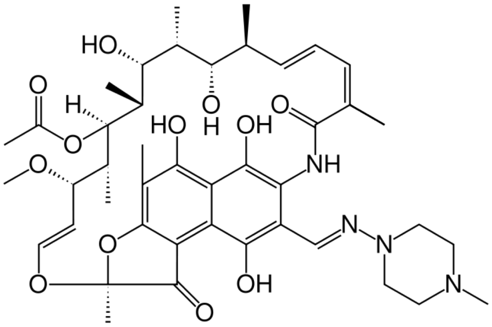

Rifampicin

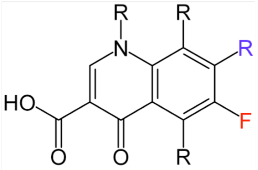

Basic structure of a fluoroquinone

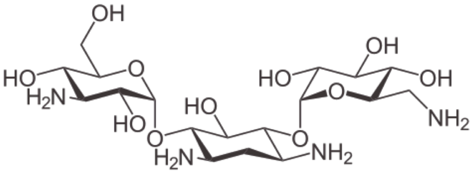

Kanamycin

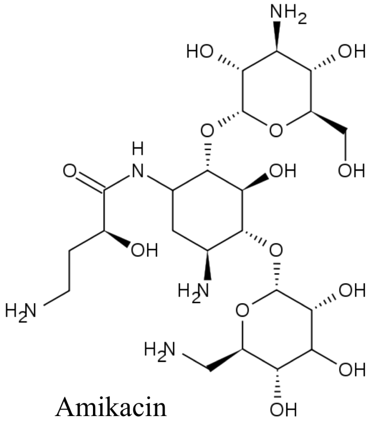

Amikacin

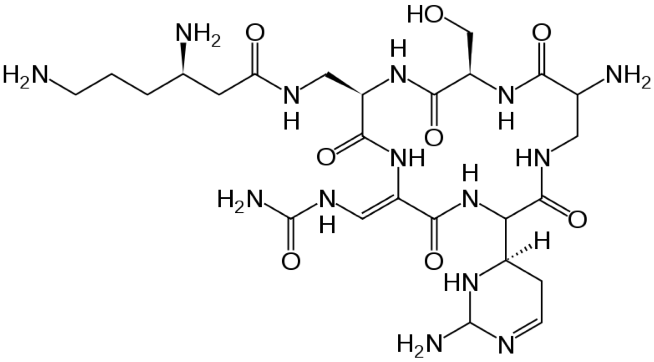

Capreomycin

Figure 4.1 Structures of anti-tuberculosis drugs currently on the market.

Although several approaches can be taken to circumvent resistance and permeability issues, the best option is to use facilitated transport by the bacterium itself. This Trojan Horse strategy takes advantage of essential bacterial nutrient uptake systems [101]. With this in mind, several natural antibiotic-mimic substrates for peptide, sugar phosphate, nucleoside, polyamine, and iron siderophore uptake routes have been studied [104]. The bacterial iron transport system is appropriate for the Trojan Horse approach due to the delicate balance of iron homeostatis in all organisms [101]. Since virulence of TB depends on its ability to assimilate iron, like most microbes, it synthesizes and utilizes siderophores, low molecular weight iron chelators that facilitate iron uptake [18]. The use of bacterial siderophores as drug delivery agents can bypass membrane-associated resistance mechanisms and increase the potency of drugs relative to passive diffusion [105], while limiting the selection of resistance to non-pathogenic mutants deficient in siderophore-receptor proteins [106].

Mycobacteria synthesize both an intracellular siderophore, termed mycobactin, and an extracellular siderophore, termed either carboxymycobactin or exochelin, depending on their composition [18]. Mycobactins have a very high affinity for iron (log K $=10^{30}$) and are suited to holding iron from competing molecules. Each mycobacterial species produces its own variation on the basic mycobactin structure (Figure 4.2). Like all siderophores, mycobactin is produced at the highest concentration when the bacteria are under iron-deficient conditions [18].

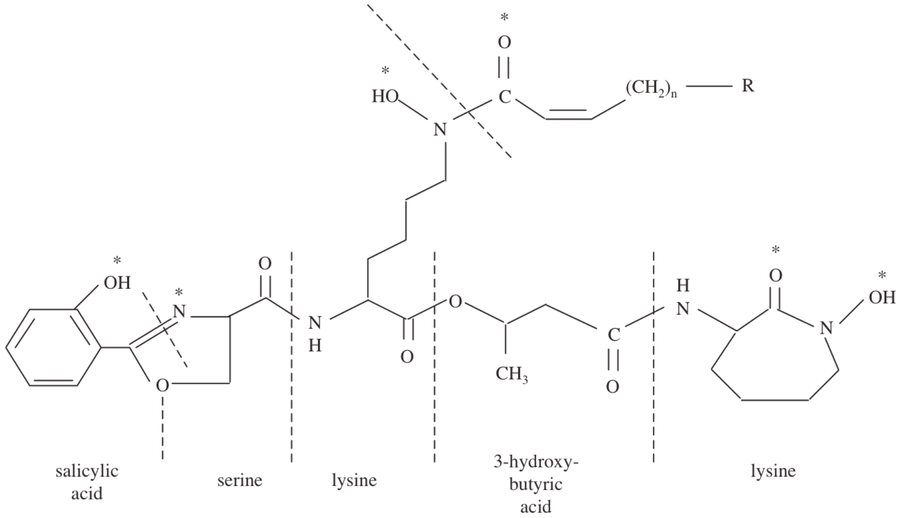

Figure 4.2 General structure of mycobactin siderophores of *M. tuberculosis*

In pathogenic mycobacteria, extracellular siderophores are collectively termed exochelins. Figure 4.3 shows the structures of exochelins MS and MN produced by *M. smegmatis* and *M. neoarum*, respectively. In *M. tuberculosis*, exochelins are variations of the mycobactin molecule, where the long alkyl chain is replaced by a shorter chain terminating in a carboxylic acid group to improve solubility. Because of the presence of this carboxylic group, the molecule has been termed carboxymycobactin [18].

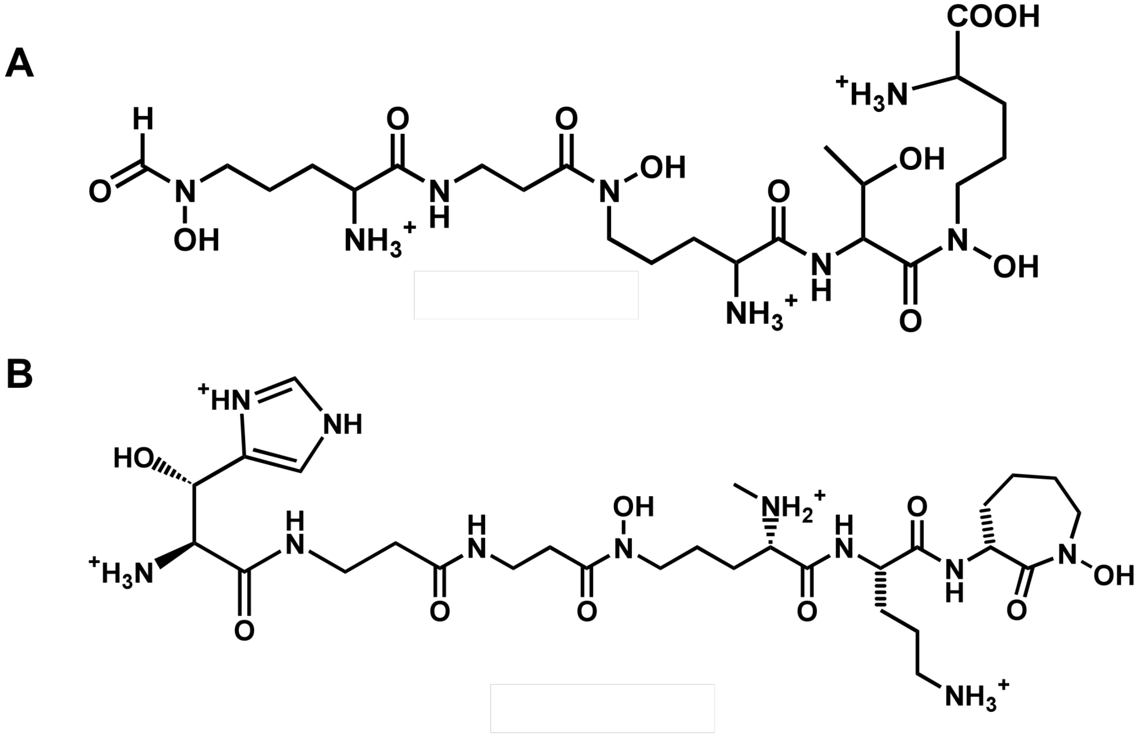

Figure 4.3 Structure of Exochelin MS (A) and Exochelin MN (B) produced by *M. smegmatis* and *M. neoarum*, respectively.

Both exochelins, in non-pathogenic bacteria, and carboxymycobactins, in pathogenic bacteria, are able to solubilize and remove iron from host sources for its uptake into the bacterial cell. Ferric exochelins and carboxymycobactins are transferred completely into the bacterial cell, although via different mechanisms. The transport of ferric exochelins across the cell membrane is an energy driven process that results in the release of iron on the cytoplasmic side of the membrane through the reduction of the ferric iron by a reductase (Figure 4.4a). After release of iron, the exochelin is transported back into the extracellular environment using an exiting protein. A second pathway (Figure 4.44b) involves the interaction between exochelin and mycobactin, which is located inside the cell envelope. The proximity of ferric exochelin to mycobactin allows mycobactin to take the iron from exochelin. Iron is held by mycobactin as a temporary, but crucial, store of iron so that its premature and unwanted release into the cytoplasm is prevented [18].

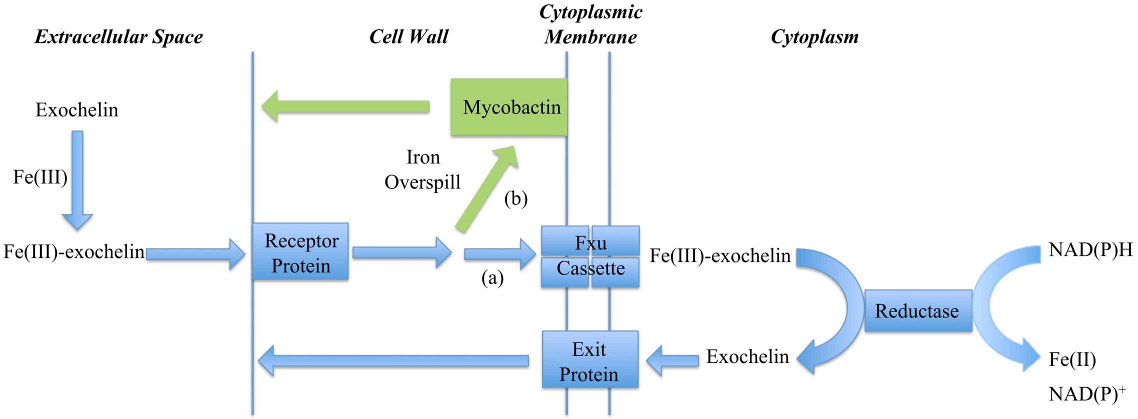

Figure 4.4 Proposed mechanism for Fe(III)-exochelin uptake into bacteria. Exochelin acquires iron from extracellular sources. It is recognized by a receptor protein and (a) enters into the cytoplasm, where the iron is reduced. Exochelin is subsequently released into the extracellular space with the help of an exit protein. Alternatively, exochelin can (b) interact with mycobactin, unload its iron for storage, and subsequently be released into the extracellular space. Adapted from Ratledge, C. *Tuberculosis* 2004, *84*, 110.

In a slightly different mechanism, carboxymycobactins are taken up by a process that is not energy linked and may involve the participation of a porin protein, Figure 4.5.

Iron can be released by the reductase mechanism used for exochelins, or could also be transferred to mycobactin for intraenvelope storage [18].

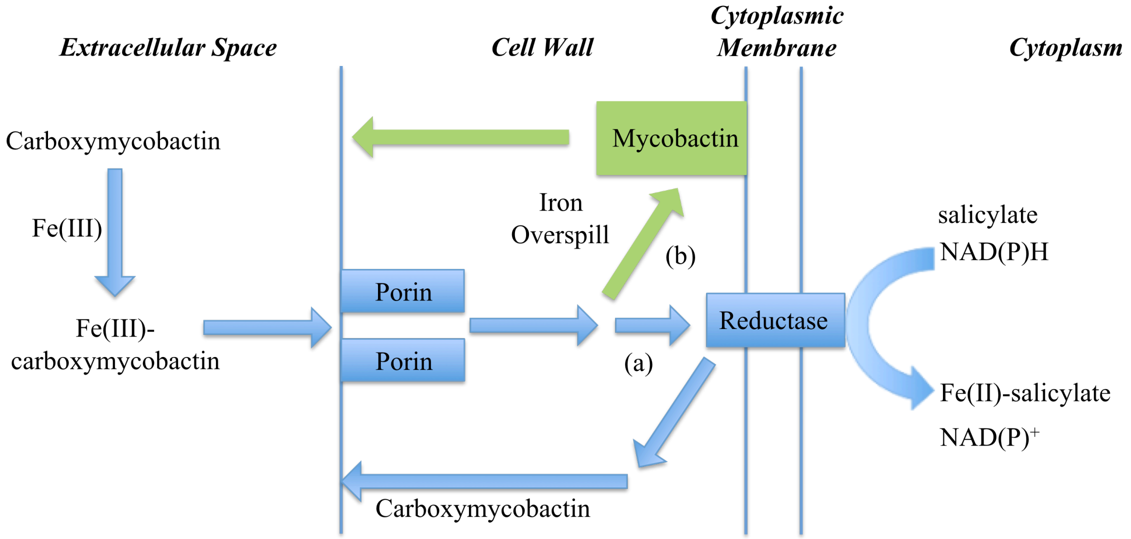

Figure 4.5 Proposed mechanism for Fe(III)-carboxymycobactin uptake into bacteria. Carboxymycobactin acquires iron from extracellular sources. It is introduced into the cellular envelope by facilitated diffusion involving a porin. (a) The porin directly funnels Fe(III)-carboxymycobactin to a reductase, where iron is reduced and possibily picked up by salycilate. The apo-carboxymycobactin then returns to the extracellular space. (b) Alternatively, Fe(III)-carboxymycobactin can interact with mycobactin at the membrane and unload its iron for storage. Adapted from Ratledge, C. *Tuberculosis* 2004, *84*, 110.

Both mechanisms involve the ultimate release of iron from mycobactin by a ferric mycobactin reductase, in which the ferric iron is reduced in the presence of NAD(P)H to ferrous iron. Since mycobactin has a low affinity for ferrous iron, the iron is picked up by a low molecular weight chelator, possibly salicylate [18].

Pathogenic bacteria depend on iron acquisition from their host via siderophores for survival, propagation, and therefore the initiation of a microbial infection [18]. Thus, supramolecular assemblies involving siderophores are currently being investigated in treating these infections, as bacterial siderophores can be used as a means of drug delivery by coupling to a known bacterial inhibitor, such as an antibiotic [107]. Once iron is encountered, this siderophore-drug assembly could theoretically be recognized by ferri-siderophore receptors and transported into the microbial cell, thereby enabling the inhibitor to effectively kill the cell. Siderophore-inhibitor conjugates have recently been developed using this approach, with artemisinin, a peroxide-containing antimalarial compound, as the inhibitor (Figure 4.6) [108].

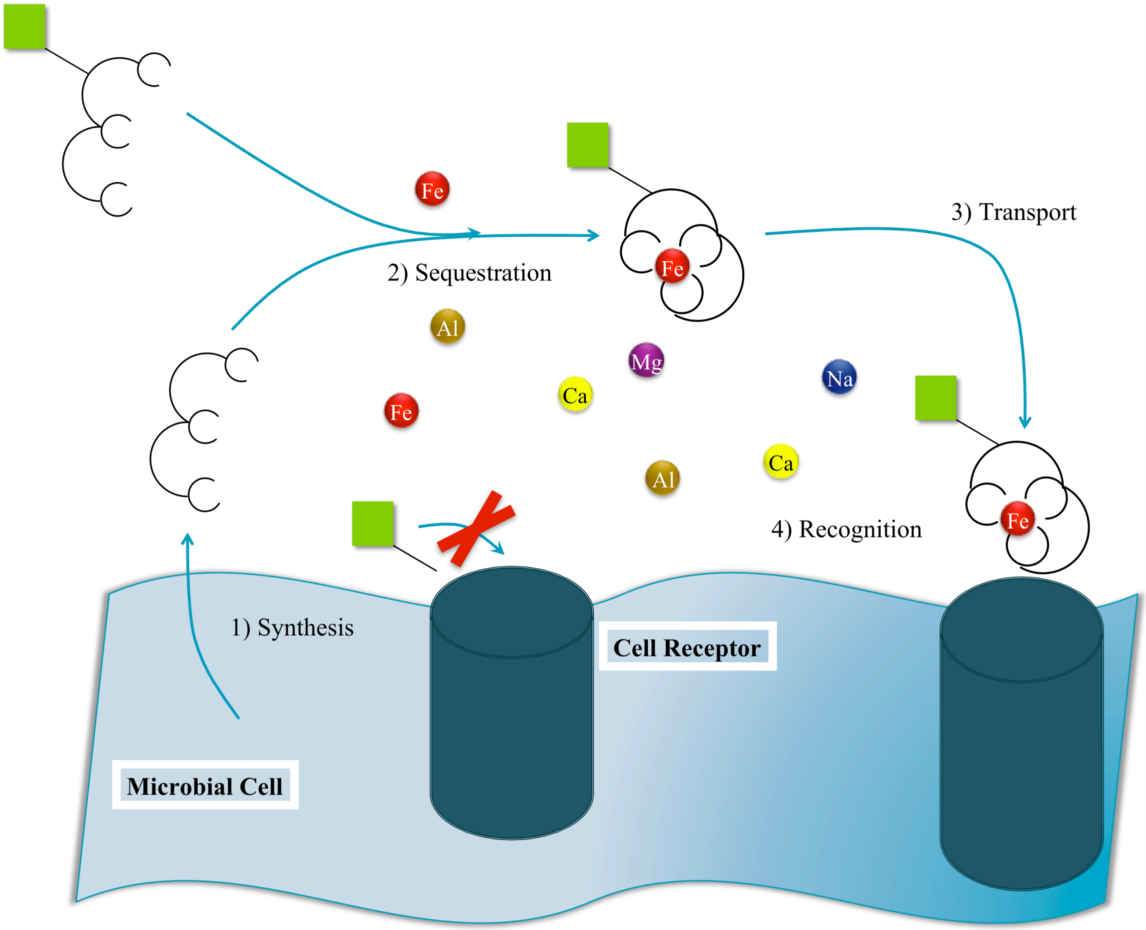

Figure 4.6 Trojan horse approach to drug delivery in a microbial cell. Under iron deficient conditions, a microbe will (1) synthesize low molecular weight, iron-specific chelators called siderophores. The siderophore is released into the environment where it (2) specifically seeks and binds iron forming a stable Fe-siderophore complex. This Fe-siderophore complex is then (3) transported back to a microbial cell where it is (4) recognized at the cell surface. Iron is then transported into the cell where it is released for use in intracellular processes. Drugs are not recognized at the cell surface and are prevented from entering the microbial cell. The Trojan horse approach takes advantage of the natural Fe uptake mechanism, where the drug (green square) is covalently linked to the siderophore, following the pathway described above.

Artemisinin (also called qinghaosu) is a natural peroxide-containing sesquiterpene based on 1,2,4-trioxane and is a remarkably potent and relatively non-toxic antimalarial agent, Figure 4.7a [109,110].

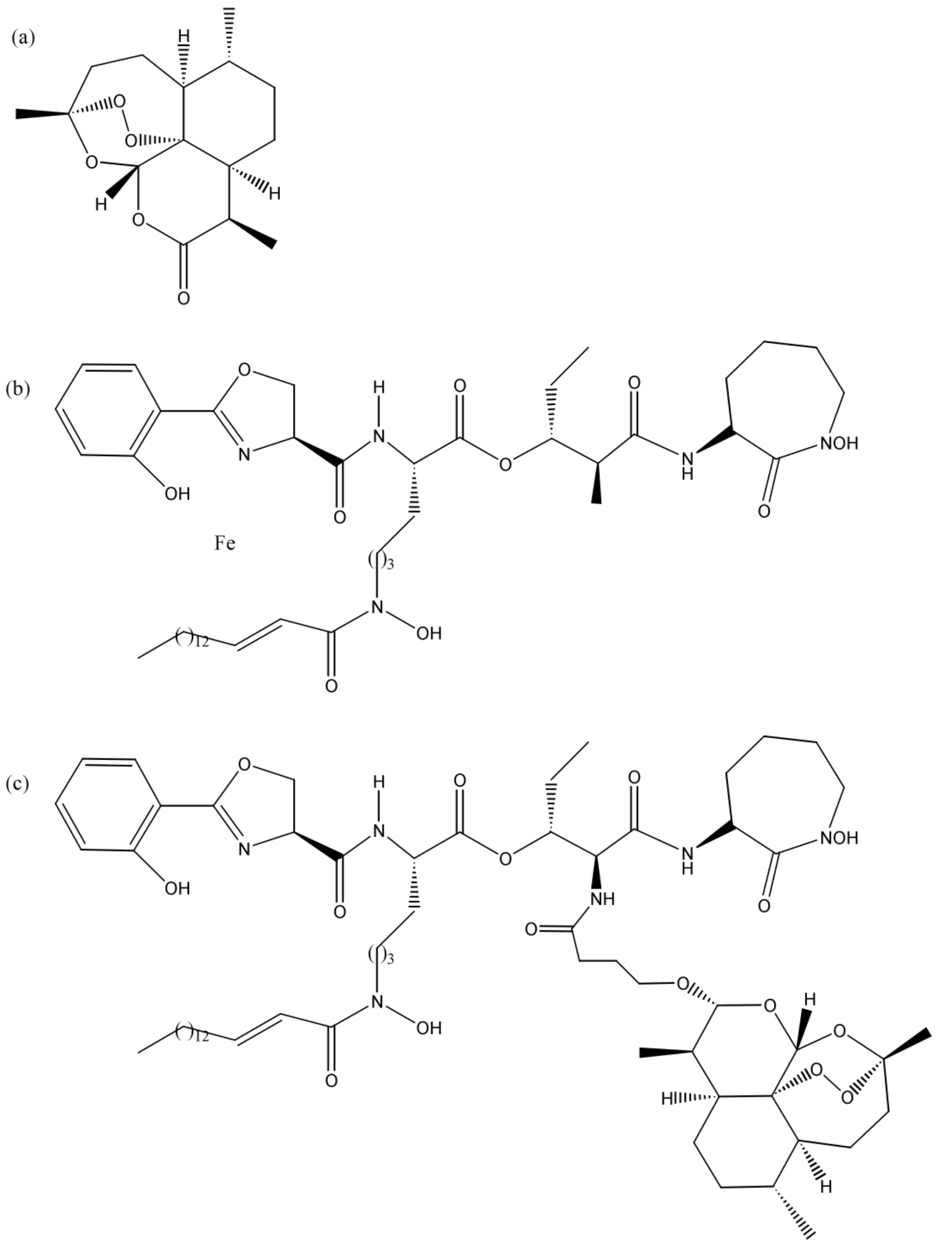

Figure 4.7 Structures of (a) artemisinin, (b) mycobactin, and (c) the mycobactin• artemisinin conjugate.

Ferrous iron [in the form of heme or iron(II) salts] has been proposed to trigger the reductive cleavage of the peroxide bond in artemisinin to form oxygen-centered radicals [110]. The nature of this reaction is still open to speculation. However, it is believed that the addition of an electron to the peroxidic bridge leads to an immediate cleavage of the bond. The oxy radicals produced react rapidly intramolecularly. Two rearrangements are thought to possibly occur, Figure 4.8. In route 1, a 1,5-H shift from position 4 occurs if the radical is located on oxygen 1. This leads to the formation of a secondary carbon radical of the type R_1R_2•CH. Route 2 results in the ß-cleavage of C_3-C_4 for the oxy radical in position 2. This leads to the formation of a primary radical of the type R•CH_2 in position 4 [111]. Such oxy radicals then form carbon-centered radicals that have been found to lead to the death of malaria parasites, a finding that has led to the design of new antimalarial peroxides [112]. It has also been demonstrated that iron released from transferrin can react with artemisinin bound to a transferrin-receptor targeting peptide to generate free radicals that can kill cells [113].

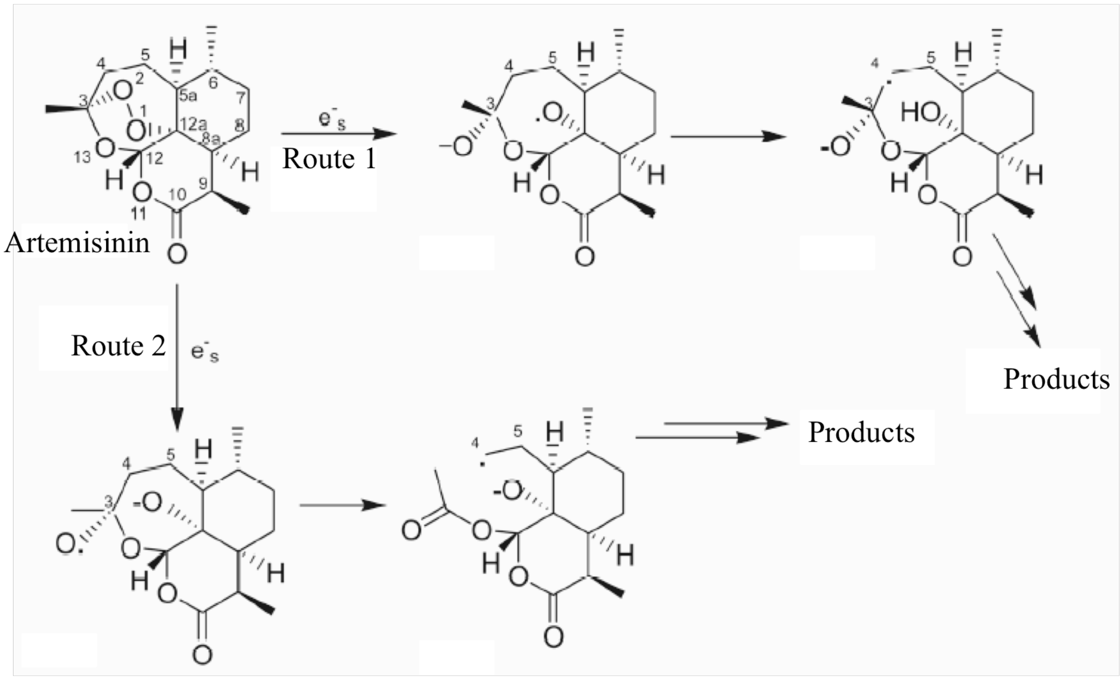

Figure 4.8 Proposed mechanism of action of artemisin via reduction of the peroxo bridge to form oxygen-centered radicals. Adapted from Fuochi, P. G.; Marconi, G.; Mulazzani, Q. G. *Int. J. Radiat. Biol.* 2005, *81*, 319.

Biological studies have demonstrated that artemisinin shows no anti-tuberculosis activity alone; however, when coupled with mycobactin (Figure 4.7b), the resulting conjugate (Figure 4.7c) shows significant anti-tuberculosis activity towards *Mycobacterium tuberculosis* [108]. This activity might be due to Fenton-like redox chemistry induced by Fe(III) reduction within the mycobactin-artemisinin conjugate.

4.2 Statement of Objectives

This chapter examines the efficacy of this Trojan horse approach in which artemisinin is brought into the cell via the natural mycobactin uptake mechanism. We propose that iron reduction in mycobactin initiates the reduction of the peroxo group of artemisinin, which culminates in the formation of hydroxyl radicals. Here we present electrochemical studies of artemisinin, mycobactin, and the mycobactin•artemisinin conjugate in an effort to understand the mechanism of action of the drug conjugate, and its relationship to redox chemistry. These electrochemical results will be related to bioactivity results made available through the Miller laboratory at the University of Notre Dame.

4.3 Experimental

4.3.1 Materials

H_4DFB^+ was purchased from Sigma-Aldrich. $FeHDFB^+$ was prepared as previously described using $FeCl_3$ (Sigma) in aqueous solution or alternatively in 50:50 MeOH: H_2O [114]. KCl and $NaClO_4$ (Fisher) stock solutions were prepared in water and 95% EtOH, respectively. Artemisinin, substituted artemisinin, mycobactin J and the mycobactin•artemisinin conjugate were provided by the Miller Lab at Notre Dame. Mycobactin J was used as the commercially available mycobactin control. The mycobactin component in the conjugate is an analog of mycobactin T. Each compound was provided pure as confirmed by IR, ^{1}H NMR, ^{13}C NMR, and High Resolution Fast Atom Bombardment Mass Spectrometry (HRFAB-MS). The conjugate was loaded using $FeCl_3$ in 95% EtOH. Artemisinin (Aldrich, 98%) solutions were prepared in a 50:50 methanol:water solution or 95% EtOH, depending on the experiment.

4.3.2 Methods

4.3.2.1 Spectrophotometric Measurements

UV-visible spectra were recorded using a Varian Cary 100 or Cary 50 spectrophotometer. The mycobactin•artemisinin conjugate was loaded with $FeCl_3$ (0.25 mM) in 95% EtOH to produce a characteristic peak at 474 nm. Fe-Mycobactin was monitored at 457 nm. Samples were allowed to equilibrate for 10 minutes before spectra were recorded.

4.3.2.2 Cyclic Voltammetry (CV) Measurements

Cyclic voltammetry measurements were made using a Cypress Systems Potentiostat and Model CS-1087 Computer-Controlled Electroanalytical system. A three-electrode setup was used: Pt wire auxiliary electrode, glassy carbon working electrode, and Ag/AgCl reference electrode. Further studies were conducted using a BAS instruments controlled growth Hg drop electrode as the working electrode with an approximate Hg drop area of 16×10^{-3} cm^2 and a mass of 2.63 g/drop. A new drop was used for each experimental trial. For the initial studies involving $FeHDFB^+$ and artemisinin, solutions were prepared in MeOH and 50:50 MeOH:H_2O. For later studies involving mycobactin, artemisinin, and the conjugate, solutions were prepared in 95% EtOH. All solutions were degassed with nitrogen before each experiment was conducted. All potentials, including those corresponding to the cathodic peak potential (E_{cp}) and anodic peak potential (E_{ap}), are reported with respect to NHE.

$FeHDFB^+$ was used as a calibrant in all experiments and its redox potential was measured in between each of the mycobactin and artemisinin measurements samples measured. For measurements made with the Hg-drop working electrode, the reduction potential of $FeHDFB^+$ was found to be -483 mV vs NHE, whereas for measurements made using a glassy carbon working electrode, the value was found to be -478 mV vs NHE. The literature value is -477 mV vs NHE using a glassy carbon or Au button working electrode [30].

4.4 Results and Discussion

4.4.1 Cyclic Voltammetry Studies of the Ferrioxamine B and Artemisinin System as a Model for the Mycobactin•Artemisinin Conjugate System

As a model for the mycobactin•artemisinin conjugate, and in order to test our technique and working hypothesis, we chose to use a solution combination of $FeHDFB^+$ (Figure 4.9) and artemisinin (Figures 4.7a). $FeHDFB^+$ is a siderophore whose redox behavior has been well characterized in the literature [115]. It can provide an indication of how the Fe-mycobactin will affect the redox chemistry of artemisinin. These experiments were performed in preparation for an investigation of the mycobactin•artemisinin conjugate.

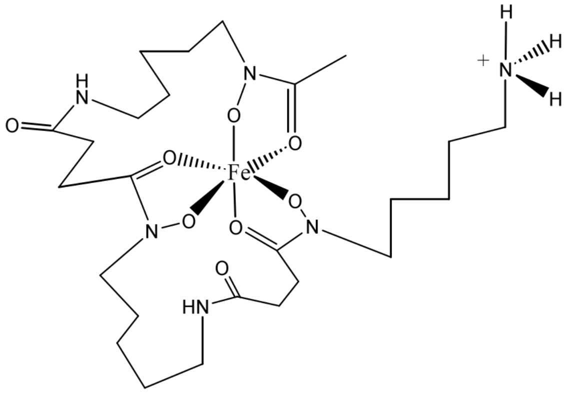

Figure 4.9 Structure of FeHDFB$^+$. Reprinted from Figure 2.1 for reader convenience.

Figure 4.10 shows an irreversible cyclic voltammogram for artemisinin that is consistent with that reported in the literature [109,116]. The reductive peak is not coupled with a re-oxidation peak, consistent with electrochemically driven reduction followed by a chemical process with a different corresponding oxidation wave, Equation 4.1.

$$\begin{tikzcd} \mathrm{art}_O \arrow[r, "+\ e^-"] & \mathrm{art}_R \arrow[l, bend left, "\times"] \end{tikzcd} \tag{4.1}$$

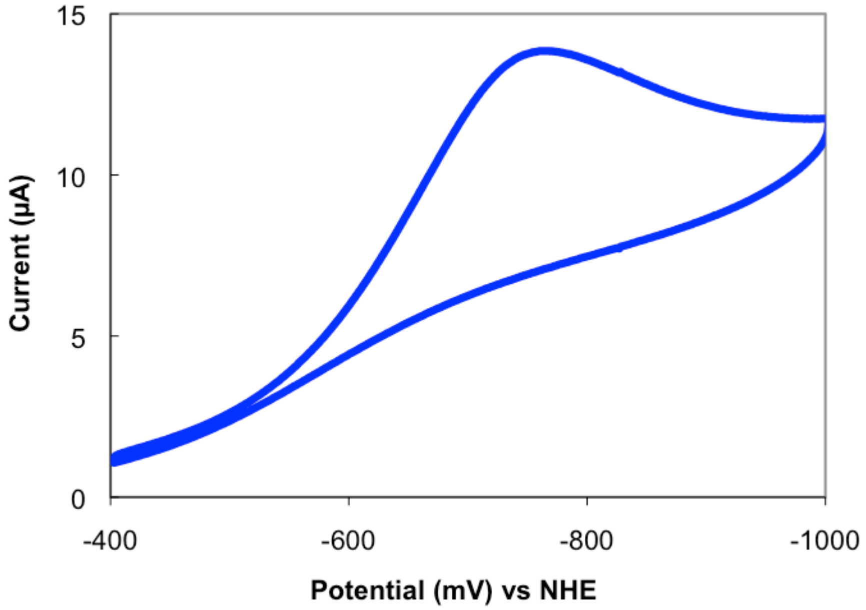

Figure 4.10 Cyclic voltammogram of artemisinin. Conditions: [artemisinin] = 4.2 mM, E_{cp} = -760 mV vs. NHE, glassy carbon working electrode, Pt wire auxiliary electrode, Ag/AgCl reference electrode, scan rate = 10 mV/s, [KCl] = 500 mM as background electrolyte, MeOH/H_2O (1:1).

Figure 4.11A shows a reversible cyclic voltammogram for $FeHDFB^+$, with clearly visible reduction and oxidation peaks. Reversibility is indicated by the ratio i_{red}/i_{ox} ~1, where i_{red} refers to the current at the cathodic peak potential and i_{ox} refers to the current at the anodic peak potential with respect to a non-zero baseline, as shown in Figure 4.11B. The results shown in Figure 4.11 are well characterized and consistent with previously published results for $FeHDFB^+$ [115].

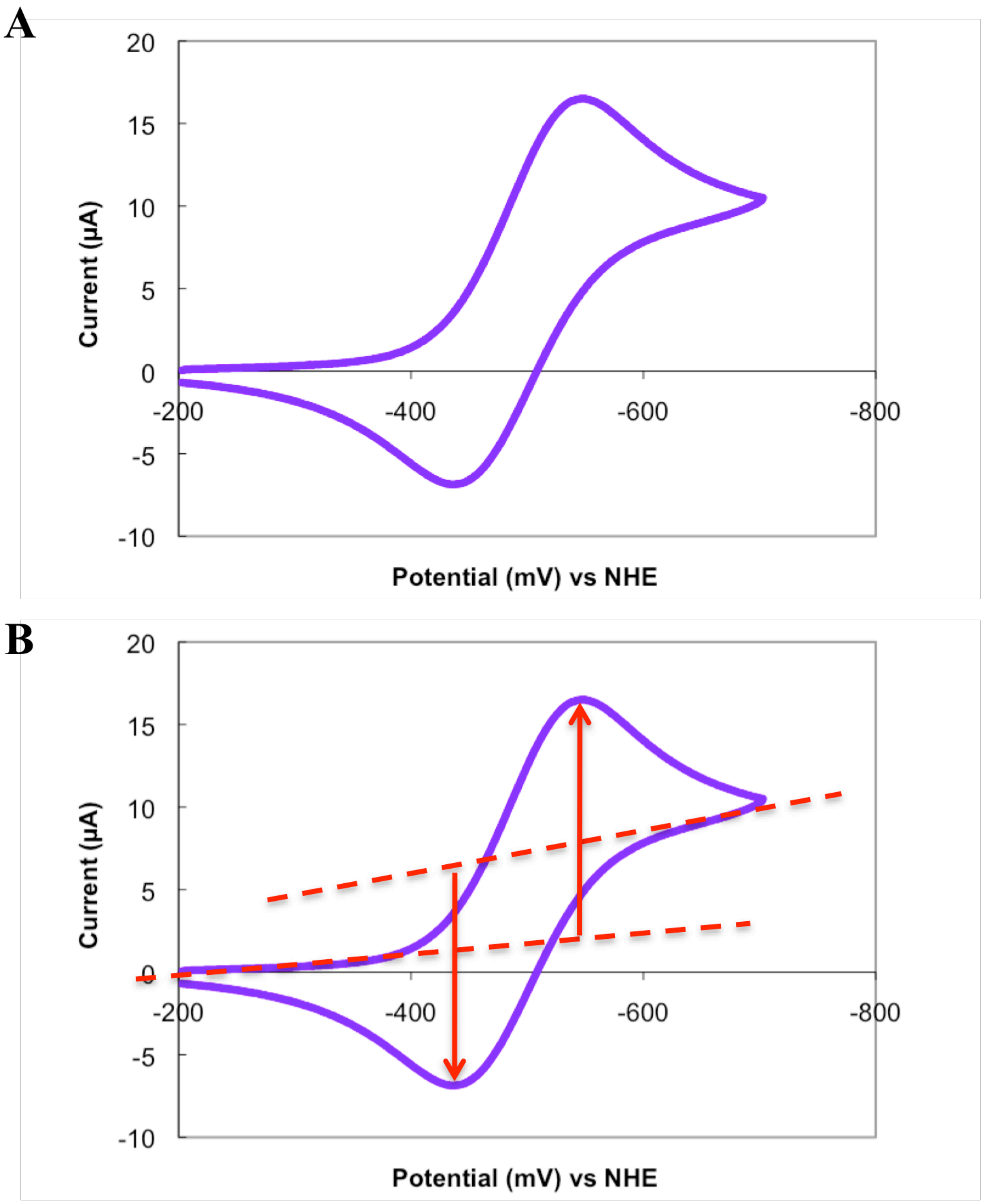

Figure 4.11 A. Cyclic Voltammogram of FeHDFB$^+$. B. Illustration of the calculation of i_{red}/i_{ox} ratio for the cyclic voltammogram of FeHDFB$^+$. Conditions: [FeHDFB$^+$] = 5 mM, $E_{1/2}$ = -492 mV vs. NHE, i_{red}/i_{ox} ~1, peak-to-peak separation ~ 100 mV, glassy carbon working electrode, Pt wire auxiliary electrode, Ag/AgCl reference electrode, scan rate = 10 mV/s, [KCl] = 500 mM as background electrolyte, MeOH/H_2O (1:1).

Figure 4.12 shows the cyclic voltammograms for artemisinin and FeHDFB$^+$ mixtures ranging from a 0.1:1 ratio to a 10:1 ratio of FeHDFB$^+$:artemisinin. At low concentrations of FeHDFB$^+$, the voltammograms resemble that of artemisinin (scans v-iv), but as more FeHDFB$^+$ is added, the cathodic peak shifts to more positive values and the voltammogram resembles that of FeHDFB$^+$ (scans iii-i). This behavior is most evident if we examine the voltammogram for the 1:1 mixture (scan iii, Figure 4.13).

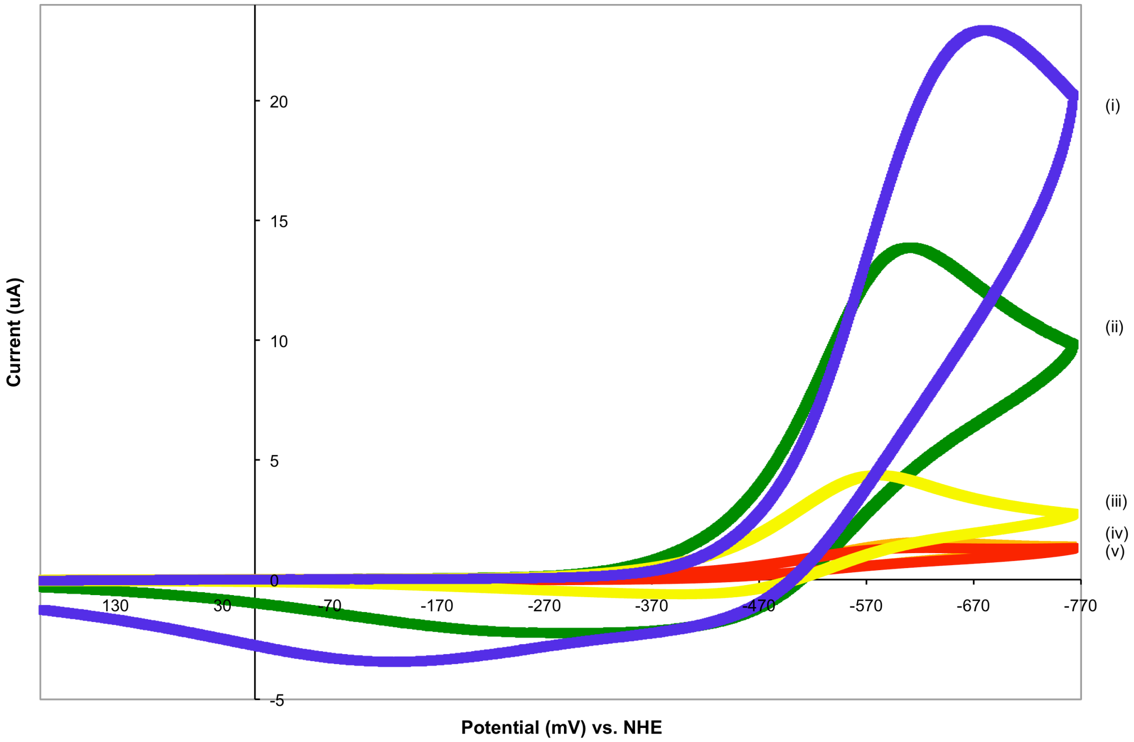

Figure 4.12 Cyclic Voltammogram of FeHDFB$^+$ and Artemisinin mixture. Conditions: [artemisinin] = 1 mM for all solutions, (i) [FeHDFB$^+$] = 10 mM, E_{cp} = -618 mV vs. NHE, (ii) [FeHDFB$^+$] = 5 mM, E_{cp} = -609 mV vs. NHE, (iii) [FeHDFB$^+$] = 1 mM, E_{cp} = -581 mV vs. NHE, (iv) [FeHDFB$^+$] = 0.2 mM, E_{cp} = -608 mV vs. NHE (v) [FeHDFB$^+$] = 0.1 mM, E_{cp} = -678 mV vs. NHE, in MeOH: H_2O, glassy carbon working electrode, Pt wire auxiliary electrode, Ag/AgCl reference electrode, scan rate = 10 mV/s, [KCl] = 500 mM as background electrolyte, MeOH/H_2O (1:1).

Figure 4.13 shows the cyclic voltammogram for a 1:1 mixture of artemisinin and FeHDFB$^+$ (shown previously in scan iii of Figure 4.12). Two observations are of significance here. One is that the observed cyclic voltammogram is essentially that of FeHDFB$^+$ except that it is non-reversible, i.e. $i_{red}/i_{ox} > 1$. The second observation is that the artemisinin signal is no longer present, as indicated by an extended sweep to the point of solvent breakdown (not shown). These observations suggest that the combination of FeHDFB$^+$ and artemisinin result in a chemical interaction between the two, presumably subsequent to reduction of ferri-FeHDFB$^+$ to ferro-FeHDFB$^+$. Furthermore the data suggest that the Fe^{2+} dissociates from the ferro-FeHDFB$^+$ and therefore is not available for re-oxidation to ferri-FeHDFB$^+$.

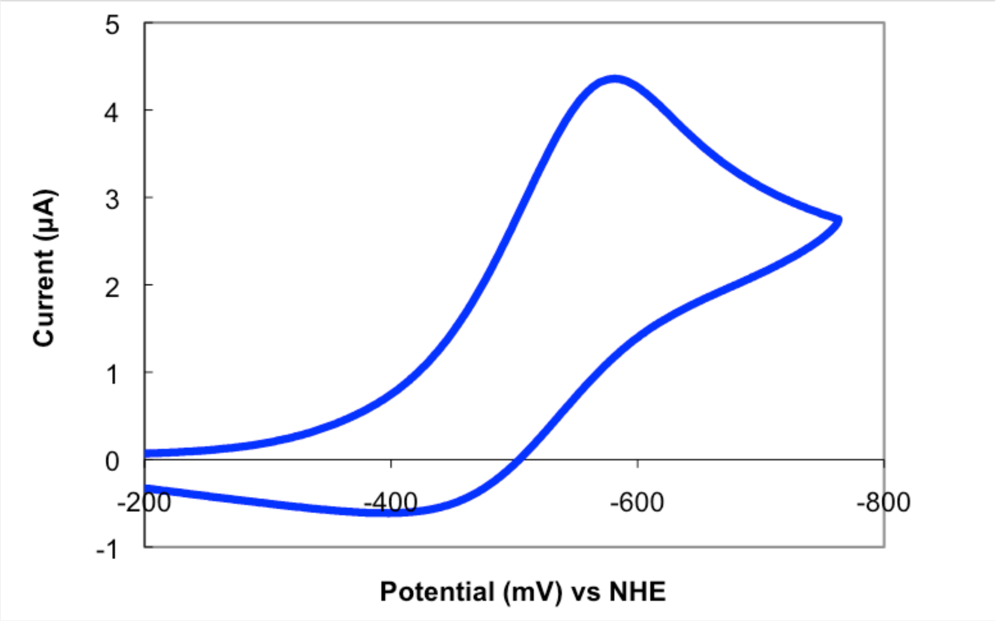

Figure 4.13 Cyclic Voltammogram of a 1:1 FeHDFB$^+$ and Artemisinin mixture. Conditions: [FeHDFB$^+$] = 1 mM, [artemisinin] = 1 mM, Ecp = -581 mV vs. NHE, glassy carbon working electrode, Pt wire auxiliary electrode, Ag/AgCl reference electrode, scan rate = 10 mV/s, [KCl] = 500 mM as background electrolyte, MeOH/H_2O (1:1).

The following EC mechanism[1] is proposed for the system involving a mixture of ferri-FeHDFB$^+$ and artemisinin, where art_O refers to the oxidized form of artemisinin and art_R refers to the reduced form of artemisinin.

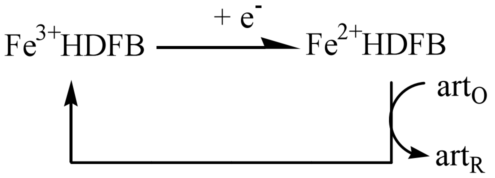

(4.2)

We have evidence for this mechanism for measurements made in that there is an increase in the cathodic peak current per concentration unit for the ferri-FeHDFB$^+$ and artemisinin 1:1 mixture in comparison to that of the individual components. Specifically, the cathodic peak current for ferri-FeHDFB$^+$ alone is approximately 2 μA/mM (Figure 4.11), and that of artemisinin alone is approximately 1.9 μA/mM (Figure 4.10), whereas for the 1:1 mixture of ferri-FeHDFB$^+$ and artemisinin it is approximately 3.5 μA/mM (Figure 4.13).

4.4.2 Cyclic Voltammetry Studies of the Mycobactin•Artemisinin Conjugate System

The structures of artemisinin, mycobactin, and the mycobactin•artemisinin conjugate are shown in Figure 4.7.

Mycobactin and the mycobactin•artemisinin conjugate were loaded with Fe^{3+}, as evidenced by the visible absorption peaks shown in Figure 4.14. The peaks at 457 nm and 474 nm are diagnostic of the metal to ligand charge transfer bands for mycobactin [118] and the mycobactin•artemisinin conjugate, respectively.

---

[1] An EC mechanism is an electrochemical reaction at the electrode in which the electrogenerated species rearranges or reacts with some other solution component. It is also referred to as a *following chemical reaction* as it occurs after the electrode reaction [117].

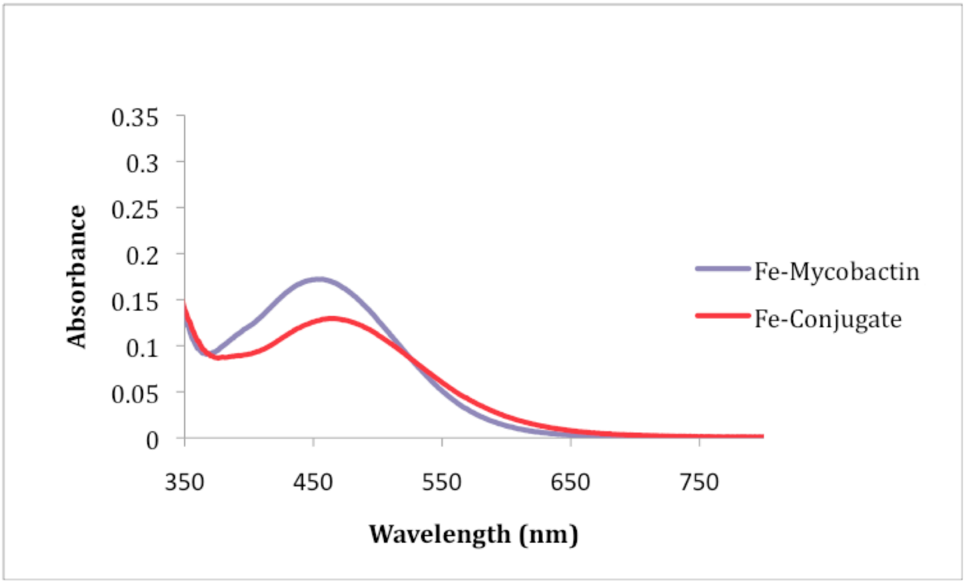

Figure 4.14 UV-Visible Spectra of Fe-loaded Mycobactin, (λ_{max} = 457 nm, in 95% EtOH) and Fe-loaded Mycobactin•Artemisinin Conjugate (λ_{max} = 474 nm, in 95% EtOH). Note: Concentrations not recorded as spectra was used for the qualitative purpose of obtaining the λ_{max}.

Figures 4.15 and 4.16 show cyclic voltammograms for Fe-mycobactin using a glassy carbon electrode and a Hg-drop mercury electrode as the working electrodes, respectively.

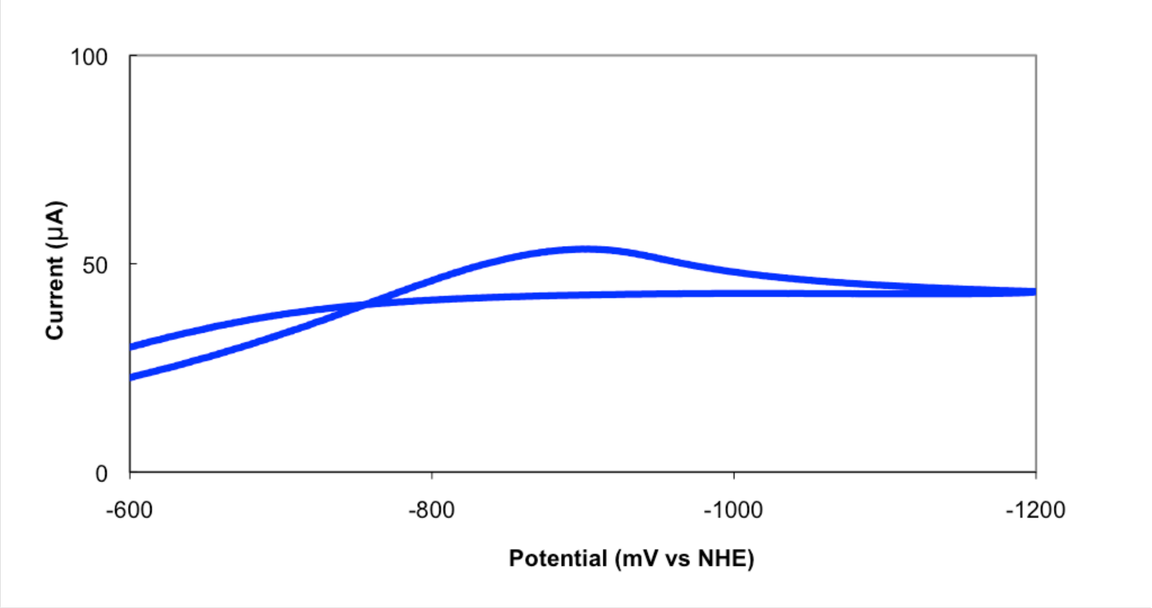

Figure 4.15 Cyclic Voltammogram of Fe-Mycobactin. Conditions: glassy carbon working electrode, Pt wire auxiliary electrode, Ag/AgCl reference electrode, scan rate = 10 mV/s, [Fe-Mycobactin] = 3 mM, [$NaClO_4$] = 100 mM as background electrolyte, solutions in 95% EtOH, , E_{cp} = -899 mV vs. NHE.

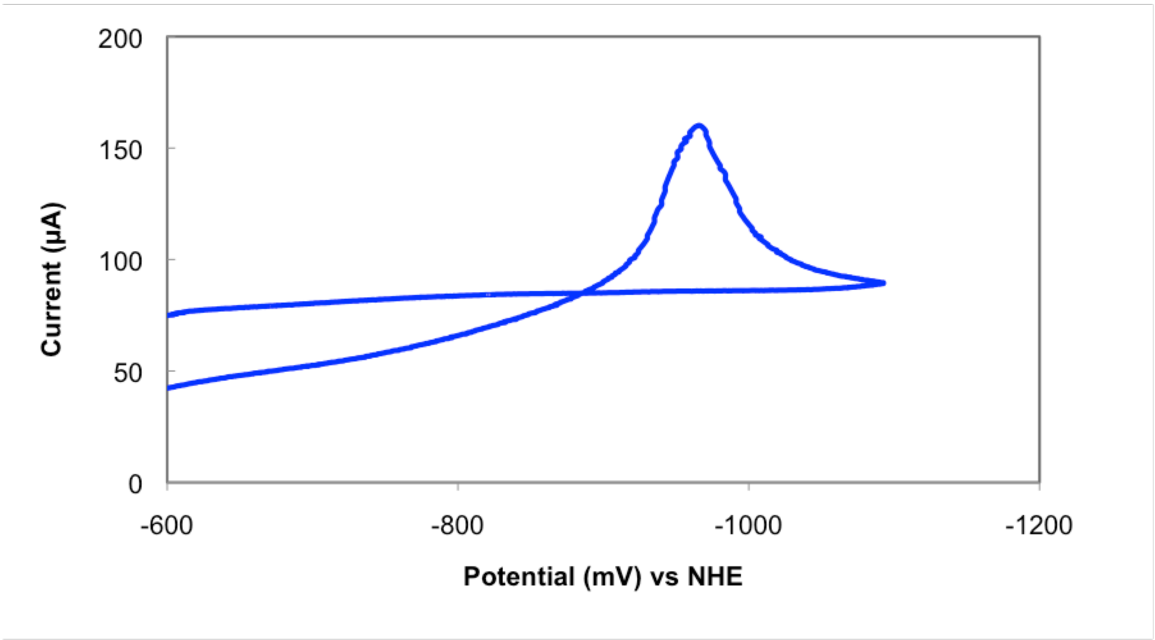

Figure 4.16 Cyclic Voltammogram of Fe-Mycobactin. Conditions: Hg-drop working electrode, Pt wire auxiliary electrode, Ag/AgCl reference electrode, scan rate = 10 mV/s, [Fe-Mycobactin] = 2.61 mM, [$NaClO_4$] = 100 mM as background electrolyte, solutions in 95% EtOH, E_{cp} = -966 mV vs. NHE.

It is important to note that irreversible behavior is observed regardless of the working electrode over a scan rate range of 10 mV/s to 550 mV/s (data not shown). This irreversibility stems from the dissociation of Fe from mycobactin upon its reduction, as shown below, Equation 4.3.

$$\mathrm{Fe^{3+}}\text{-Mycobactin} \underset{-\,e^-}{\overset{+\,e^-}{\rightleftharpoons}} \mathrm{Fe^{2+}}\text{-Mycobactin} \longrightarrow \mathrm{Fe^{2+}} + \text{Mycobactin} \qquad (4.3)$$

Before studying the electrochemical behavior of the Fe-mycobactin•artemisinin conjugate, a mixture of Fe-mycobactin and artemisinin was studied using a glassy carbon electrode as the working electrode, as shown in Figure 4.17. The voltammogram for artemisinin (shown in blue) shows an irreversible behavior that is consistent with that reported in the literature [109]. The voltammogram for Fe-loaded mycobactin (shown in orange) also shows irreversible behavior, as seen in our previous studies. Cyclic voltammetry results for Fe-loaded mycobactin are not available in the literature. Finally, the voltammogram for the mixture of Fe-loaded mycobactin and artemisinin (shown in lavender) shows only one cathodic peak. Although a clear assignment cannot be made as to what the peak corresponds to, it does indicate an interaction between Fe-mycobactin and artemisinin. These studies were repeated using a Hg-drop working electrode, Figure 4.18. Although the potentials are not identical to those observed using the glassy carbon electrode, the general trend in potential between each component remains the same.

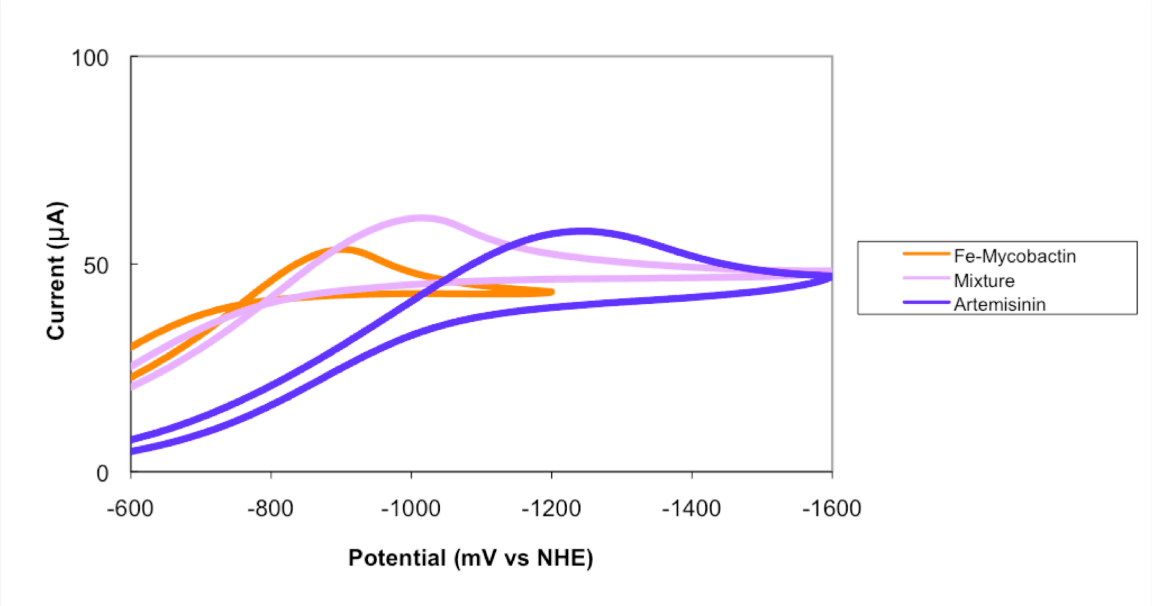

Figure 4.17 Cyclic Voltammogram of Fe-Mycobactin, and Artemisinin. Conditions: glassy carbon working electrode, Pt wire auxiliary electrode, Ag/AgCl reference electrode, scan rate = 10 mV/s, [$NaClO_4$] = 100 mM as background electrolyte, solutions in 95% EtOH. Orange trace: Fe-Mycobactin. Conditions: [Fe-Mycobactin] = 3 mM, E_{cp} = -899 mV vs. NHE. Blue trace: Artemisinin. Conditions: [Artemisinin] = 3 mM, E_{cp} = -1235 mV vs. NHE. Lavender trace: Artemisinin/Fe-Mycobactin 1:1 mixture. Conditions: [Fe-Mycobactin] = 2 mM, [Artemisinin] = 2 mM E_{cp} = -1011 mV vs. NHE.

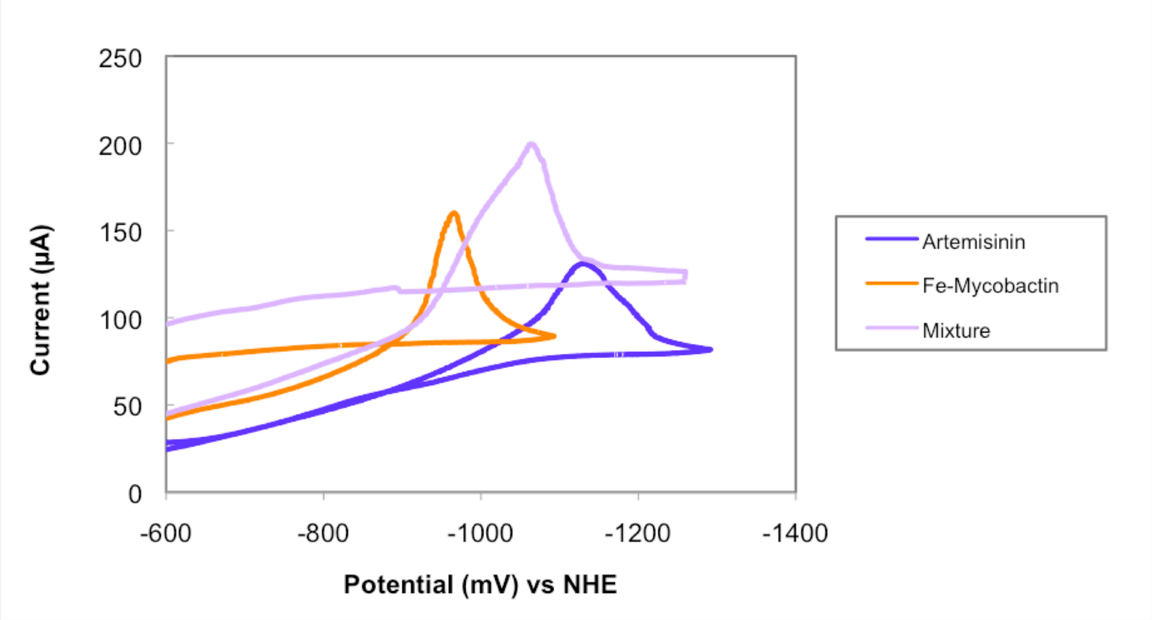

Figure 4.18 Cyclic Voltammogram of Fe-Mycobactin, and Artemisinin. Conditions: Hg-drop working electrode, Pt wire auxiliary electrode, Ag/AgCl reference electrode, scan rate = 10 mV/s, [NaClO$_4$] = 100 mM as background electrolyte, solutions in 95% EtOH. Orange trace: Fe-Mycobactin. Conditions: [Fe-Mycobactin] = 2.61 mM, E_{cp} = -966 mV vs. NHE. Blue trace: Artemisinin. Conditions: [Artemisinin] = 3 mM, E_{cp} = -1130 mV vs. NHE. Lavender trace: Artemisinin/Fe-Mycobactin 1:1 mixture. Conditions: [Fe-Mycobactin] = 1.25 mM, [Artemisinin] = 1.25 mM, E_{cp} = -1063 mV vs. NHE.

The results shown above (Figures 4.17 and 4.18) suggest that there is an interaction between Fe-mycobactin and artemisinin. The following EC mechanism is proposed for the system involving a 1:1 mixture of mycobactin and artemisinin:

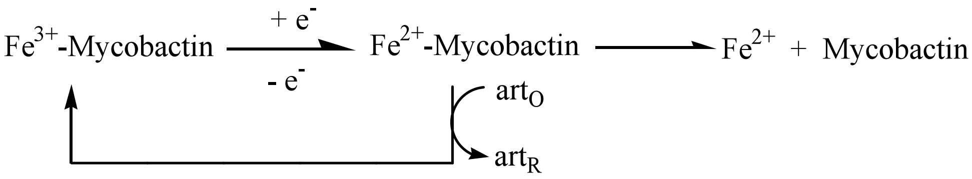

(4.4)

As was the case for the FeHDFB$^+$ and artemisinin 1:1 mixture, we have evidence for this mechanism for measurements made with the glassy carbon working electrode

(Figure 4.17) in that there is an increase in the cathodic peak current per concentration unit for the mycobactin and artemisinin mixture in comparison to that of the individual components. Specifically, the peak current for Fe-mycobactin alone is approximately 4.3 μA/mM, whereas for the 1:1 mixture of Fe-mycobactin and artemisinin it is approximately 6 μA/mM (Figure 4.17). The same behavior is observed in measurements made with the Hg-drop working electrode with a similar increase occuring in the cathodic peak current per concentration unit for the 1:1 mycobactin and artemisinin mixture in comparison to that of the individual components. Specifically, the peak current for Fe-mycobactin is approximately 26.4 μA/mM, whereas for 1:1 the mixture of Fe-mycobactin and artemisinin it is approximately 61.6 μA/mM (Figure 4.18). This evidence indicates that, regardless of the working electrode, upon addition of artemisinin there is increased current output due to an interaction between the Fe^2-mycobactin and the artemisinin (Equation 4.4).

Figures 4.19 and 4.20 show the voltammograms for artemisinin, Fe-loaded mycobactin, and the artemisinin•Fe-loaded mycobactin conjugate obtained using the glassy carbon working electrode. The voltammogram for artemisinin (shown in blue) shows an irreversible behavior that is consistent with that reported in the literature [109,116]. As seen in our studies with the $FeHDFB^+$ / artemisinin mixture model system (Figures 4.11-4.13), the reductive peak for artemisinin is not coupled with a re-oxidation peak, consistent with electrochemically driven reduction followed by a chemical process with a different corresponding oxidation wave. The voltammogram for Fe-loaded mycobactin (shown in orange) also shows irreversible behavior. Finally, the voltammogram for the Fe-mycobactin•artemisinin conjugate shows slightly different behavior in Figures 4.19 and 4.20. Both fall at similar potentials, however, the voltammogram presented in Figure 4.20 (shown in lavender) shows a shoulder corresponding to the reduction of mycobactin, followed by the subsequent reduction of artemisinin. It is significant to note here that the second cathodic peak, that corresponding to artemisinin within the conjugate, occurs essentially at the same reduction potential as that of artemisinin by itself, and that the first cathodic peak, that corresponding to ferri-mycobactin is slightly shifted to a lower reduction potential, presumably because of its interaction with artemisinin within the conjugate.

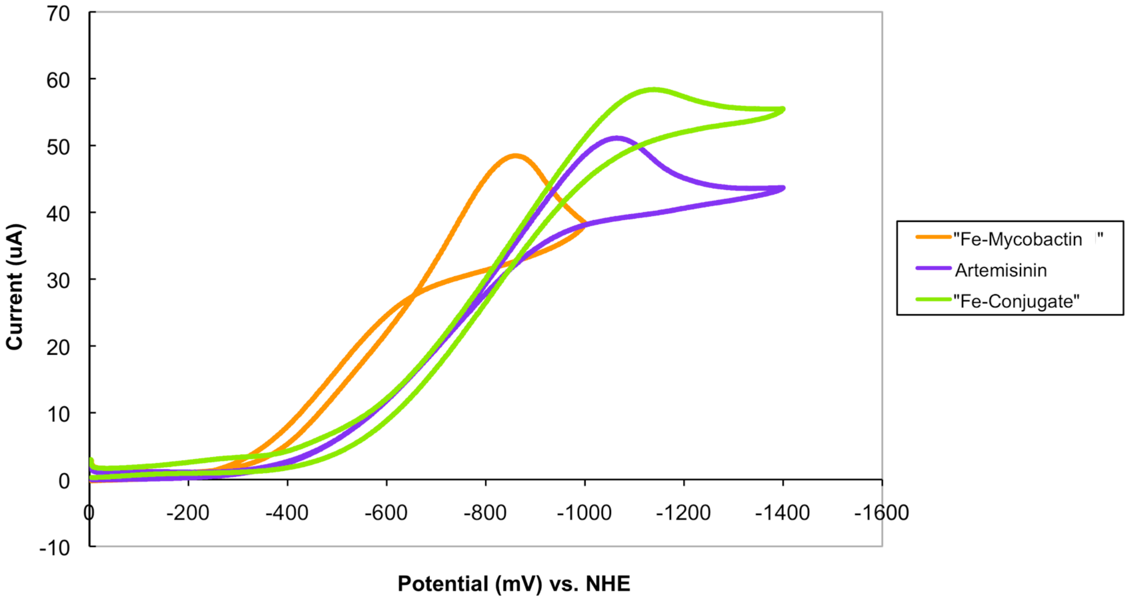

Figure 4.19 Cyclic Voltammograms of Fe-loaded Mycobactin, Artemisinin, and Fe-loaded Mycobactin•Artemisinin Conjugate. Conditions: glassy carbon working electrode, Pt wire auxiliary electrode, Ag/AgCl reference electrode, scan rate = 10 mV/s, [NaClO4] = 100 mM as background electrolyte, solutions in EtOH. (a) Mycobactin (shown in orange). Conditions: [Mycobactin] = 3mM, E_{cp}= -856 mV vs. NHE (b) Artemisinin (shown in blue). Conditions: [Artemisinin] = 3mM, E_{cp} = -1063 mV vs. NHE (c) Artemisinin•Mycobactin conjugate (shown in green). Conditions: [Conjugate] = 1.625 mM, E_{cp}= -1139 mV vs. NHE.

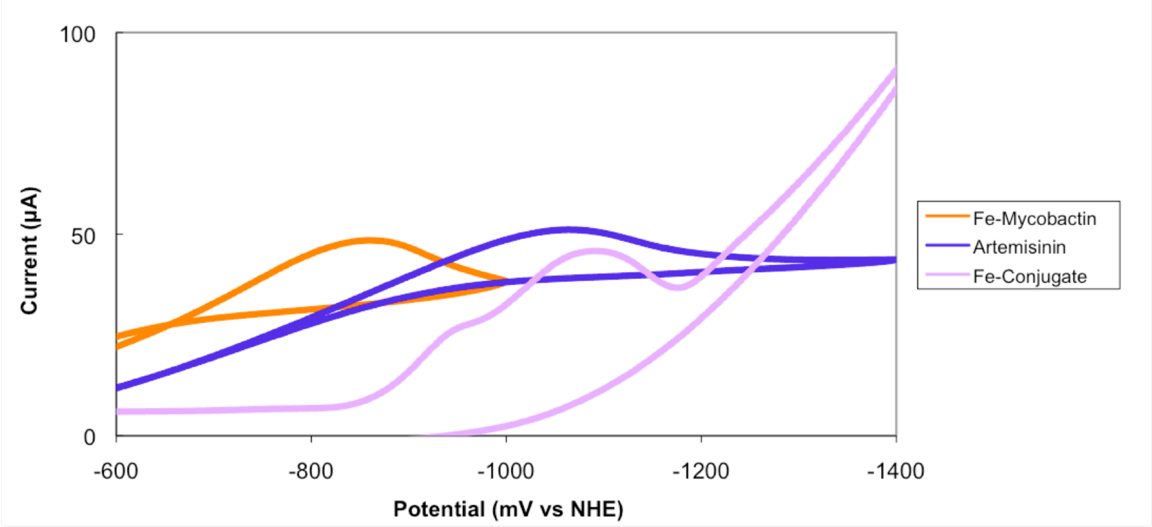

Figure 4.20 Cyclic Voltammograms of Fe-loaded Mycobactin, Artemisinin, and Fe-loaded Mycobactin•Artemisinin Conjugate. Conditions: glassy carbon working electrode, Pt wire auxiliary electrode, Ag/AgCl reference electrode, scan rate = 10 mV/s, [$NaClO_4$] = 100 mM as background electrolyte, solutions in 95% EtOH. Orange trace: Fe-Mycobactin. Conditions: [Fe-Mycobactin] = 3 mM, E_{cp} = -856 mV vs. NHE. Blue trace: Artemisinin. Conditions: [Artemisinin] = 3mM, E_{cp} = -1063 mV vs. NHE. Lavender trace: Fe-Mycobactin•Artemisinin Conjugate. Conditions: [Conjugate] = 1.625 mM, E_{cp} = -955 mV vs. NHE, E_{cp} = -1090 mV vs. NHE.

Similar behavior is seen in measurements made with the Hg-drop working electrode, Figure 4.21. Both artemisinin (shown in blue) and Fe-mycobactin (shown in orange) show irreversible behavior and the voltammogram for the Fe-mycobactin •artemisinin conjugate (shown in lavender) again shows a shoulder corresponding to the reduction of mycobactin, followed by the subsequent reduction of artemisinin. In general, measurements taken using the Hg-drop working electrode are shifted to more negative potentials than those with the glassy carbon electrode, presumably due to an increase in over potential.

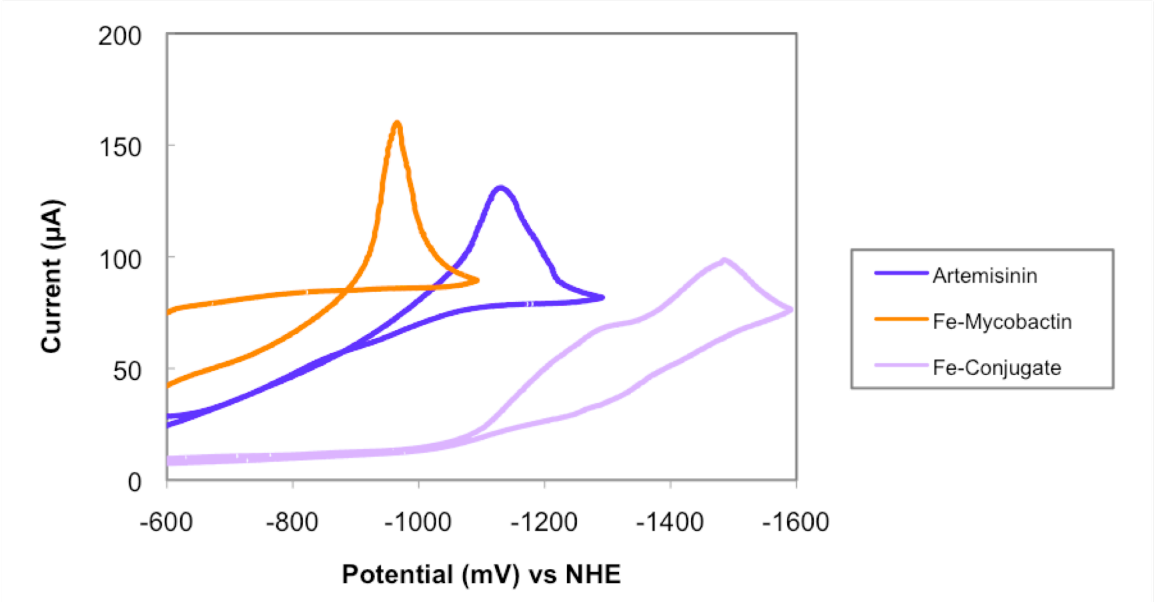

Figure 4.21 Cyclic Voltammograms of Fe-loaded Mycobactin, Artemisinin, and Fe-loaded Mycobactin•Artemisinin Conjugate. Conditions: Hg-drop working electrode, Pt wire auxiliary electrode, Ag/AgCl reference electrode, scan rate = 10 mV/s, [$NaClO_4$] = 100 mM as background electrolyte, solutions in 95% EtOH. Orange trace: Fe-Mycobactin. Conditions: [Fe-Mycobactin] = 2.61 mM, Ecp = -966 mV vs. NHE. Blue trace: Artemisinin. Conditions: [Artemisinin] = 3 mM, Ecp = -1130 mV vs. NHE. Lavender trace: Fe-Mycobactin•Artemisinin Conjugate. Conditions: [Conjugate] = 2.46 mM, Ecp = -1270 mV vs. NHE, Ecp = -1476 mV vs. NHE.

It is clear from these results that the combination of Fe-loaded mycobactin and artemisinin within the conjugate results in a chemical interaction between the two, as hypothesized from results obtained from the $FeHDFB^+$/artemisinin mixture. This interaction appears to occur subsequent to the reduction of ferri-mycobactin to ferro-mycobactin, as was the case in our model system. An EC mechanism is proposed in Equation 4.6.

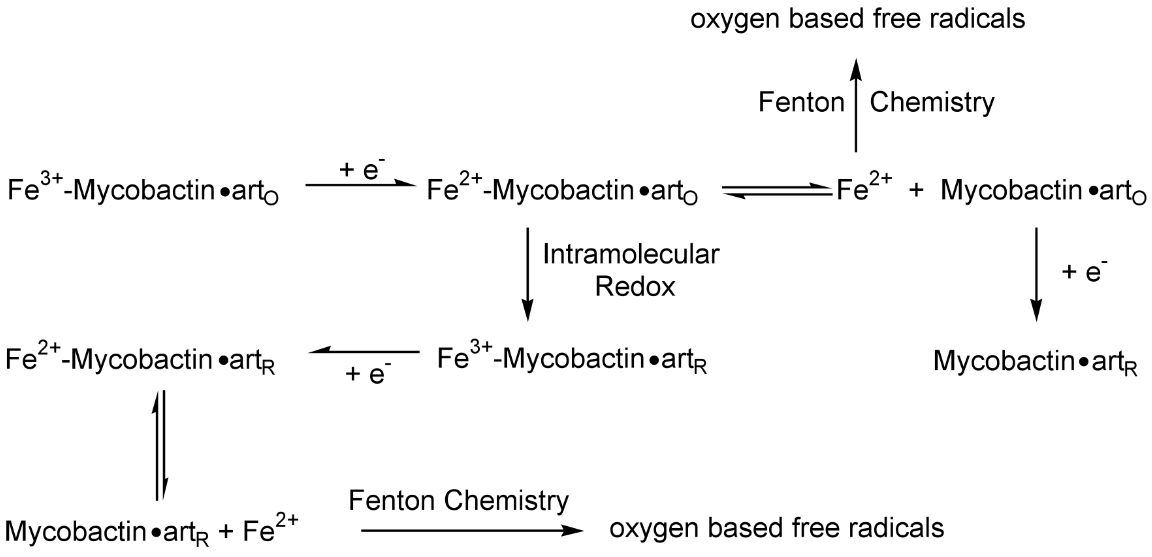

(4.6)

We have evidence for this mechanism for measurements taken using the glassy carbon working electrode (Figure 4.20) in that there is an increase in the cathodic peak current per concentration unit for the Fe-mycobactin•artemisinin conjugate in comparison to that of the individual components. Specifically, the peak current for Fe-mycobactin is approximately 7 μA/mM, whereas for the Fe-mycobactin•artemisinin conjugate it is approximately 18 μA/mM for the shoulder and 19 μA/mM for the main peak. This indicates that upon addition of artemisinin there is increased current output due to an intramolecular electron transfer between the Fe^{2+}-mycobactin and the artemisinin components. This increase in cathodic peak current per concentration of the conjugate with respect to the individual components was not observed in the measurements made with the Hg-drop working electrode. However, the general trend in the order of the reduction potentials, and the shapes of the curves were reproducible in comparison.

4.5 Summary and Conclusions

4.5.1 Cyclic Voltammetry Studies of the Ferrioxamine B and Artemisinin System as a Model for the Mycobactin•Artemisinin Conjugate System

The results obtained suggest that ferro-$FeHDFB^+$ interacts with artemisinin through a process that re-oxidizes Fe^{2+} in the reduced $FeHDFB^+$. We have evidence for this mechanism in that the anodic return wave for $FeHDFB^+$ is missing, as shown in Figure 4.13. This tells us that the ferro-$FeHDFB^+$is not available for re-oxidation, and thus must be engaged elsewhere. Additionally, there is an increase in the cathodic peak current per concentration unit for the 1:1 $FeHDFB^+$and artemisinin mixture (Figures 4.13) in comparison to that of the individual components (Figures 4.11-4.12). Specifically, the peak current is approximately 2 μA/mM for $FeHDFB^+$ alone, whereas for the mixture of $FeHDFB^+$ and artemisinin it is approximately 3.5 μA/mM. This supports the cyclic process illustrated in Equation 4.2.

4.5.2 Cyclic Voltammetry Studies of the Mycobactin•Artemisinin Conjugate System

The results obtained suggest that there is an interaction between Fe-mycobactin and artemisinin in the system involving the mycobactin•artemisinin conjugate. We have evidence for this mechanism for measurements taken using the glassy carbon working electrode (Figure 4.20) in that there is an increase in the cathodic peak current per concentration unit for the Fe-mycobactin•artemisinin conjugate in comparison to that of the individual components. Specifically, the peak current for Fe-mycobactin is approximately 7 μA/mM, whereas for the Fe-mycobactin•artemisinin conjugate it is approximately 18 μA/mM for the shoulder and 19 μA/mM for the main peak. This indicates that upon addition of artemisinin there is increased current output due to an intramolecular electron transfer between the Fe^{2+}-mycobactin and the artemisinin components. This supports the cyclic process illustrated in Equation 4.6.

4.5.3 Potential Therapeutic Value of the Artemisinin• Mycobactin Trojan Horse Approach

Although the antimalarial agent artemisinin itself is not active against tuberculosis, biological studies show that conjugation to a mycobacterial siderophore induces significant and selective anti-TB activity, while retaining an antimalarial activity similar to that of artemisinin itself [108].

Voltammetric studies suggest that reduction of the bound ferric iron to its ferrous form induces Fenton-like chemistry from the interaction of the ferrous iron with the peroxide linkage of the artemisinin leading to the reduction and cleavage of the peroxo-bridge, consistent with our hypothesis. This correlates with the biological activity observed for this complex, since this latter reduction would generate free radicals that would be expected to cause intracellular damage. The proposed coupled electrochemical/chemical processes (Equation 4.6) is consistent with our observations and indicates that we can produce an effective Trojan horse drug using Fe-mycobactin as a recognition factor, Figure 4.22.

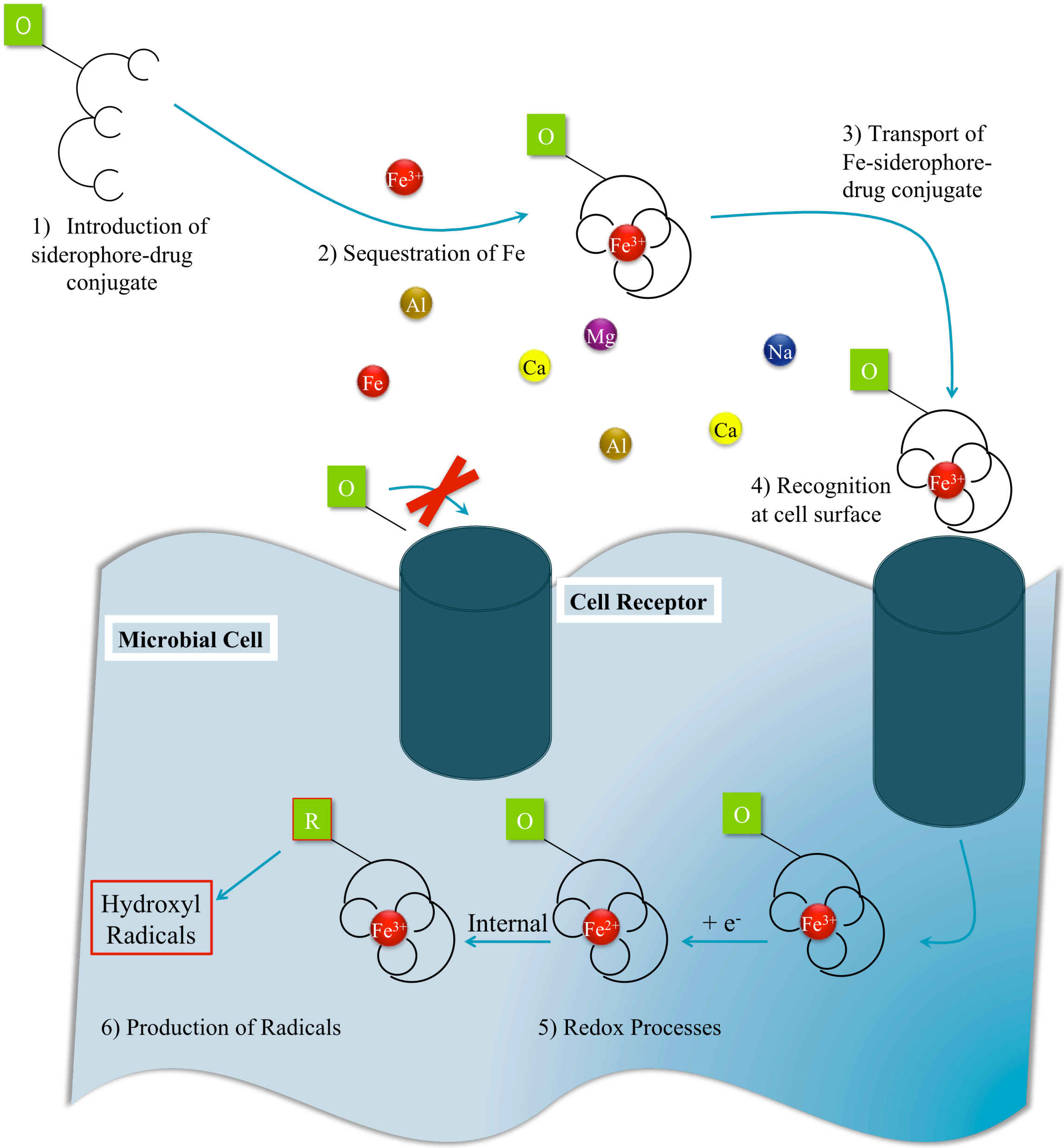

Figure 4.22 Trojan horse approach to artemisinin delivery in the *M. tuberculosis* microbial cell. Taking advantage of the iron-sequestering pathway of a microbial cell, (1) artemisinin in its oxidized state can be coupled to mycobactin, a siderophore produced by *M. tuberculosis*. This siderophore (2) specifically sequesters and binds iron, which it then (3) transports to the cell surface for (4) recognition by a cell receptor. Due to the recognition factor present in mycobactin, the mycobactin•artemisinin complex is taken up into the cell. A series of (5) redox processes result in the reduction of artemisinin. This reduction causes the cleavage of a peroxo bridge in artemisinin, (6) resulting in the generation of hydroxyl radicals.

This application of the "Trojan Horse" approach towards drug delivery demonstrates that new microbe selective antibiotics can be generated by an appropriate combination of antibiotics and microbial iron sequestering agents. It improves on the current approach to antibiotic delivery by utilizing the iron sequestering pathways of the microbial cell and therefore eliminating the concern for the development of drug resistance.

Appendix A: General Chemistry and the NO_2/N_2O_4 System: It's not as Simple as it Appears (and That Can Make It an Enrichment Teaching Tool)[1]

E. M. Tristani, D.B. Chesnut and A. L. Crumbliss

Department of Chemistry, Duke University, Box 90346, Durham, NC 27705-0346

Introduction

The seemingly simple NO_2 / N_2O_4 system is widely used by authors of general chemistry texts to illustrate chemical bonding principles and theories, formal charges, exceptions to the octet rule, chemical equilibria, and chemical kinetics.

$$2\ NO_2\ (g) \leftrightarrows N_2O_4\ (g) \tag{A.1}$$

One of the draws of this reaction is the ease with which students can visibly monitor the progress towards equilibrium by observing color changes that occur in the flask as the reaction proceeds. N_2O_4 is a colorless gas which, when warmed above its boiling point (21.2 °C), dissociates into a dark brown gas (NO_2). As the dissociation of N_2O_4 continues, the color intensifies until equilibrium is reached. Eventually the color change ceases even though some N_2O_4 remains in the reaction flask [119]. Consequently, the amount of NO_2 in the mixture can be determined by measuring the intensity of the color of the gas mixture [119]. Equilibrium may be reached from either direction with pure NO_2 or a mixture of NO_2 and N_2O_4 as starting materials with similar results [120].

The NO_2 / N_2O_4 reaction is also useful for reasons other than the study of opposing processes coming to equilibrium. It allows for the study of factors that determine the concentrations of reactants and products at equilibrium from which the

---

[1] This appendix has been adapted from Tristani, E.M.; Chesnut, D.B.; Crumbliss, A.L. **General chemistry and the NO2/N2O4 system: It's not as simple as it appears, and that can make it an enrichment teaching tool**. Chem. Educ., 2010.

expression of the equilibrium constant as a pressure constant (K_p) or concentration constant (K_c) can be obtained. Furthermore, the reaction offers a simple way of demonstrating the effect of Le Chatelier's principle as changes in volume / pressure are observed along with changes in color. For example, a mixture of the gases held in an air-tight syringe will change color once pressure is applied via the syringe plunger. Reducing the volume of a gaseous mixture at equilibrium causes the system to shift in a direction which reduces the number of moles of gas. Conversely, increasing the volume shifts the system towards a greater number of moles of gas [120]. A shift in equilibrium towards production of NO_2 (greater moles of gas) is achieved by applying pressure which compresses the mixture, thus temporarily increasing the temperature and creating a darker mixture (that of the color of NO_2). Once equilibrium is reached the color returns to a lighter shade as formation of N_2O_4 is favored by the pressure increase [119].

When general topics such as these are considered independently, the NO_2 / N_2O_4 paradigm works well as a means of illustration. However, complications arise when, for example, the simple rules of formal charges and structures associated with the reactants and products of the dimerization reaction are considered in concert. We find these subtleties can be of interest to the motivated / inquisitive student and are an enrichment teaching opportunity.

We contend that the increased complexity beneath the surface of this commonly used "simple" system provides a rich opportunity to introduce students to the fact that chemistry is not as simple as it is sometimes made out to be, and that deviations can occur from the simple rules often presented in most general chemistry texts. Furthermore this system can serve as an effective enrichment teaching tool which can reward rather than confuse the inquisitive student mind with its complexity. In further stating our case we will demonstrate that while the NO_2 / N_2O_4 system can be successfully used to demonstrate certain fundamental principles of general chemistry and its framework of simplified rules, the true picture can also be appreciated by the beginning student as an illustration that simple rules merely guide our entry into the fascinating study of chemistry, and that these rules may not always sufficiently explain what is happening and should be discarded when experimental data dictate that they are not applicable. This can be used in an enrichment discussion with small groups of students truly motivated to understand chemistry and its subtleties.

Exceptions to the Octet Rule, Resonance, Formal Charges and the NO_2 Dimerization Reaction

General chemistry texts commonly discuss exceptions to the octet rule for chemical bonding soon after presenting the Lewis electron dot octet rule paradigm, resonance structures, and the use of formal charges to determine which resonance structures are valid or more important. Nitrogen dioxide (NO_2) is usually used as an example to illustrate such exceptions, when an atom has less than a full octet, or an odd number of electrons. Students are faced with the choice of having a 7-electron N atom or 7-electron O atom. Prior to the text book discussion of the exception to the octet rule involving compounds containing atoms with fewer than eight valence electrons, students are generally taught to choose between major and minor resonance forms by determining the formal charges for each atom in a particular Lewis structure. This principle is illustrated in Scheme 1 where four resonance forms for NO_2 are shown.

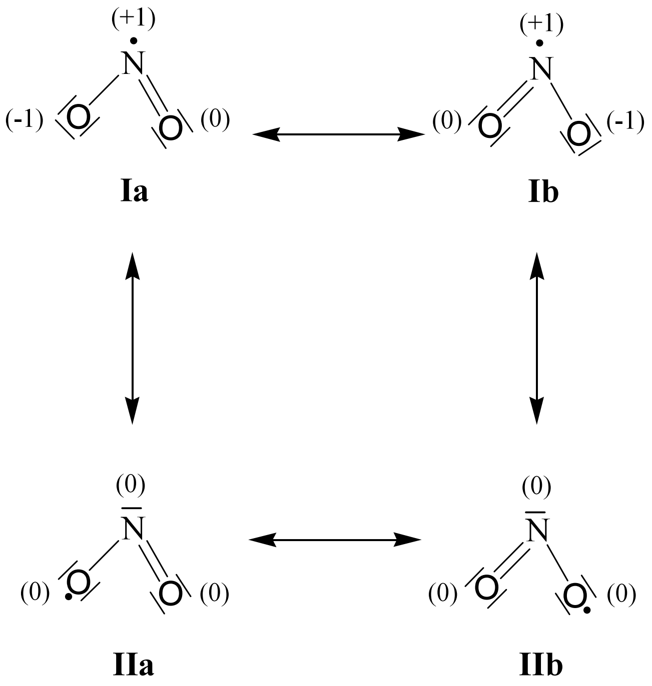

Scheme 1 Resonance forms for NO_2 and their associated formal charges.

Based on guidelines promoted by most general chemistry textbooks, students are told that resonance forms which exhibit the least amount of charge separation are most likely to be the "true" structures [121]. In this case students will logically select structures **IIa** and **IIb** and discard **Ia** and **Ib**. Beyond this charge separation principle, there is nothing in the Lewis structure rules that permits preference to be drawn between structures **I** and **II**. However, some confusion may arise later in that the text subsequently teaches that NO_2 will readily dimerize to form N_2O_4. When students look at the structure shown for N_2O_4, they see that it contains a N—N bond (see **III**), presumably due to coupling the "odd" electron on each N atom of NO_2 in the supposedly unfavored structures **Ia** and **Ib**. This seemingly contradictory structure **III** provides an excellent opportunity to turn students on to what chemistry is really about.

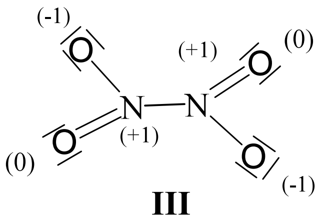

III

We should note that while **III** is the vastly predominant ground state form of the NO_2 dimer, structures **Ia** and **IIa** could in principle be combined to produce dimer structure **IV**. Similarly, structures **IIa** and **IIb** can be theoretically combined to yield structure **V** as shown below.[2]

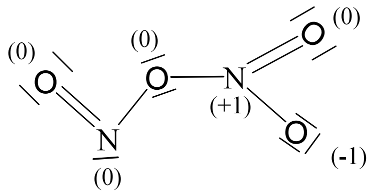

IV

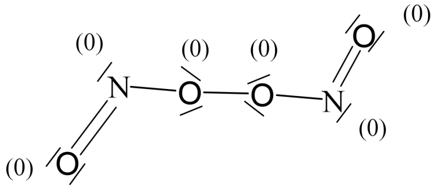

V

But, as has been pointed out in the literature [122], species **IV** is unstable and has been observed only under extreme conditions such as low temperature matrices or at

---

[2] There are three idealized ways in which the reactants can collide, but there are also an infinite number of orientations, representing the rotation of the molecules, which are intermediate between these idealized collisions. In the process of colliding there is a perturbation of the valence electrons that leads to the formation of the product dimer structure. For further theoretical investigations of the transition state and mechanism of the $NO_2 \leftrightarrows N_2O_4$ reaction see: (a) Ornellas, F.R.; Resende, S.M.; Machado, F.B.C.; Roberto-Neto, O. J. Chem Phys. 2003, 118, 4060-4065. (b) Stirling, A.; Papal, I.; Mink, J.; Salahub, D. J. *J. Chem. Phys.* **1994,** 100, 2910-2923.

high pressures and temperatures. Structure **V** has, to our knowledge, not been observed experimentally although it has been treated theoretically. Note that of the three structures **III**, **IV**, and **V**, **V** has no charge separation, **IV** has minimal charge separation, and the structure found experimentally, **III**, has considerable charge separation and exhibits a Lewis structure where two positive nitrogen atoms are adjacent! This illustrates further that, given what is known experimentally, the oversimplified rules for selecting dominant structures simply break down in this instance.

*Question: If **IIa** and **IIb** are the proper resonance forms for NO_2, why isn't the low energy structure of N_2O_4 that shown in **V**?*

There are several reasons for this observation which are chemically and intellectually satisfying, but which do not follow the simple rules. When presented with this paradox, students can be asked to form hypotheses to rationalize the observed structure for N_2O_4. Three examples are as follows:

Hypothesis #1:

Structures **IIa** and **IIb** do not represent the structure of NO_2 because the formal charge rule does not work in this case. Consequently, the dimerization reaction is shown in Scheme 2.

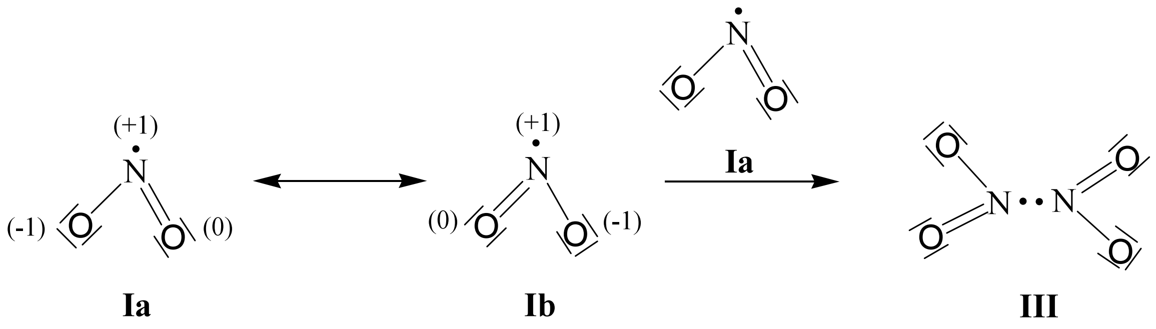

Scheme 2 NO_2 dimerization reaction resulting in a N-N linkage

Hypothesis #2:

All four resonance forms **Ia**, **Ib**, **IIa**, and **IIb** must be considered to represent the structure of NO_2, and while **IIa** and **IIb** are predominant, consistent with the formal charge rules, **Ia** and **Ib** are more "reactive" with respect to dimerization. This hypothesis is illustrated in Scheme 3.

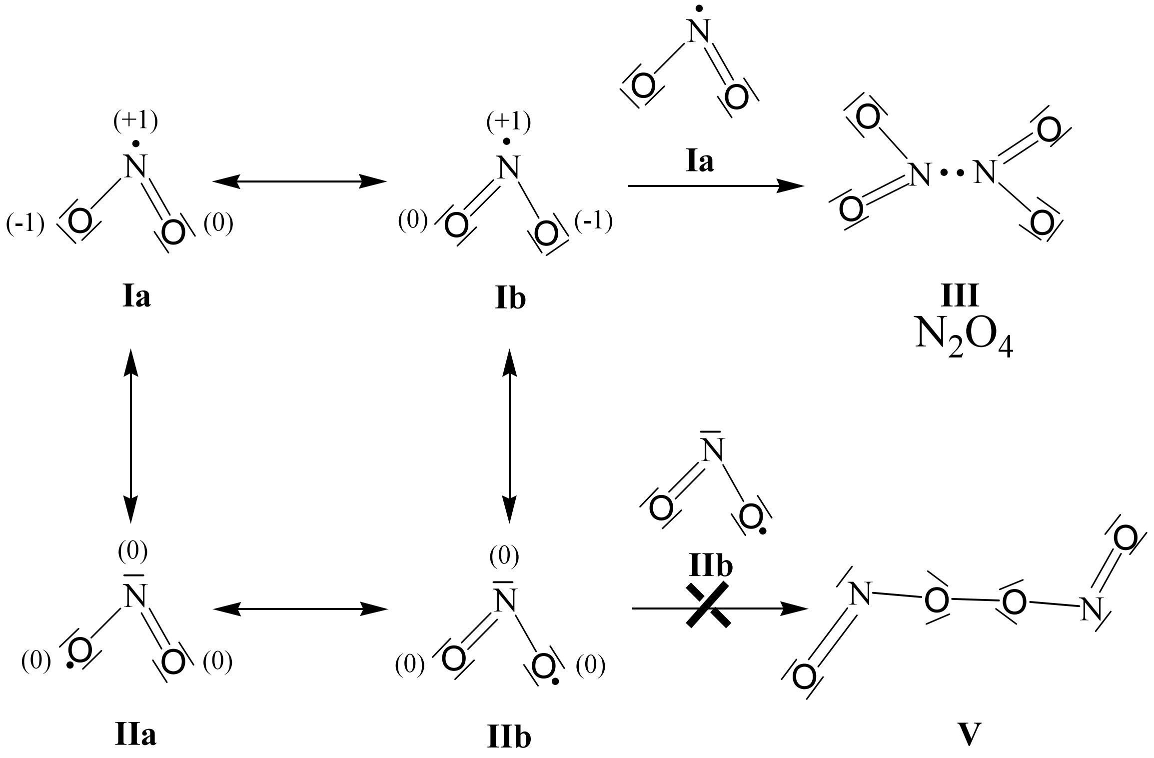

Scheme 3 NO_2 dimerization resulting from N or O-linkage

Hypothesis #3:

Structures **Ia** and **Ib** do not represent the structure of NO_2, consistent with the formal charge rules, but the O—O bonded form of N_2O_4 is unstable and quickly rearranges to the N—N bonded form, as illustrated in Scheme 4.

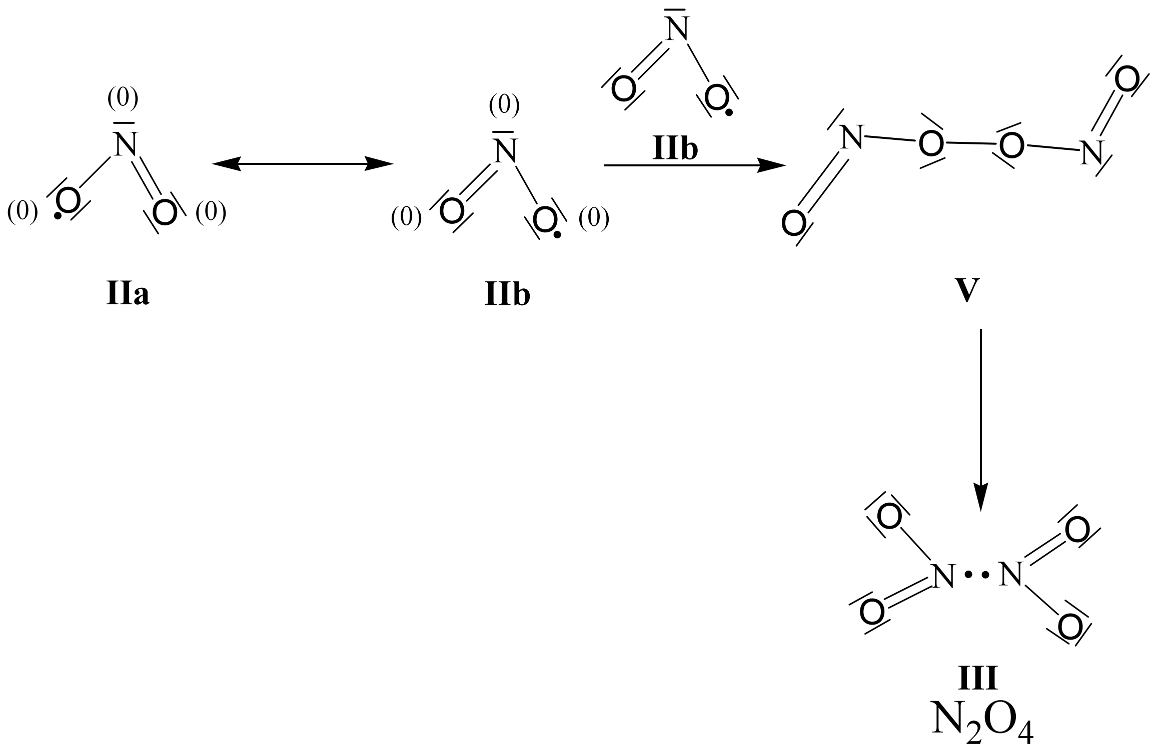

Scheme 4 NO_2 dimerization reaction resulting from O-O linkage followed by rearrangement to a N-N linked species.

Modern experimental and theoretical approaches have been used to study the unusual character of the N—N bond in N_2O_4 and they are useful in discussing which of the competing Lewis structures afford the greatest contribution to the final dimeric structure. These are summarized in a recent publication [123]. Basin populations and their topology obtained from the electron localization function (ELF) [124,125] and atoms-in-molecules (AIM) integrated spin density [126] and delocalization indices [127] were used to study the properties of the NO_2 / N_2O_4 system in hopes of elucidating the electronic structure. ELF describes chemical bonding based on a topological analysis of local quantum mechanical wavefunctions related to the Pauli exclusion principle. AIM provides a method for analyzing the electron density distribution in a manner which yields information on atoms and the bonds between them in a molecule. The technique uses the electron density to partition space into atoms. Density functional Kohn-Sham single determinant wavefunctions were used to determine electronic properties. Chesnut and Crumbliss [123] present data that can be used to directly address contradictions that general chemistry students face in studying this system. This theoretical paper allows us to arrive at conclusions that are not in accordance with the simple rules presented in certain general chemistry texts, illustrating that these rules are not absolute and in this particular case need to be modified. Of the possible hypotheses for N_2O_4 formation presented above, and based on the experimental data provided, we can conclude that the true ground state structure of N_2O_4 is that shown in **III**. An explanation based on the approach in reference [123] is as follows.

As explained previously, introductory chemistry students are taught to choose the NO_2 structure where only the oxygen carries the odd electron (**IIa**, **IIb**), as this provides the least charge separation in the molecule. However, data from theory [123] that well reproduce the hyperfine coupling constants show that there is considerable spin density on the nitrogen atom as depicted by structures **Ia** and **Ib**. Structures **Ia** and **Ib** each represent 21% of the overall structure of the NO_2 molecule for a total of 42%, while structures **IIa** and **IIb** each represent 29%, totaling 58%. This indicates that structures with the odd electron on the nitrogen have a significant presence in the overall structure, a fact that is not made obvious by choosing a structure based on the simple formal charge rules presented in most undergraduate texts.

Students must also rethink the rules if they are to understand how two NO_2 molecules come together to form the dimer, N_2O_4. As discussed earlier, based on formal charge separation students incorrectly select structure **V** over **III** or **IV** as the correct structure for N_2O_4. However, further analysis of the bonding interactions between the two NO_2 molecules as they come together provides an accurate representation of the

N_2O_4 structure. If structures **IIa** and **IIb** are considered, as the NO_2 molecules come together to form N_2O_4 the net effect would be a weakly antibonding or even nonexistent N—N bond. On the other hand, if structures **Ia** and **Ib** are considered as the two NO_2 molecules approach each other to form N_2O_4, a strong N—N bond would be expected due to the location of the unpaired electron on each nitrogen on the NO_2 fragment and its contribution to the new bond. If structures **Ia** and **IIa** (or **Ib** and **IIb** alternately) are considered as two NO_2 molecules come together at the N atoms, a two-center three electron bond would form resulting in a "half bond" at best. Thus, as illustrated by the structures, when the two NO_2 moieties corresponding to structures **IIa** and **IIb** or a mixture of **Ia** or **Ib** with **IIa** or **IIb** come together to form N_2O_4 the net result is a very weak sigma bond. While not at all obvious from our arguments, theory has shown that there is essentially no contribution from the pπ parts of the molecules. At this point in their training students are not likely to worry about π-system interactions, but the instructor can state this as a "fact" that results from the above simplified analysis.

The NO_2 / N_2O_4 paradigm is an ideal system to illustrate that chemistry is not always as simple as it might seem, and that general rules are often not absolute and must be massaged in the presence of contradictory data. In addition, this system presents an opportunity to demonstrate the relevance of the general subject of chemistry, in that concepts that have been taught for years still pose valid scientific questions of interest to modern day researchers. Through exposure to inconsistencies when simple rules are rigidly applied, coupled with some discussion of current research results aimed at understanding the underlying chemistry, students may learn to appreciate the complexity and beauty of chemistry while also developing better critical thinking skills which will benefit them in their future studies.

Acknowledgement

ALC thanks his Chem 21 and Chem 23 students for their enthusiasm and their feedback.

References

[1] Steed, J. W.; Atwood, J. L. *Supramolecular Chemistry*; John Wiley & Sons, Ltd: Chichester, 2000.

[2] Werner, A. *Zeitschr. Anorg. Chem.* **1893**, *3*, 267.

[3] Fischer, E. *Ber. Deutsch. Chem. Ges.* **1894**, *27*, 2985.

[4] Behr, J.-P. *The Lock and Key Principle. The State of the Art - 100 Years On*; Wiley: Chichester, 1994.

[5] A. Villiers, C. R. H. *Seances Acad. Sci.* **1891**, *112*, 435.

[6] A. Villiers, C. R. H. *Seances Acad. Sci.* **1891**, *112*, 536.

[7] Schalley, C. A. *Analytical Methods in Supramolecular Chemistry*; Wiley: Weinheim, 2007.

[8] Buckingham, A. D.; Legon, A. C.; Roberts, S. M. *Principles of Molecular Recognition*; Blackie Academic & Professional: London, 1993.

[9] Miller, M. J.; Darwish, I.; Ghosh, A.; Ghosh, M.; Hansel, J.; Hu, J.; Niu, C.; Ritter, A.; Scheidt, K.; Suling, C.; Sun, S.; Zhang, D.; Budde, A.; De Clercq, E.; Leong, S.; Malouin, F.; Moellmann, U. In *Anti-Infectives: Recent advances in chemistry and structure-activity relationships*; Bentley, P. H., O'Hanlon, P. J., Eds.; The Royal Society of Chemistry: Cambridge, 1997, p 116.

[10] Crichton, R. *Inorganic Biochemistry of Iron Metabolism: From Molecular Mechanisms to Clinical Consequences*; Second ed ed.; John Wiley & Sons, LTD: Chichester, 2001.

[11] Fenton, H. J. H. *J. Chem. Soc.* **1894**, *65*, 899.

[12] J. Pierre; Fontecave, M. *BioMetals* **1999**, *12*, 195.

[13] K. N. Raymond; Dertz, E. A. In *Iron Transport in Bacteria*; J. H. Crosa, A. R. Mey, Payne, S. M., Eds.; ASM Press: Washington, D.C., 2004, p 3.

[14] Winkelmann, G. *CRC Handbook of Microbial Chelates*; CRC Press: New York, 1991.

[15] Albrecht-Gary, A.-M.; Crumbliss, A. L. In *Iron Transport and Storage in Microorganisms, Plants, and Animals*; Sigel, A., Sigel, H., Eds.; M. Dekker, Inc: New York, 1998; Vol. 35, p 239.

[16] Telford, J. R.; Raymond, K. N. In *Comprehensive Supramolecular Chemistry*; Lehn, J.-M., Ed.; Pergammon Press: London, 1996; Vol. 1, p 245.

[17] Drechsel, H.; Winkelmann, G. In *Transition Metals in Microbial Metabolism*; Winkelmann, G., Carrano, C. J., Eds.; Harwood: Amsterdam, 1997.

[18] Ratledge, C. *Tuberculosis* **2004**, *84*, 110.

[19] B. F. Matzanke; S. Anemuller; V. Schunemann; A. X. Trautwein; Hantke, K. *Biochem.* **2004**, *43*, 1386.

[20] Ettlinger, L.; Corbaz, R.; Hutter, R. *Arch. Microbiol.* **1958**, *31*, 326.

[21] Schwarzenbach, G.; Schwarzenbach, K. *Helv. Chim. Acta* **1963**, *46*, 1390.

[22] Gabutti, V.; Piga, A. *Acta Haematol.* **1996**, *95*, 26.

[23] Batinic-Haberle, I.; Spasojevic, I.; Crumbliss, A. L. *Inorg. Chem.* **1996**, *1996*, 2352.

[24] Batinic-Haberle, I.; Spasojevic, I.; Crumbliss, A. L. *Inorg. Chim. Acta* **1997**, *260*, 35.

[25] Batinic-Haberle, I.; Spasojevic, I.; Jang, Y.; Bartsch, R. A.; Crumbliss, A. L. *Inorg. Chem.* **1998**, *37*, 1438.

[26] Batinic-Haberle, l.; SpasojeviC, I.; Bartsch, R. A.; Crumbliss, A. L. *J. Chem. Soc. Dalton Trans* **1995**, *15*, 2503.

[27] Crumbliss, A. L.; Batinic Haberle, I.; Spasojevic, I. *Pure Appl. Chem.* **1996**, *68*, 1225.

[28] Dhungana, S.; White, P.; Crumbliss, A. *J Am Chem Soc* **2003**, *125*, 14760.

[29] Dhungana, S.; White, P. S.; Crumbliss, A. L. *J. Biol. Inorg. Chem.* **2001**, *6*, 810.

[30] Spasojevic, I.; Armstrong, S. K.; Brickman, T. J.; Crumbliss, A. L. *Inorg. Chem.* **1999**, *38*, 449-454.

[31] Spasojevic, I.; Batinic-Haberle, I.; Choo, P. L.; Crumbliss, A. L. *J. Am. Chem. Soc.* **1994**, *116*.

[32] Spasojevic, I.; Batinic-Haberle, I.; Choo, P. L.; Crumbliss, A. L. *J. Am. Chem. Soc.* **1994**, *116*.

[33] Spasojevic, I.; Boukhalfa, H.; Stevens, R. D.; Crumbliss, A. L. *Inorg. Chem.* **2001**, *40*, 49-58.

[34] Spasojevic, I.; Crumbliss, A. L. *J. Chem. Soc. Dalton Trans.* **1998**, 4021.

[35] Spasojevic, I.; Crumbliss, A. L. *Inorg. Chem.* **1999**, *38*, 3248-3250.

[36] Trzaska, S. M.; Toone, E. J.; Crumbliss, A. L. *Inorg. Chem.* **2000**, *39*, 1071.

[37] Tristani, E. M.; Dubay, G. R.; Crumbliss, A. L. *J Incl Phenom Macro* **2009**, *64*, 57-65.

[38] Tristani, E. M.; Wirgau, J. I.; Dubay, G. R.; Sibert, J. W.; Crumbliss, A. L. *Inog. Chim. Acta* **2010**, (submitted).

[39] Evers, A.; Hancock, R. D.; Martell, A. E.; Montekaitis, R. J. *Inorg. Chem.* **1989**, *28*, 2189.

[40] Hiraoka, M. *Crown Ethers and Analogous Compounds*; Elsevier: Amsterdam, 1992; Vol. 45.

[41] Cox, B.; Schneider, H. *Coordination and Transport Properties of Macrocyclic Compounds in Solution*; Elsevier: Amsterdam, 1992.

[42] Inoue, Y.; Gokel, G. W. *Cation Binding by Macromolecules*; Marcel Dekker, Inc.: New York, 1990.

[43] Gokel, G. *Crown Ethers and Cryptands*; The Royal Society of Chemistry: Cambridge, 1991.

[44] Chang, R. *Chemistry*; 9 ed.; McGraw Hill: New York, 2007.

[45] Charewicz, W.; Heo, G.; Bartsch, R. *Anal. Chem.* **1982**, *54*, 2094.

[46] Connors, A. K. *Binding Constants: The Measurement of Molecular Complex Stability*; Wiley: New York, 1997.

[47] Foster, R.; Fyfe, C. *Prog. Nucl. Magn. Reson. Spectrosc.* **1969**, *4*, 1.

[48] Frensdorff, H. *J. Am. Chem. Soc.* **1971**, *93*, 600.

[49] Izatt, R.; Bradshaw, J.; Nielsen, S.; Lamb, J.; Christensen, J.; Sen, D. *Chem. Rev.* **1985**, *85*, 271.

[50] Izatt, R.; Bradshaw, J.; Pawlak, K.; Bruening, R.; Tarbet, B. *Chem. Rev.* **1992**, *92*, 1261.

[51] Izatt, R.; Pawlak, K.; Bradshaw, J.; Bruening, R. *Chem. Rev.* **1991**, *91*, 1721.

[52] Michaux, G.; Reisse, J. *J. Am. Chem. Soc.* **1982**, *104*, 6895.

[53] Schmidt, E.; Popov, A. *J. Am. Chem. Soc.* **1983**, *105*, 1873.

[54] Walkowiak, W.; Charewicz, W.; Kang, S.; Yang, I.; Pugia, M.; Bartsch, R. *Anal. Chem.* **1990**, *62*, 2018.

[55] Wu, G.; Jiang, W.; Lamb, J.; Bradshaw, J.; Izatt, R. *J. Am. Chem. Soc.* **1991**, *113*, 6538.

[56] Greig, M.; Gaus, H.; Cummins, L.; Sasmor, H.; Griffey, R. *J. Am. Chem. Soc.* **1995**, *117*, 10765.

[57] Griffer, R. H.; Hofstadler, S. A.; Sannes-Lowery, K. A.; Ecker, D. J.; Crooke, S. T. *Proc. Natl. Acad. Sci.* **1999**, *96*, 10129.

[58] Jorgensen, T.; Roepstorff, P.; Heck, A. *Anal. Chem.* **1998**, *70*, 4427.

[59] Lim, H.-K.; Hsieh, Y. L.; Ganem, B.; Henion, J. *J. Mass Spectrom.* **1995**, *30*, 708.

[60] Loo, J. A.; Hu, P.; McConnell, P.; Mueller, W. T.; Sawyer, T. K.; Thanabal, V. *J. Am. Soc. Mass. Spectrom.* **1997**, *8*, 234.

[61] Prieto, M.; Whittal, R.; Balwin, M.; Burlingame, A.; Balhorn, R. *Proceed. 47th ASMS Conf. Mass Spectrom. All. Top.* **1999**, 614.

[62] Young, D.-S.; Hung, H.-Y.; Liu, L. K. *Rapid Commun. Mass Spectrom.* **1997**, *11*, 769.

[63] Przybylski, M.; Glocker, M. O. *Angew. Chem. Int. Edit.* **1996**, *35*, 806.

[64] Smith; Bruce, R. D.; Wu, J. E.; Lei, Q.; Paula, Q. *Chem. Soc. Rev.* **1997**, *26*, 191.

[65] Smith, D. L.; Zhang, Z. *Mass Spectrom. Rev.* **1994**, *13*, 411.

[66] Blair, S. M.; Kempen, E. C.; Brodbelt, J. S. *J. Am. Soc. Mass. Spectrom.* **1998**, *9*, 1049.

[67] Brodbelt, J. S.; Kempen, E. C.; Reyzer, M. *Struct. Chem.* **1999**, *10*, 213.

[68] Kempen, E. C.; Brodbelt, J. S. *Anal. Chem.* **2000**, *72*, 5411.

[69] Kempen, E. C.; Brodbelt, J. S.; Bartsch, R. A.; Blanda, M. T.; Farmer, D. B. *Anal. Chem.* **2001**, *73*, 384.

[70] Caudle, M. T.; Stevens, R. D.; Crumbliss, A. L. *Inorg. Chem.* **1994**, *33*, 843.

[71] Caldwell, C.; Crumbliss, A. *Inorg. Chem.* **1998**, *37*, 1906.

[72] Backer, M. D.; Hureau, M.; Depriester, M.; Deletoille, A.; Sargent, A. L.; Forshee, P. B.; Sibert, J. W. *J. Electroanal. Chem.* **2008**, *612*, 97.

[73] Sibert, J.; Seyer, D.; Hundt, G. *Journal of Supramolecular Chemistry* **2002**.

[74] Kaifer, A. E.; Mendoza, S. In *Comprehensive Supramolecular Chemistry*; Gokel, G., Atwood, J., Davies, J., MacNicol, D., Vogtle, F., Eds.; Pergammon: Oxford, 1996; Vol. 1, p 701.

[75] Boulas, P.; Gomez-Kaifer, M.; Echegoyen, L. *Angew. Chem. Int. Ed. Engl.* **1998**, *37*, 216.

[76] Wurster, C. *Ber. Dtsch. Chem. Ges.* **1879**, *12*, 522.

[77] Pearson, A.; Hwang, J. *Tetrahedron Letters* **2001**.

[78] Zhang, X.; Buchwald, S. *J. Org. Chem* **2000**.

[79] Sibert, J. W.; Pierce, B. M. In *Book of Abstracts 214th ACS National Meeting* Las Vegas, NV, 1997, p INOR-364.

[80] Sibert, J. W. U.S., 2001; Vol. Patent 6,262,258.

[81] Sibert, J. W. U.S., 2002; Vol. Patent 6,441,164.

[82] Sibert, J.; Forshee, P. *Inorg. Chem* **2002**, *41*, 5928.

[83] Sibert, J.; Forshee, P.; Hundt, G.; Sargent, A.; Bott, S. *Inorg. Chem* **2007**.

[84] Sibert, J.; Forshee, P.; Lynch, V. *Inorg Chem* **2005**, *44*, 8602.

[85] Sibert, J.; Hundt, G.; Sargent, A.; Lynch, V. *Tetrahedron* **2005**, *61*, 12350.

[86] Sargent, A.; Mosley, B.; Sibert, J. *J. Phys. Chem. A* **2006**.

[87] Wirgau, J. I. *Ph.D. Dissertation*; Duke University: Durham, NC, 2003.

[88] Spasojević, I.; Crumbliss, A. *J. Chem. Soc. Dalton Trans,* **1998**.

[89] Daas, C. *Principles and Practice of Biological Mass Spectrometry*; Wiley: New York, 2001.

[90] Thomson, J. A.; Ladbury, J. E. In *Biocalorimetry 2: Applications of Calorimetry in the Biological Sciences*; Ladbury, J. E., Doyle, M. L., Eds.; Wiley: New Jersey, 2004.

[91] Tellinghuisen, J. *Analytical Biochemistry* **2008**, *373*, 395.

[92] Turnbull, W. B.; Daranas, A. H. *J. Am. Chem. Soc.* **2003**, *125*, 14859-14866.

[93] Christensen, T.; Gooden, D. M.; Kung, J. E.; Toone, E. J. *J. Am. Chem. Soc.* **2003**, *125*, 7357-7366.

[94] Dhungana, S.; White, P.; Crumbliss, A. *J Am Chem Soc* **2003**, *125*, 14760-14767.

[95] Miller, S. R.; Gustowski, D. A.; Chen, Z.; Gokel, G. W.; Echegoyen, L.; Kaifer, A. E. *Anal. Chem.* **1988**, *60*, 2021.

[96] Jong, F. D.; Reinhoudt, D. N.; Huid, R. *Tetrahedron Letters* **1977**, 3985.

[97] Boer, J. A. A. D.; Reinhoudt, D. N. *J. Am. Chem. Soc.* **1985**, *107*, 5347.

[98] Snider, D. E. J.; Raviglione, M.; Kochi, A. In *Tuberculosis: Pathogenesis, Protection, and Control*; ASM Press: Washington, D.C., 1994, p 3.

[99] Dorman, S.; Chaisson, R. *Nat. Med.* **2007**, *13*, 295.

[100] Stover, C.; Warrener, P.; VanDevanter, D.; Sherman, D.; Arain, T. M.; Langhorne, M. H.; Anderson, S. W.; Towell, J. A.; Yuan, Y.; McMurray, D. N.; Kreiswirth, B. N.; Barryk, C. E.; Baker, W. R. *Nature* **2000**, *405*, 962.

[101] Möllmann, U.; Heinisch, L.; Bauernfeind, A.; Köhler, T.; Ankel-Fuchs, D. *Biometals* **2009**, *22*, 615.

[102] Talbot, G. *Expert Rev. Anti. Infe.* **2008**, *6*, 39.

[103] Talbot, G. H.; Bradley, J.; Edwards, J. E.; Gilbert, D.; Scheld, M. E.; Bartlett, J. G. *Clin. Infect. Dis.* **2006**, *42*, 657.

[104] Zahner, H.; Diddens, H.; Keller-Schierlein, W.; Nageli, H.-U. *Jpn. J. Antibiot.* **1977**, *30*, S201.

[105] Braun, V. *Drug Resist. Updat.* **1999**, *2*, 363.

[106] Wencewicz, T. A.; Möllmann, U.; Long, T. E.; Miller, M. J. *Biometals* **2009**, *22*, 633.

[107] Miller, M. J. D., I.; Ghosh, A.; Ghosh, M.; Hansel, J.; Hu, J.; Niu, C.; Ritter, A.; Scheidt, K.; Suling, C.; Sun, S.; Zhang, D.; Budde, A.; De Clercq, E.; Leong, S.; Malouin, F.; Moellmann, U., In *Anti-Infectives: Recent advances in chemistry and structure-activity relationships*; Bentley, P., O'Hanlon, P., Eds.; The Royal Society of Chemistry: Cambridge, 1997, p 116.

[108] Miller, M. J. *unpublished*.

[109] Feng Zhang, D. K. G., Jr. and Steven R. Meshnick *Biochem. Pharmacol.* **1992**, *43*, 1805-1809.

[110] Meshnick, S. R. *Int. J. Parasitol.* **2002**, *32*, 1655.

[111] Fuochi, P. G.; Marconi, G.; Mulazzani, Q. G. *Int. J. Radiat. Biol.* **2005**, *81*, 319.

[112] Posner, G.; Oh, C. H. *J. Am. Chem. Soc.* **1992**, *114*, 8328.

[113] Lai, H.; Sasaki, T.; Singh, N. *Expert Opin. Ther. Targets* **2005**, *9*, 995.

[114] Crumbliss, I. S. a. A. L. *J. Chem. Soc., Dalton Trans.* **1998**, 4021-4027.

[115] Spasojevic, I.; Crumbliss, A. *Inorg Chem* **1999**, *38*, 3248-+.

[116] Jiang, H. L.; Chen, K. X.; Tang, Y.; Chen, J. Z.; Li, Y.; Wang, Q. M.; Ji, R. Y. *Indian J. Chem.* **1997**, *36B*, 154.

[117] Kissinger, P. T.; Heineman, W. R. *Laboratory Techniques in Electroanalytical Chemistry*; Marcel Dekker: New York, 1984.

[118] Ratledge, C. *Biochem. Bioph. Res. Co.* **1971**, *45*, 856.

[119] Brown, T. L.; LeMay, E. H.; Bursten, B. E.; Murphy, C. J. *Chemistry: The Central Science*; Tenth ed.; Prentice Hall: New Jersey, 2006.

[120] Chang, R. *Chemistry*; Ninth ed.; McGraw-Hill: New York, 2007.

[121] Chang, R. *Chemistry*; Ninth ed.; McGraw-Hill: New York, 2007.

[122] Stirling, A.; Papal, I.; Mink, J. *J. Chem. Phys.* **1994**, *100*, 2910.

[123] Chesnut, D. B.; Crumbliss, A. L. *Chemical Physics* **2005**, *315*.

[124] Becke, A. D.; Edgecomb, K. E. *J. Chem. Phys.* **1990**, *92*, 5397.

[125] Silvi, B.; Savin, A. *Nature* **1994**, *371*, 683.

[126] Bader, R. F. *Atoms in Molecules: a Quantum Theory*; Oxford University Press: Oxford, 1994.

[127] Fradera, X.; Austen, M. A.; Bader, R. F. *J. Phys. Chem. A* **1999**, *103*, 304.

Biography

Esther Marie Tristani was born August 28, 1984 to Ramon and Carmen Tristani in San Juan, Puerto Rico. She lived and studied in Puerto Rico until a move to Bloomington, IN in 1999. There she attended Bloomington High School South, where she graduated Valedictorian in 2001. After graduation, she enrolled in Indiana University Bloomington, where she received a *Bachelors of Science* in Chemistry with Mathematics and Spanish minors in 2005. From here she moved to North Carolina to obtain her *Doctorate of Philosophy* in Chemistry at Duke University.

Upon graduating, Esther will move to Pleasanton, CA to begin her career in industry at The Clorox Company.

Awards:

Duke Endowment Fellowship, 2005-2010

Duke University Graduate School Conference Travel Fellowship, April 2008-2010

John Herbert Pearson Teaching Award, Spring 2008

Affiliations:

American Chemical Society

Phi Lambda Upsilon

Publications:

Walz, A.J.; Zhu, H.; Wu, C.; Moraski, G.; Miller, M.J.; Möllmann, U.; **Tristani, E.M.**; Crumbliss, A.L.; Ferdig, M.; Boshoff, H. *Delivery is special: The Antimalarial Agent Artemisinin also becomes a Potent Anti-TB Agent when Conjugated to a Mycobacterial Siderophore Analog*. Manuscript in preparation, 2010.

Tristani, E.M.; Wirgau, J.I.; Dubay, G.R.; Sibert, J.W.; Crumbliss, A.L. *Siderophore-Redox Active Ionophore Host-Guest Assemblies: A Prototype for Selective Metal Ion Compartmentalization*. Submitted for publication in Inorg. Chim. Acta, 2010.

Tristani, E.M.; Dubay, G.R.; Crumbliss, A.L. *Characterization of second coordination shell host-guest assemblies and binding selectivities in binary and complex mixtures by Electrospray Ionization Mass Spectrometry*. J. Incl. Phenom. Macro., 64, 57-65, **2009**.

Tristani, E.M.; Chesnut, D.B.; Crumbliss, A.L. *General Chemistry and the* NO_2 / N_2O_4 *System: It's not as simple as it appears, and that can make it an enrichment teaching tool*, Chem. Educ., 2010.

Presentations:

Tristani, E.M.; Chesnut, D.B.; Crumbliss, A.L. *General Chemistry and the* NO_2 / N_2O_4 *System: It's not as simple as it appears when the rules don't work*, 61st Southeast Regional Meeting of the American Chemical Society (SERMACS), San Juan, PR, October, 2010.

Tristani, E.M.; Dubay, G.R.; Crumbliss, A.L. *Mass spectral method for the quantification of host-guest interactions including ionophore-siderophore assemblies,* 123rd North Carolina American Chemical Society Local Section Meeting, Research Triangle Park, NC, September, 2007.

Tristani, E.M.; Wirgau, J.I.; Sibert, J.W.; Crumbliss, A.L. *Microcalorimetric determination of the thermodynamic parameters for redox active ionophore-siderophore host-guest complex formation,* 238th National Meeting of the American Chemical Society, Washington, D.C., August, 2009.

Tristani, E.M.; Dubay, G.R.; Crumbliss, A.L. *Mass spectral method for the quantification of host-guest interactions including ionophore-siderophore assemblies,* 57th Conference of the American Society for Mass Spectometry, Philadelphia, PA, June, 2009.

Tristani, E.M.; Dubay, G.R.; Crumbliss, A.L. *Characterization of second coordination shell host-guest assemblies and binding selectivities by Electrospray Ionization Mass Spectrometry,* 235th ACS National Meeting, New Orleans, LA, April, 2008.

Tristani, E.M.; Crumbliss, A.L. *Utilizing ESI-MS to probe ionophore-siderophore host-guest interactions,* 121st North Carolina American Chemical Society Local Section Meeting, Durham, NC, April, 2007.